THE HONG KONG
POLYTECHNIC UNIVERSITY
香港理工大學
Pao Yue-kong Library
包玉剛圖書館

Copyright Undertaking

Pao Yue-kong Library, The Hong Kong Polytechnic University, Hung Hom, Kowloon, Hong Kong

http://www.lib.polyu.edu.hk

MAGNETIC COUPLER DESIGN IN WIRELESS POWER TRANSFER FOR VEHICULAR APPLICATIONS

HESHOU   WANG

PhD

The Hong Kong Polytechnic University

2022

The Hong Kong Polytechnic University

Department of Electrical Engineering

Magnetic Coupler Design in Wireless Power Transfer

for Vehicular Applications

Heshou   Wang

A thesis submitted in partial fulfillment of the requirements for

the degree of Doctor of Philosophy

July 2022

CERTIFICATE OF ORIGINALITY

I hereby declare that this thesis is my own work and that, to the best of my knowledge and belief, it reproduces no materials previously published or written, nor material that has been accepted for the award of any other degree or diploma, except where due acknowledgement has been made in the text.

_____(Signed)

HESHOU   WANG   (Name of student)

To my grandmother

Abstract

Wireless power transfer (WPT) is increasingly attractive because of its simplicity and user-friendliness. As a soul part, magnetic coupler design is of great importance in WPT systems with beauty to improve the wanted couplings for energy transfer and to reduce or even eliminate unwanted couplings for stable operation. Furthermore, impressive characteristics, e.g., load-independent outputs, high efficiency, and high misalignment tolerance, are all highly related to magnetic coupler design. Hence, this thesis investigates several special magnetic couplers for wirelessly charging vehicular applications.

Firstly, a special magnetic coupler based on three-coil WPT is proposed to charge electric scooters (ESs). Unipolar Q coil, mixed QDD coil, and bipolar DD coil are designed for the source coil, the transmitter coil (T_X), and the receiver coil (R_X), respectively. This coupler utilizes unipolar coils and bipolar coils, thereby magnetically decoupling the receiver coil from the source coil to realize load-independent output characteristics.

Similarly, Q coils, DD coils and DDQ coils can also be utilized in double-receiver WPT systems for automatic guided vehicles (AGVs) to eliminate the unwanted cross-couplings. Unwanted cross-couplings are the bottleneck to hinder the development of double-receiver WPT systems, which dramatically disturb the system stability because receivers affect each other when the air gap changes, or misalignment happens. Two types of unwanted couplings can be reduced by presented structure. The first-type unwanted couplings between receivers can be eliminated, contributing to independent-work receivers. The second-type unwanted couplings among the source coil and receivers can be eliminated. Thus, load-independent constant voltage (CV) output can be realized. The inverter achieves zero phase angle (ZPA), degrading the volt-ampere rating and increasing efficiency. Most importantly, the coupler design process can become efficient since the proposed structure ensures an easy way to reduce the cross-couplings because the decoupling is from the shape rather than turn numbers.

Then, a novel resonator scheme has been studied for wireless battery charging systems of Electric Bicycles (EBs). The Helmholtz coils are adopted to ensure a stable mutual inductance between the transmitting and receiving coils. The switched S-SP/S compensation scheme can be used to implement load-independent constant current (CC) and constant voltage (CV) charging for the battery loads instead of using bulky LCL or LCC compensation schemes. The advancements of the proposed design, as compared to the conventional methods, are more than constant mutual coupling and elimination of compensated inductors. The communication channel, additional user-end converter, and complicated control algorithms can also be annihilated.

After investigating stational wireless chargers, dynamic wireless power transfer (DWPT) is also presented for wireless charging electric trains (ETs). An innovative topology using parallel multi-inverters, together with an improved magnetic coupler design, is introduced to increase the power capacity. A segmented transmitter technology, in which several transmitters mounted on the rail track are energized according to the position of the onboard pickups, is investigated to realize continuously stable power supply.

Overall, several vehicular-application-oriented WPT systems, including the special magnetic coupler designs, associated power electronics and compensation topologies, are all analyzed in detail, developed, and validated by simulation and experimental tests.

Publications

Main journal papers

1. **H. Wang**, K. W. E. Cheng, X. Li and J. Hu, "A Special Magnetic Coupler Structure for Three-Coil Wireless Power Transfer: Analysis, Design, and Experimental Verification," in *IEEE Transactions on Magnetics*, vol. 57, no. 11, pp. 1-8, Nov. 2021, Art no. 8002108, doi: 10.1109/TMAG.2021.3111738. **[for Chapter 2]**

2. **H. Wang** and K. W. E. Cheng, "Analysis, Design, and Validation of a decoupled Double-receiver Wireless Power Transfer System with Constant Voltage Outputs for Industrial Power Supplies," in *IEEE Transactions on Industrial Informatics*, doi: 10.1109/TII.2022.3165248. **[for Chapter 3]**

3. **H. Wang** and K. W. E. Cheng, "A Dual-Receiver Inductive Charging System for Automated Guided Vehicles," in *IEEE Transactions on Magnetics*, 2022, doi: 10.1109/TMAG.2022.3181576. **[for Chapter 3]**

4. **H. Wang**, K. W. E. Cheng and Y. Yang, "A New Resonator Design for Wireless Battery Charging Systems of Electric Bicycles," *in IEEE Journal of Emerging and Selected Topics in Power Electronics*, doi: 10.1109/JESTPE.2022.3157729. **[for Chapter 4]**

5. **Heshou Wang**, Ka Wai Eric Cheng "An Improved and Integrated Design of Segmented Dynamic Wireless Power Transfer for Electric Vehicles," *Energies*, vol. 14, no. 7, p. 1975, 2021. **[for Chapter 5]**

Other selected journal papers

1. X. Li, J. Hu, Y. Li, **H. Wang**, M. Liu, and P. Deng, "A Decoupled Power and Data-Parallel Transmission Method With Four-Quadrant Misalignment Tolerance for Wireless Power Transfer Systems," *IEEE Transactions on Power Electronics*, vol. 34, no. 12, pp. 11531-11535, 2019. **[for Chapter 3]**

2. X. Li, X. Li, J. Hu, **H. Wang**, X. Dai, and Y. Sun, "A New Coupling Structure and Position Detection Method for Segmented Control Dynamic Wireless Power Transfer Systems," *IEEE Transactions on Power Electronics*, vol. 35, no. 7, pp. 6741-6745, 2020. **[for Chapter 5]**

3. Y. Li, J. Hu, X. Li, **H. Wang**, and K. W. E. Cheng, "Cost-Effective and Compact Multistring LED Driver Based on a Three-Coil Wireless Power Transfer System," *IEEE Transactions on Power Electronics*, vol. 34, no. 8, pp. 7156-7160, 2019. **[for Chapter 2]**

Selected conference papers

1. **H. S. Wang**, K. W. E. Cheng and J. F. Hu, "A Compact Design for a Switchable Wireless Charger," *2020 8th International Conference on Power Electronics Systems and Applications (PESA)*, 2020, pp. 1-7, doi: 10.1109/PESA50370.2020.9343996. (Merit with Mention Award at 8th International Conference on Power Electronics Systems and Applications). **[for Chapter 1]**

2. **H. S. Wang**, K. W. E. Cheng and J. F. Hu, "An Investigation of Compensation Networks for Three-coil Wireless Power Transfer," *2020 8th International Conference on Power Electronics Systems and Applications (PESA)*, 2020, pp. 1-6, doi: 10.1109/PESA50370.2020.9343961. **[for Chapter 1]**

3. **H. Wang** and K. W. Eric Cheng, "An Intermediate-Coil and Ferrite-Based Coupling

Structure With Load-Independent Constant Outputs for Inductive Power Transfer," *2021 IEEE 1st International Power Electronics and Application Symposium (PEAS)*, 2021, pp. 1-4, doi: 10.1109/PEAS53589.2021.9628622. **[for Chapter 2]**

4. **H.S. Wang**, S.R. Zhuo, F. Gao, B. Elena, G. Arnaud, K.W.E. Cheng "An Integrated Design of Cost-Effective Bipolar Hexagonal Coil and Active Disturbance Rejection Control for Inductive Power Transfer," in *the 2022 IEEE/AIAA Transportation Electrification Conference and Electric Aircraft Technologies Symposium*, 15-17 June 2022, accepted. **[for Chapter 3]**

5. **Heshou Wang**, Ka Wai Eric Cheng "Conical Coil Design for Domino Wireless Power Transfer," *The 20th Biennial IEEE Conference on Electromagnetic Field Computation (CEFC)*, 2022, Accepted.

6. **Heshou Wang**, Ka Wai Eric Cheng " An Inductive Power Transfer System with a Special Magnetic Coupler," *The 20th Biennial IEEE Conference on Electromagnetic Field Computation (CEFC)*, 2022, Accepted.

Acknowledgements

Life is a journey; I really enjoy the engineering study in, my Alma Mater, the Hong Kong Polytechnic University. Impressive professors, comfortable environment, and friendly colleagues all leave a wonderful memory for me.

Most importantly, I would like to express my sincere appreciation to my chief supervisor, Prof. Ka Wai Eric Cheng, for his patient, remarkable and valuable guidance. He is an outstanding and experienced supervisor. His constructive suggestions, optimistic attitude, and industrial experience deeply impress and inspire me. He not only ignites my research passion but also broadens my academic outlook. He gives me the courage to follow my research intuition. Without his help, I could not complete my Ph.D. study.

Secondly, I would like to express my admiration for Dr. Jiefeng Hu. He was my supervisor during the first year of my Ph.D. study. He opened the research gate to me and helped me to build some good research habits. Also, I would like to thank Dr. Ka Wing Chan for his generous help.

Then, I would like to express my great thanks to other research staff and friends who share weal and woe with me. They are Dr. Xiaofei Li, Dr. Yong Li, Dr. Xueqin Lei, Dr. Yun Yang, Dr. Zilin Li, Dr. Ming Liu, Dr. Yinghao Shan, Dr. Jinhong Sun, Dr. Yuan Yao, Dr. Junwei Liu, Dr. Martin Boissier, Dr. Lvping Fu, Dr. Yunpeng Zhang, Dr. Xing Zhao, Dr. Wenzheng Xu, Dr. Cuidong Xu, Dr. Xiangdang Xue, Dr. Minghao Wang, Dr. Kaiwen Chen, Mr. Chris Ip, Mr. Jerry Kan, Mr. Yingping Cao, Mr. Huihuan Wu, Mr. Daohong Wang, Mr. Kaiyuan Wang, Mr. Jie Mei, Mr. W.C. Mak, Mr. H. Wong, Mr. H.T. Wong, Anita, and Tina.

I also want to thank my university, graduate school (GS), Research and Innovation Office (RIO), EE department, general office (GO), and my lovely EF001 for their professional service and support throughout my study life. I would like to thank all my colleagues and friends. Special thanks to my dearest sister Cara Zhu and brothers Gray

Guo and Herman Wang. They light up my life in the dark hours. When I feel low, they give me the strength to carry on and overcome life challenges.

Last but not least, many thanks to my parents, Bo Wang and Xiaoxia Wang, for their endless love. I also thank my aunt Xiaohui Wang for her concern and love. And sincere gratitude goes to other family members, especially my grandmother, Lizhu Zhao. Without their emotional and physical support, I cannot pursue my dreams. Their love wirelessly powers me whenever possible.

Contents

List of Figures

XIV

XVI

List of Tables

List of Acronyms

AC	alternating current
AGVs	automatic guided vehicles
BHP	bipolar hexagonal pad
CC	constant current
CI	coupled inductor
CPT	capacitive power transfer
CV	constant voltage
DC	direct current
DSP	digital signal processor
DWPT	dynamic wireless power transfer
EBs	electric bicycles
EVs	electric vehicles
ETs	electric trains
EMC	electromagnetic capacity
EMF	electromagnetic field
EMI	electromagnetic interference
ESR	equivalent series resistance

FEA	finite element analysis
FHA	fundamental harmonics approximation
FPGA	field programmable gate array
ICEVs	internal combustion engine vehicles
ICNIRP	international commission on non-Ionizing radiation protection
IoT	Internet of Things
IPT	inductive power transfer
KCL	Kirchhoff's Current Law
KVL	Kirchhoff's Voltage Law
LCC	inductor–capacitor–capacitor
LED	light-emitting diode
MAX	maximum
MIN	minimum
MOSFET	metal-oxide-semiconductor field-effect transistor
MPPT	maximum power point tracking
PI	proportional and integral control
PID	proportional-integral-derivative
PV	photovoltaic
PCB	printed circuit board

PSC	phase shift control
PTE	power transfer efficiency
PWM	pulse-width modulation
RMS	root mean square
RVIPT	roadway vehicle inductive power transfer
TI	tapped inductor
VCR	voltage current relationship
WPT	wireless power transfer
ZPA	zero phase angle
ZVS	zero-voltage switching

List of Symbols

symbol	unit	description
B	T	flux density
C	F	capacitance
C_{air}	–	air resistance coefficient
C_P	F	capacitance of the primary resonant circuit
C_S	F	capacitance of the secondary resonant circuit
D	m	the distance between coils
d_{in}	mm	inner diameter of a spiral coil
d_{out}	mm	outer diameter of a spiral coil
d_w	mm	coil diameter
d	–	duty ratio
δ	–	conduction angle
ϕ	W_b	magnetic flux
f	Hz	frequency
f_s	Hz	switching frequency
H	A/m	magnetic field strength
i	A	instantaneous current

I_{in}	A	input DC current
I_o	A	output DC current
k	_	coupling coefficient
K_P	_	output variable of the PID proportional part
K_I	_	output variable of the PID integral part
K_D	_	output variable of the PID differential part
L	H	self-inductance
M	H	mutual inductance
M_t	H	total mutual inductance
m	kg	mass of coils
N	_	number of turns
N_{DD}	_	number of turns of a DD coil
N_Q	_	number of turns of a Q coil
P_{in}	W	input power
P_{out}	W	output power
R	Ω	resistance
R_{eq}	Ω	input equivalent load of the rectifier
R_L	Ω	resistive load

s_t	mm	spacing between two adjacent turns in a coil
t	seconds	time
μ	H/m	permeability
μ_0	H/m	space permeability
μ_r	_	relative permeability
v	V	instantaneous voltage
V_{in}	V	input DC voltage
V_O	V	output DC voltage
vol	mm^3	coil volume
ω	rad/s	angular frequency
ρ	kg/m^3	density
η	_	overall dc-dc efficiency
η_P	_	efficiency of the primary loop
η_S	_	efficiency of the secondary loop
$\dot{X}$	_	the phasor form of the parameter
Z	Ω	impedance
Z_{eq}	Ω	equivalent impedance
Z_{in}	Ω	input impedance

Z_P	Ω	primary network impedance
Z_r	Ω	equivalent reflected impedance
Z_S	Ω	secondary network impedance
Z_{Sn}	Ω	the input impedance of an S-resonant network
Z_{Tn}	Ω	the input impedance of a T-resonant network

Chapter 1

Introduction

1.1 Background of Wireless Power Transfer

Wireless power transfer (WPT) has been highlighted by numerous pioneering scientists. One famous prototype by Nikola Tesla, dating back to the last century, embarks on the journey of wireless charging research. Nevertheless, after the 1980s, there has been no practical WPT implementation for over half a century because of the limited development of two main components. One is from the cable material since WPT requires low winding resistance. The other is from the high-frequency equipment.

What makes WPT great again? One reason should be a revolutionary improvement from high-frequency power devices [1]. In the 1980s, power Metal-Oxide-Semiconductor Field-Effect Transistor (MOSFET) are commercially available, offering a practical way to convert DC to high-frequency AC. Especially, Silicon-Carbide (SiC) MOSFET takes an important role due to its high blocking voltage, low loss, and high-frequency operation [2]. SiC power electronic devices enable high efficiency and high power density, reducing energy dissipation and operating costs for high-frequency applications, thereby opening a new era of WPT [3].

In 2007, researchers from the Massachusetts Institute of Technology (MIT) demonstrated a WPT system that could transfer 60 W efficiency over 2 meters, which ignited the passion for WPT research again [4]. Thanks to its impressive benefits, such as non-contact, convenience, and user-friendliness, researchers have increasingly started paying attention to this beautiful technology. As a promising alternative to traditional conductive charging via cables, WPT offers more charging freedoms. For example, energy can be transferred without any physical contact; therefore, the physical limitations caused by conductive cables can be resolved. Nowadays, WPT has been

successfully integrated with a significant number of applications such as heating systems [5], consumer electronics [6], and electric vehicles (EVs) [7]. Among different applications, vehicular applications are one of the most promising products. With the campaigns to stop issuing of gasoline vehicle licenses by governments such as and Norway 2025, HK 2035, UK 2030, the research on transportation electrification has become increasingly necessary [8]. Intelligent chargers take an essential role in transportation energy sources. As a next-generation charging infrastructure, wireless power transfer must be an attractive topic for researchers worldwide.

1.2 Development of EV Charging Technology

As a promising alternative to gasoline-powered internal combustion engine vehicles (ICEVs), EVs are promising to alleviate the pollution problems due to their inherent advantages, e.g., zero pollution, energy-saving, low noise, etc. Thanks to incentive plans and subsidies from governments to promote zero-carbon emissions and green transportation, there is a race in EV technology leadership among worldwide automakers such as Tesla, BYD, Toyota, BMW, and Volkswagen groups to make their products to be dominant as quickly as possible in the market. This campaign also leads to plenty of EV research areas, especially in places where resource-saving and environment-friendly awareness is upheld. Although electrically vehicular applications show excellent performances as green transportation, the market is still not as active as it should be. The government subsidy and tax reduction incentives are still the main reason behind the increase in current market share [9].

The major bottleneck hindering EVs' development must be the electricity storage systems [10]. It is pretty challenging to design such a storage system to meet all stringent requirements simultaneously, e.g., high power density, low cost, long lifecycle, user-friendliness, safety, and reliability. These factors greatly limit the driving range of vehicular applications, which constitutes major practical bottlenecks for EV promotion. Currently, one bottleneck hindering EVs' popularization is the limited battery capacity. Therefore, it is urgent to develop efficient EV charging infrastructures and advanced

technologies to accelerate the commercialization of EVs [11]. With the help of advanced charging infrastructures, more miniature onboard battery packs, and extending cruising range, worldwide EV commercialization can be achieved [12]. In total, the charging infrastructures can be roughly divided into two parts: conductive charging and wireless charging.

1.2.1 EV conductive charging

Conductive charging involves the use of electric cables to charge electric vehicles. This method is further classified into on-board and off-board charging. Regarding the onboard charger, the EV is directly connected to the ac grid via a cable. Typically, the main components of a charger are installed at the vehicle's side, including the EMI filter, rectifier, and dc-dc converter, which reduces the cost and physical space required to construct the charging infrastructure. On the other hand, the main charging component is located on the ground. Comparing this to the former with light electronics and filter components for the sake of EV weight, the latter (off-board charging) uses a relatively heavy and high-power charging infrastructure. Thus, off-board charging enables fast charging, which enhances the efficiency of charging [13]. Admittedly, conductive charging can realize high-power density and charging efficiency. However, its limitations are also obvious. The installation of bulk charging cables requires a considerable amount of space. Additionally, there are some risks associated with conductive charging, such as electric shock, arcing, cable and connector aging, and electrocution [14].

Traditionally, conductive charging has been used to charge batteries in vehicular applications. However, wireless charging is becoming more widespread, as demonstrated in Fig. 1-1. At present, onboard batteries are charged by conductive charging plugs connected to the AC power supply [15]. However, the heavy gauge cables used to connect to the EV are difficult to handle, creating tripping hazards and exposing the system to vandalism [16].
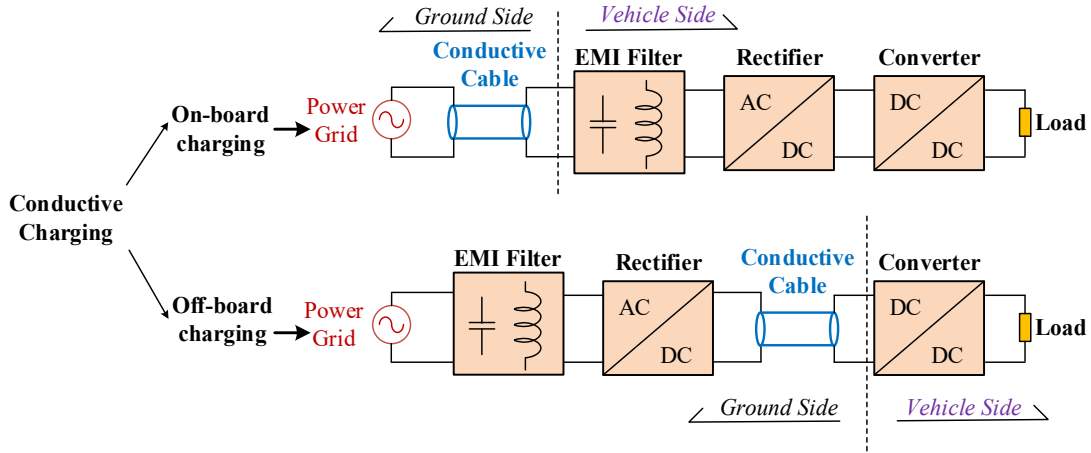
Fig. 1-1. The typical conductive charging method for electric vehicles.
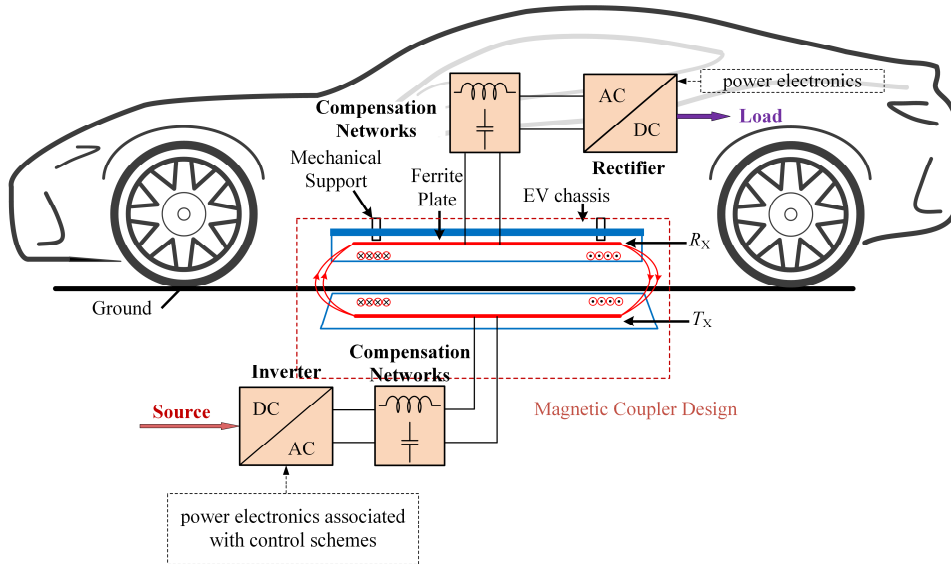
Fig. 1-2. The architecture of a typical wireless power transfer system.

1.2.2 EV wireless charging

When it comes to EV wireless charging, it has become a more and more attractive method thanks to its incredible merits [17], [18], as shown in Fig. 1-2. For example, such a technology avoids tangled wires and is integrated with the parking bay, thereby improving convenience [19]. Moreover, there is no need to plug in/out operations, eliminating abrasion and extending the service life of applications [20]. Compared with traditional conductive EV charging, WPT can avoid electric shock or arc, even

electrocution [21]. Due to its non-contact, risk like an electric shock, arcing, or electrocution can be avoided. The convenience can be greatly improved by EV wireless charging, including static wireless charging and dynamic wireless power transfer (DWPT) systems.

As an important means of intelligent charging, WPT significantly facilitates the electrification progress of vehicular applications by resolving the aforementioned problems in an alternative way. Instead of improving the energy storage itself, wireless charging ensures that vehicular applications can harness energy wirelessly in parking by stationary WPT systems and moving by dynamic WPT systems. The static wireless charger can be integrated into the parking lots in the public area. There is no need for extra space to install the charger, saving valuable space in metropolitans such as New York, London, Paris, Beijing, and Hong Kong [22]. As for the stationary IPT system, the drivers just need to park their car and leave [23]. Moreover, such user-friendliness can be further enlarged by dynamic wireless power transfer (DWPT) [24]. In terms of dynamic charging, vehicular applications can run without a stop. When vehicular applications are moving on the road, they can be continuously powered. The range anxiety can be further improved by dynamic charging. Theoretically, dynamic charging does not require any onboard battery. Instead, they utilize an onboard receiver pad to gain the energy from the transmitter laid on the ground. Thus, the driving range can be greatly extended as well as the weight of battery packages can be mitigated. For instance, if 20% of the roads possess a 40-kW dynamic charging system, the driving range of an EV can be extended by at least 80% [25]. And the battery capacity of vehicles equipped with wireless charging could be reduced to 20% or less compared to EVs with conductive charging [26]. The reduction in batteries may offset the implementation cost of the dynamic wireless charger. The waste due to the aged batteries can also be reduced.

As regards the IPT system, the SAE J2954 defines specific criteria for interoperability, electromagnetic compatibility, performance requirements, safety, and

testing requirements for static wireless charging for light-duty electric vehicles and plug-in electric vehicles. The adoption of a standard design guideline will ensure the interoperability of wireless charging infrastructures between manufacturers in different countries. The SAE J2954 technical information report [18] shows that TABLE 1-1 provides power levels and operating frequencies for static WPT charging. SAE J2954 stipulates that a single nominal frequency of 85 kHz must be used and that systems that compensate for various operating variations must achieve tuning within this band, as outlined in Table.

TABLE 1-1. J2954 SPECIFICATIONS

Charging Level	Power Level	Minimum Efficiency (%)	Minimum efficiency (offset)	Offset Range (mm)	Ground Clearance Class (mm)
WPT 1	3.7 kW	>85	>80		
WPT 2	7.7 kW	>85	>80	ΔX: ±75	Z1: 100-150
WPT 3	11.1 kW	>80	>80	ΔY: ±100	Z2: 140-210
WPT 4	22 kW	---	---		Z3: 170-250

Furthermore, compared to conventional conductive charging, WPT is more suitable for future vehicular applications [27]. The advantages of wireless charging are aesthetics, safety, convenience, and a fully automated charging process [28]. WPT can eliminate much charging troublesome, which is desirable by the EV owners [29]. Especially, WPT is suitable for different kinds of vehicular applications, which are not limited to automobiles but also includes other promising vehicular applications such as scooters, automatic guided vehicles (AGVs), electric bicycles (EBs), and electric trains (ETs). However, as EV application differs, the required output power level and design purposes of the WPT systems are different. In summary, this thesis covers several

important EV wireless charging systems, including electric scooters (Chapter 2), automatic guided vehicles (Chapter 3), electric bicycles (Chapter 4), electric trains (Chapter 5). As a promising charging method, WPT contributes to EVs with numerous advantages:

- User-friendliness: Wireless chargers can be integrated into parking lots, which saves valued space for metropolitans. There is no need for extra space to install the charger, which can save valuable space in metropolitans like New York, London, and Hong Kong.

- Safety: Energy can be transferred through the time-varying electromagnetic field; therefore, the risk of electric shock, arcing, or electrocution can be avoided.

- Robustness: WPT ensures stable charging even in harsh operation places such as underwater, toxic, and explosive environments.

- Intelligence: Compared to conductive charging, WPT is more suitable for future smart cities. It is easier to integrate with promising technologies, e.g., vehicular charging for EVs, since charging for the Internet of Things (IoT), and intelligent charging for the industry 4.0.

Overall, WPT technology provides a more convenient, intelligent, safe, and fully automated charging process. Thanks to these superiorities, wireless charging must be a promising option for EV chargers. Key research areas in wireless charging systems contain magnetic coupler design, compensation networks, and power electronics with advanced controlling schemes. Therefore, it is important to model all these three key parts from the view of physical abstraction.

1.3 The Modelling of WPT Systems

Fig. 1-3 depicts a typical WPT system model, including coil design, compensation networks, energy conversion devices, and associated control systems [30].
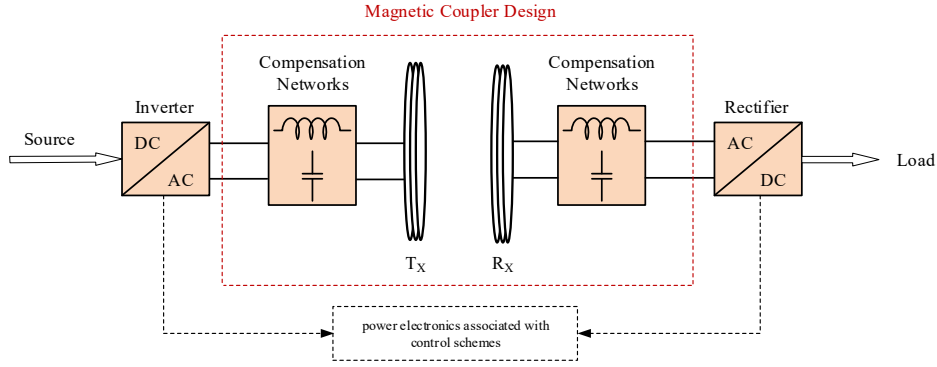
Fig. 1-3. The overview of a typical wireless power transfer system for EVs.

TABLE 1-2. REVIEW OF SEVERAL FERRITE-CORE COIL STRUCTURE

EE	II	UU	EI	UI

1.3.1 Coil Classification

Various geometries of primary and secondary windings, based on E-E, I-I, U-U, E-I, and U-I ferrite core combinations, are shown in TABLE 1-2. A significant disadvantage of the ferrite core structure in EV charging applications is the impact on the ground clearance due to the thickness of the ferrite core; therefore, it is necessary to modify the EV chassis to accommodate the charger. On the other hand, bumper-to-wall charging is not possible without extensive modifications to the vehicle's chassis. Hence, air-core type couplers are useful for wireless charging of electric golf carts, mine carts, and scooters [31].

Nowadays, air-core typed structures have been proposed to develop advanced magnetic couplers in WPT systems, as shown in TABLE 1-3. These structures can be roughly divided into two types: single-sided and double-sided, as illustrated in Fig. 1-4. Coil design is the key to IPT systems [32], [33]. For example, solenoid coils are proposed to constitute double-sided winding transformers [34]. Nevertheless, this flux-

pipe resonant type has intrinsic leakage flux, thereby leading to a low coupling coefficient. Nowadays, unipolar coils such as spiral coils and square coils are widely used in practice for consumer electronics like smartphones. However, the charging zone is limited, and the poor horizontal misalignment hinders the development. Hence, bipolar coil types, i.e., DD coils, are proposed for improving the charging range and horizontal misalignment tolerance [35]. Recently, there is an interesting Taichi coil [36], which seemingly manifests a bipolar characteristic. As for enlarging transmission distance with high efficiency, some promising coil combinations are investigated domino coils [37]-[40].
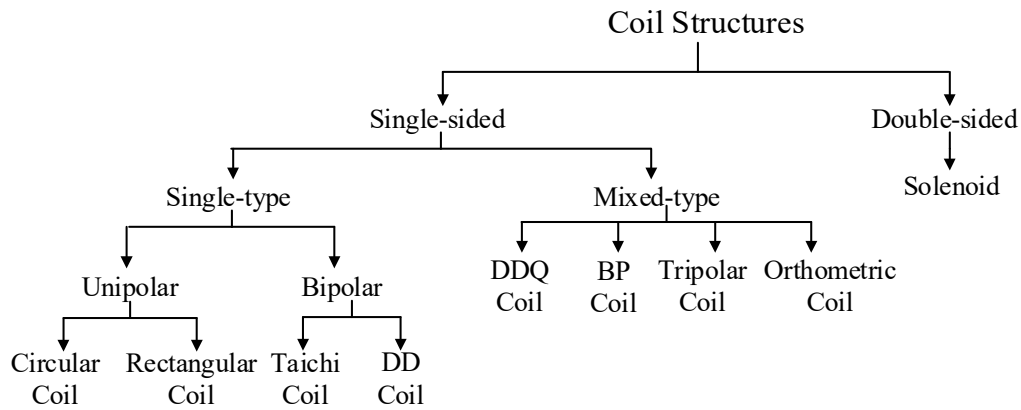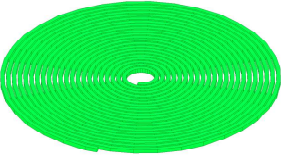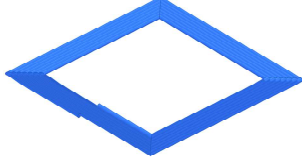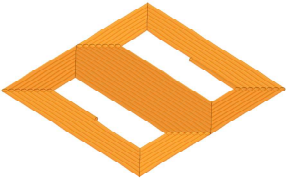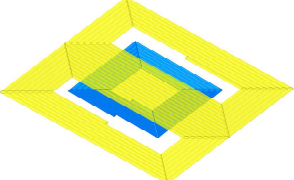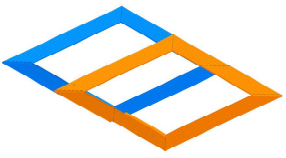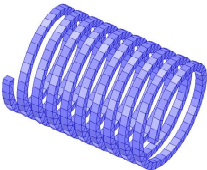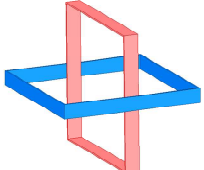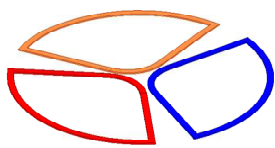
Fig. 1-4. The classification of air-core typed couplers.

TABLE 1-3. REVIEW OF SEVERAL AIR-CORE COIL STRUCTURE

The circular coil is the most common coil structure due to its simplicity and symmetry [41].	The rectangular coil is popular in dynamic wire power transfer, and it is extensible for constituting coil array [42].	The Taichi is a bipolar coil that can realize high misalignment tolerance [36].
The DD coil is a bipolar coil that offers high tolerance to lateral misalignment [35].	The DDQ coil is a combination between a Q coil and a DD coil. It increases the lateral misalignment tolerance in the non-door-to-door direction [35].	The bipolar pad (BP) can be excited independently to improve the misalignment tolerance [43].
The solenoid coil is a double-sided coil type, which is extremely suitable for domino WPT [44].	The orthometric coil is used in the omnidirectional situation for 3D WPT [45].	The tripolar shows better performance in 3-phase WPT [46].

1.3.2 Coil Modelling

1) The coupled-inductor modeling

Coil modelling plays an important role in magnetic coupler design. One popular way is coupled-inductor modelling, as shown in Fig. 1-5.
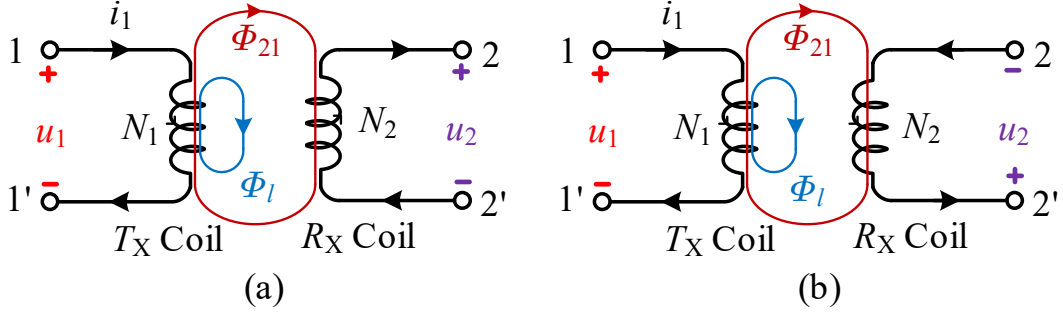
Fig. 1-5. Coil model of one typical WPT system with one transmitter coil and one receiver coil.

When the current flowing in the Tx coil is i_1, such a coil generates a coupled flux Φ_{21} with the Rx coil. Since Φ_{21} is time-varying, an induced voltage can be generated at the Rx coil according to the Faraday's law, which can be expressed as

$$u_2 = \frac{\mathrm{d}\psi_M}{\mathrm{d}t} = \frac{\mathrm{d}N_2\phi_{21}}{\mathrm{d}t} = \frac{\mathrm{d}Mi_1}{\mathrm{d}t} = M\frac{\mathrm{d}i_1}{\mathrm{d}t} \tag{1.1}$$

where ψ_M is the mutual flux linkage

$$\psi_M = N_2\Phi_{21} = Mi_1 \tag{1.2}$$

where M is the mutual inductance; however, the direction of the induced voltage and mutual flux linkage should comply with the right-hand screw rule. For instance, as illustrated in Fig. 1-5, the directions of u_2 are different according to different coil winding directions. Considering the difficulty in drawing the real winding directions like Fig. 1-5. A simplified method with dotted terminals is introduced to define the relationship between the current direction and the induced voltage direction, as shown in Fig. 1-6. Coil model of one typical WPT system with dotted terminals: (a) type A, and (b) type B. When the reference direction of current i and the induced voltage u_M are the same according to the dotted terminals, we can get

$$u_M = M\frac{\mathrm{d}i}{\mathrm{d}t} \tag{1.3}$$

Otherwise,

$$u_M = -M\frac{\mathrm{d}i}{\mathrm{d}t} \tag{1.4}$$
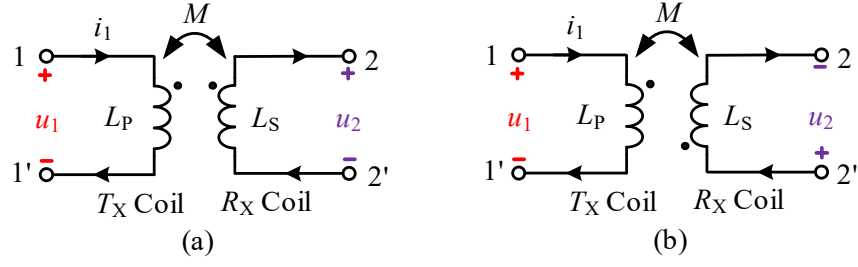
Fig. 1-6. Coil model of one typical WPT system with dotted terminals: (a) type A, and (b) type B.
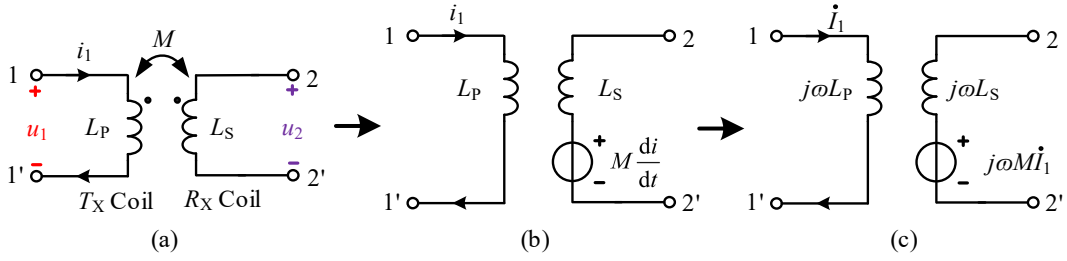
Fig. 1-7. Circuit diagram of type A: (a) dotted terminal circuit, (b) equivalent circuit with additional voltage sources in time domain form, and (c) equivalent circuit with additional voltage sources in phasor form.
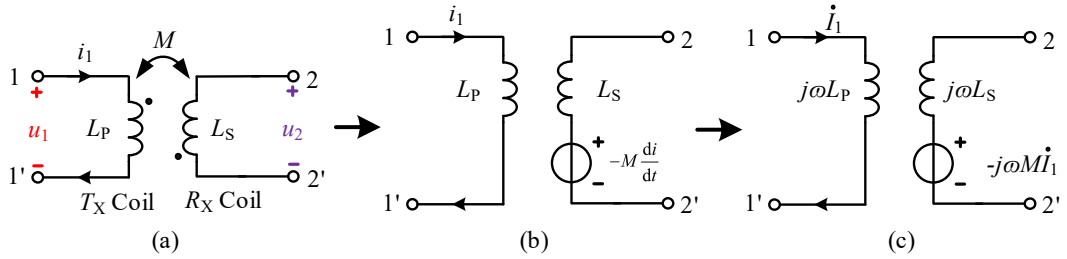
Fig. 1-8. Circuit diagram of type B: (a) dotted terminal circuit, (b) equivalent circuit with additional voltage sources in time domain form, and (c) equivalent circuit with additional voltage sources in phasor form.

To further simplify the system, it is widely to utilize the additional voltage source to represent the influence of mutual inductance. The circuit of a pair of coils, i.e., a transmitter coil and a receiver coil, are demonstrated in Fig. 1-7 and Fig. 1-8. When considering there is a current on the secondary side, the models can be redrawn as Fig. 1-9. Therefore, the voltages can be expressed as

$$u_1 = L_P \frac{di_1}{dt} + M \frac{di_2}{dt}$$
$$u_2 = L_S \frac{di_2}{dt} + M \frac{di_1}{dt}$$

(1.5)

Then, the phasor form can be rewritten as

$$\dot{U}_1 = j\omega L_P \dot{I}_1 + j\omega M \dot{I}_2$$
$$\dot{U}_2 = j\omega L_S \dot{I}_2 + j\omega M \dot{I}_1$$

(1.6)

where the dot version means the phasor form of the parameter
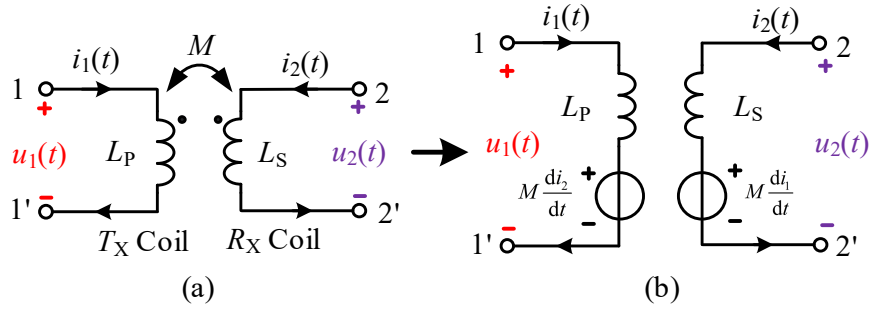
Fig. 1-9. Coil diagram of type A: (a) dotted terminal diagram, and (b) equivalent voltage source

diagram.

Similarly, if the dotted terminal is in a different position, the circuit scheme can be shown in Fig. 1-10. And the voltages can be expressed as

$$u_1 = L_P \frac{di_1}{dt} - M \frac{di_2}{dt}$$
$$u_2 = L_S \frac{di_2}{dt} - M \frac{di_1}{dt}$$

(1.7)

Then, the phasor form can be rewritten as

$$\dot{U}_1 = j\omega L_P \dot{I}_1 - j\omega M \dot{I}_2$$
$$\dot{U}_2 = j\omega L_S \dot{I}_2 - j\omega M \dot{I}_1$$

(1.8)

Similarly, it can be seen that the induced voltages are different at different terminal modes. Therefore, a two-coil WPT system can be reflected by such an equivalent circuit

with additional volage sources.
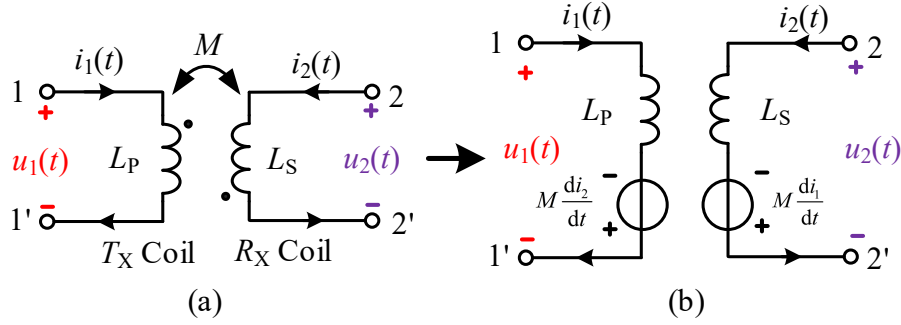
Fig. 1-10. Coil diagram of type B: (a) dotted terminal diagram and (b) equivalent voltage source diagram.

2) The equivalent modeling

As illustrated in Fig. 1-11, a T-model can be adopted for further simplifying modeling because the voltage-current relationship (VCR) is the same as the circuit in Fig. 1-10. Therefore, T-model is an equivalent model for the inductor modeling. Hence, the T-model is investigated to simplify the coil structure further.
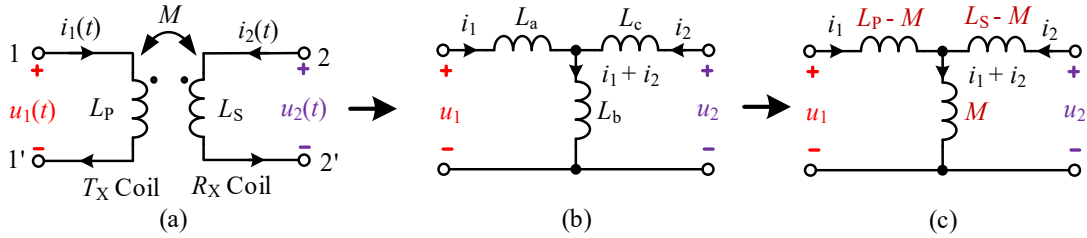
Fig. 1-11. The coupled inductor modeling and its equivalent T-model.

According to Kirchhoff's circuit law, the following equation can be gained as

$$
\begin{aligned}
u_1 &= L_a \frac{di_1}{dt} + L_b \frac{d(i_1 + i_2)}{dt} = (L_a + L_b)\frac{di_1}{dt} + L_b \frac{di_2}{dt} \\
u_2 &= L_b \frac{di_1}{dt} + (L_b + L_c)\frac{di_2}{dt}
\end{aligned}
\tag{1.9}
$$

To meet the same coefficients, the inductance values in the T-model can be expressed as

$$\begin{cases} L_a = L_P - M \\ L_b = M \\ L_c = L_S - M \end{cases} \qquad (1.10)$$

Similarly, the situation in Fig. 1.8 can also be redrawn in the T-model circuit, as shown in Fig. 1-12.

$$\begin{cases} L_a = L_P + M \\ L_b = -M \\ L_c = L_S + M \end{cases} \qquad (1.11)$$
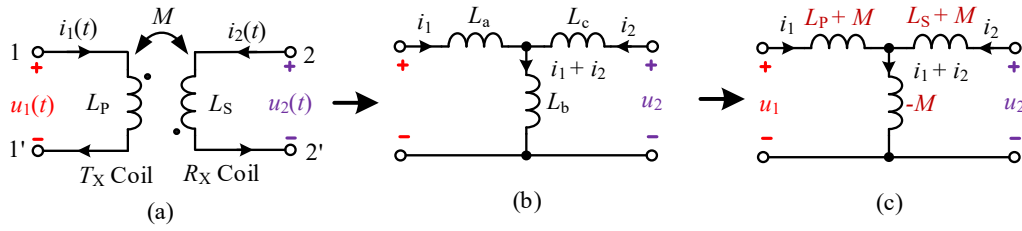
Fig. 1-12. The coupled inductor modelling and its equivalent T-model.

1.3.3 Modelling of Compensation Networks

One necessary part of IPT systems is the compensation networks. Conventionally, there are four basic compensation networks, namely, SS, SP, PS, and PP. Recently, high-order compensation networks such as LCC and LCL have been widely utilized.

In addition, intermediate circuits with high-order networks still need investigating. Fig. 1 illustrates two high-order compensation networks, i.e., LCL [47] and LCC [48]. In terms of LCL topologies, the self-inductance of two inductors, i.e., L_a and L_P should be the same. As for LCC types, the capacitor C_a partly compensates L_P to achieve the L_P' whose self-inductance equals L_a. Hence, the LCC compensation topology can be regarded as a supplement type for LCL topology [49].

In general, resonance is necessary for better system performance; thereby, capacitors are needed to tune the coils to make resonators. Specifically, a well-designed compensation network can achieve load-independent constant outputs, including CC and CV, minimize VA rating and maximize power transfer capability, suppress the

bifurcation phenomenon, and enhance efficiency [50].
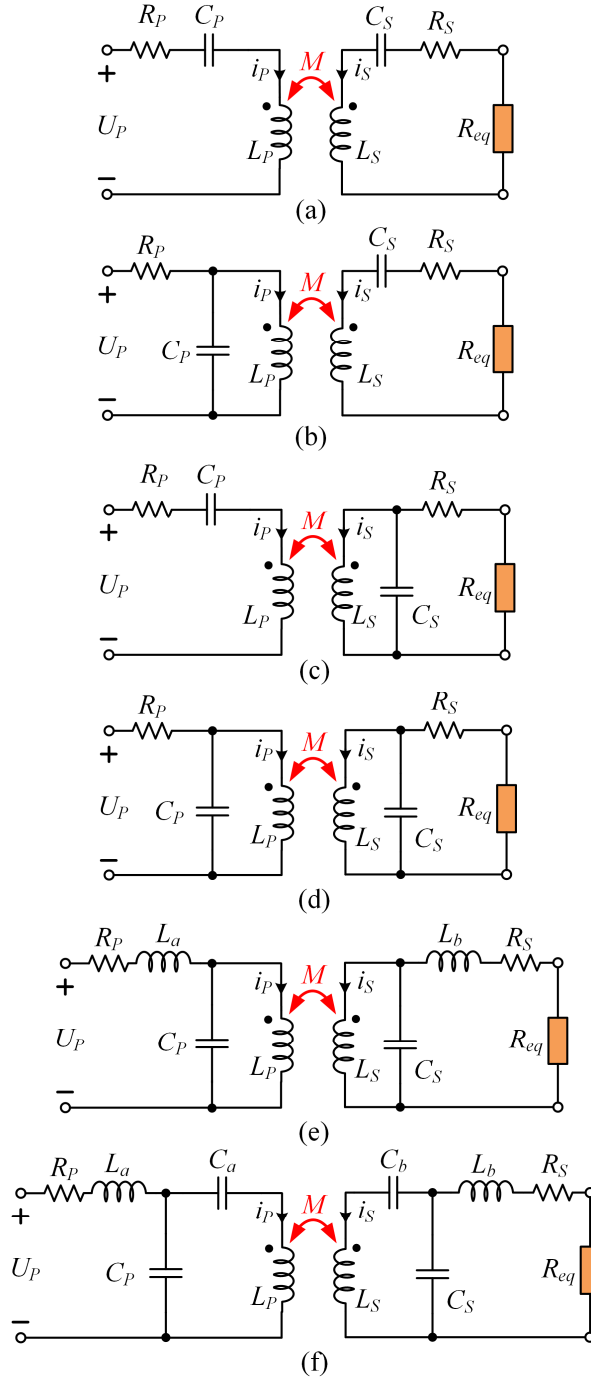
Fig. 1-13. Several Compensation networks: (a) SS (b) PS (c) SP (d) PP (e) LCL (f) LCC.

Basically, four compensation topologies, including SS, SP, PS, and PP are widely used in two-coil WPT, as shown in Fig. 1-13 (a)-(d). Recently, several high-order compensation topologies such as LCL and LCC have become more and more interesting owing to their special capabilities. As illustrated in Fig. 1-13 (e), LCL

topologies are proposed due to several advantages. Firstly, the current of primary inductance can be independent of the reflected impedance of the secondary circuit [51]. Secondly, LCL topologies are studied to improve misalignment tolerance and lower voltage stresses across compensation capacitors [52]. As demonstrated in Fig. 1-13 (f), LCC topology is composed of an inductor-capacitor-capacitor both on the primary and secondary sides. This topology can accomplish ZCS [53], and the inverter needs to supply the active power only with the primary-side load-independent current [54]. In other words, LCC is a supplementary topology for LCL, which can be seen in Fig. 1-14.
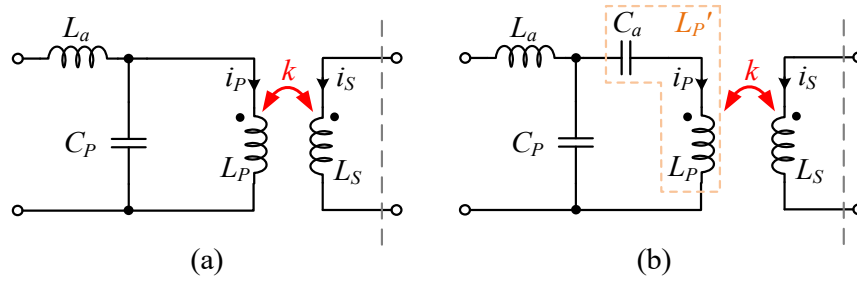
Fig. 1-14. High-order compensation networks: (a) LCL and (b) LCC.

1.3.4 Key Resonant Networks

Currently, voltage-source inverters are used almost exclusively as the power source for WPT systems rather than current-source inverters. Due to this, it is challenging to use P compensation with VSI because two voltage sources cannot be connected in parallel [55]. Therefore, this thesis also focuses on the series compensation at the source side.

In general, wireless power transfer discussed in this thesis is basically about magnetic resonance. Magnetic resonance means the energy oscillation between the magnetic field and the electric field. Therefore, inductors reflect the magnetic field in the electrical equivalent circuits, whereas the capacitors represent the electric field. Therefore, the LC resonant tank can reflect the magnetic resonance.

In terms of different resonant tanks, coils or inductors are compensated by capacitors to minimize volt-ampere (VA) rating and maximized power transfer capability. When tuning coils with capacitors, resonance can be generated. Therefore,

it is necessary to analyze different resonant circuits that are extremely useful for fast analysis in WPT systems. In this thesis, all the analyses are based on the exploration and investigation of key resonant circuits, including S-, T-, and Π-resonant networks.

(a) S-resonant network

The S resonant circuit is shown in Fig. 1-15. At the resonant frequency, the total impedance of an S resonant network is zero. That means it works like a short circuit because $Z_1 = -Z_2$, as shown in Fig.
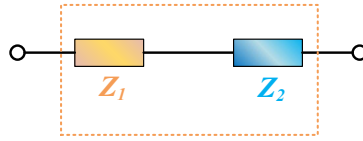
Fig. 1-15. S-resonant network.

(b) T-resonant network

The other one is the T-resonant networks, which are illustrated in Fig. 1-16. Because $Z_a = Z_c = -Z_b$, at the resonant frequency, the relationship between the input and the output can be gained as
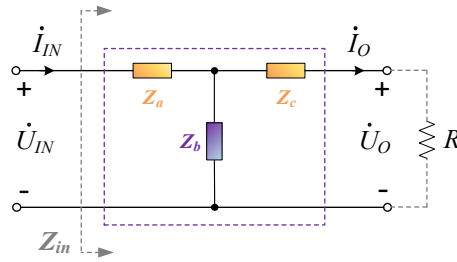
Fig. 1-16. T-resonant network.

(c) Π-resonant network

Remarkably, Fig. 1-17 illustrates a typical Π-resonant network, including input variables U_{IN}, I_{IN}, and Z_{IN} (i.e., voltage, current, and impedance) as well as output variables U_O and I_O (i.e., voltage, current, and impedance), respectively. R is the equivalent resistance.
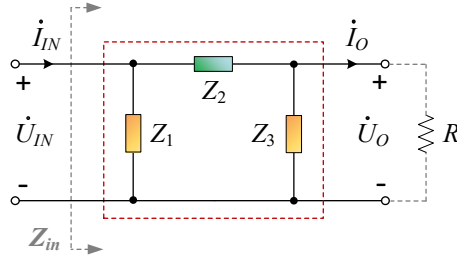
Fig. 1-17. Π-resonant network.

According to the two-port networks theory, the transfer matrix of this Π-resonant circuit shown in Fig. 1-17 can be obtained as follows

$$\begin{bmatrix} \dot{I}_{IN} \\ \dot{I}_O \end{bmatrix} = \begin{bmatrix} (Z_1 + Z_2)/Z_1 Z_2 & -1/Z_2 \\ 1/Z_2 & -(Z_2 + Z_3)/Z_2 Z_3 \end{bmatrix} \begin{bmatrix} \dot{U}_{IN} \\ \dot{U}_O \end{bmatrix} \tag{1.12}$$

The other one is the Π-resonant networks, which are illustrated in Fig. 1-18. Because $Z_a = Z_c = -Z_b$, at the resonant frequency, the relationship between the input and the output can be gained as
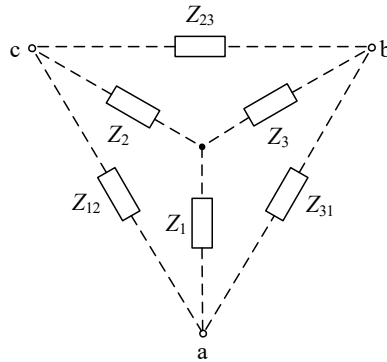
Fig. 1-18. The diagram of the conversion between T- and Π- resonant networks.

$$\begin{aligned} Z_1 &= \frac{Z_{31} Z_{12}}{Z_{12} + Z_{23} + Z_{31}} \\ Z_2 &= \frac{Z_{12} Z_{23}}{Z_{12} + Z_{23} + Z_{31}} \\ Z_3 &= \frac{Z_{23} Z_{31}}{Z_{12} + Z_{23} + Z_{31}} \end{aligned} \tag{1.13}$$

$$Z_{12} = \frac{Z_1 Z_2 + Z_2 Z_3 + Z_3 Z_1}{Z_3}$$

$$Z_{23} = \frac{Z_1 Z_2 + Z_2 Z_3 + Z_3 Z_1}{Z_1} \qquad (1.14)$$

$$Z_{31} = \frac{Z_1 Z_2 + Z_2 Z_3 + Z_3 Z_1}{Z_2}$$

1.4 Challenges in WPT for Vehicular Applications

To couple, or not to couple, that is a consideration of the application, technology, and managerial decision. One prerequisite for wireless charging is improving wanted couplings while reducing unwanted couplings. The wanted couplings ensure outstanding transferability such as load-independent outputs (Chapter 2-5), double/multiple charging objectives (Chapter 3), misalignment tolerance enhancement (Chapter 4-5), and charging while in motion (Chapter 5). However, undesirable cross-couplings always come along with the increasing number of coils from relay coils or additional transmitting and receiving coils.

a) Load-independent Outputs

Over the full range of the Li-ion battery charge, the battery pack equivalent load resistance, which is defined as the ratio of the charging voltage to the charging current, maybe roughly from a few ohms to several hundred ohms, as illustrated in Fig. 1-19.
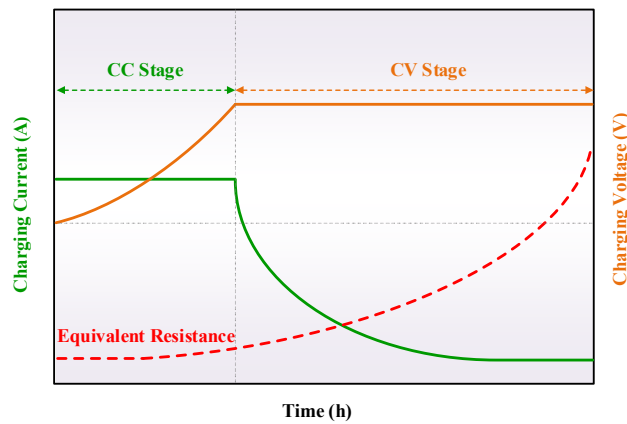
Fig. 1-19. A typical diagram of Lithium-ion battery charging characteristics.

With such a wide load range, a load-independent constant current/constant voltage (CC/CV) charging profile is desirable to ensure the battery's safety, durability, and performance in vehicular applications.

One classic method is to build feedback control between transmitting and receiving sides with the help of communication channels for regulating charging current and voltage in [56] and [57]. Nevertheless, the additional communication devices deteriorate both system cost and reliability. The interference between the energy transmission channel and communication signal channel also should be well considered. To avoid this, non-communication methods such as user-end converters have been proposed on the receiver side. This can significantly reduce their power density and increase the weight and size of battery packages [58]-[21]. Nevertheless, complicated control methods, such as primary side control [59], power flow control [60], dual side control [61], H_∞ control [62], and μ-synthesis approach [63] are generally adopted to regulate the converters for realizing good robustness against load and coupling variations. To avoid communication and complex control method, various high-order compensation networks like LCC or LCL are needed at the receiver side in achieving load-independent output charging in [64], [65], [66]. Such a compensated inductor not only brings bulky size and heavier weight for the EBs, but also lowers the power transfer efficiency in terms of non-negligible equivalent series resistances (ESRs). In practice, undesirable high-order harmonics may also arise from the resonance between the switched compensated inductors and parasitic capacitances. To resolve these issues, the special magnetic coupler design in this thesis offers a promising solution for load-independent charging for vehicular applications. Chapters 3-5 describe the design of the three-coil coupler, decoupling structure, Helmholtz resonator, and Q-DD-Q coil array, respectively. The essence is neither complicated control, nor communication method, but is the well-designed magnetic coupler with the beauty of simplicity.

b) Misalignment Tolerance

Misalignment tolerance should be given priority to vehicular wireless charging applications. A well-designed magnetic coupler minimizes the variation of magnetic couplings under a large range of misalignment [64]. The rotational, angular, and lateral misalignments need consideration since they may affect the charging performance. Specifically, Chapters 2 and 3 adopt DD coils. Chapter 4 utilize a special magnetic coupler that combines Helmholtz and spiral coils to improve misalignment tolerance. Chapter 5 adopts the Q-DD-Q coil sequence to enlarge the charging zone.

c) Zero Voltage Switching and Zero Phase Angle

Magnetic coupler design not only focuses on the coil but also involves the co-design with compensation capacitors. Zero voltage switching (ZVS) and zero phase angle (ZPA) ensure the high efficiency of the power electronic systems [67]-[70]. With the help of well-designed compensation capacitors, the inverter can achieve zero voltage switching (ZVS) or zero phase angle (ZPA).

On the one hand, a zero-voltage switching (ZVS) condition in Chapter 2 for the primary MOSFET-based inverter can be easily achieved to improve the system efficiency by slightly changing the value of a compensation component or the operating frequency.

On the other hand, Chapter 3 indicates the zero-phase angle (ZPA) between the input voltage and current, namely the unit power factor, can minimize the apparent power required and enhance the power transfer capability. As a result, the inverter only provides active power to the load, which lowers the volt-ampere rating and increases the efficiency.

The next section introduces the detailed solution from the perspective of the magnetic coupler. Chapters 2-5 mainly focus on utilizing a special magnetic coupler design to realize load-independent outputs, double/multiple charging channels, misalignment tolerance improvement, and dynamic wireless power transfer.

1.5 Objectives, Contributions, and Outlines

The purpose of this thesis is to design specific magnetic couplings for IPT systems in order to charge different types of vehicular applications, as demonstrated in Fig. 1-20. The key to successful design is to enhance the main magnetic couplings while simultaneously reducing the unwanted magnetic couplings. The design objective also includes enhancements to misalignment tolerance and power transfer capability. Overall, this thesis is arranged as follows.

Chapter 1 provides the background of the recent development of IPT systems and necessary modeling parts, including coils, compensation topologies, and associated control methodologies. A description of the motivation for this research, its objectives, and the outline of this thesis can be found in Fig. 1-20, which is organized as follows.

Chapter 2 highlights an electric-scooter-oriented magnetic coupler. Couplers of this type offer a general solution to enhance design flexibility in three-coil WPTs. This coupler eliminates the mutual inductance between the source coil and the receiver coil, thereby breaking the design limitations and facilitating the expression of intrinsic characteristics. In particular, load-independent CV output characteristics are analyzed and validated. Comparative analyses are conducted under aligned and misaligned conditions. An H-bridge power converter, a typical power electronic circuit for the WPT application, has been used in experimental verification. An experimental prototype has been constructed in order to verify the feasibility of the proposed approach, and the experimental results show good agreement with the theoretical analysis. The proposed WPT system can achieve a measured overall dc-dc power transfer efficiency at 83.3% with a 14 cm air gap when delivering 320 W to 20 Ω load. The proposed design can be generalized to other output voltages or power levels to fulfill different charging needs.
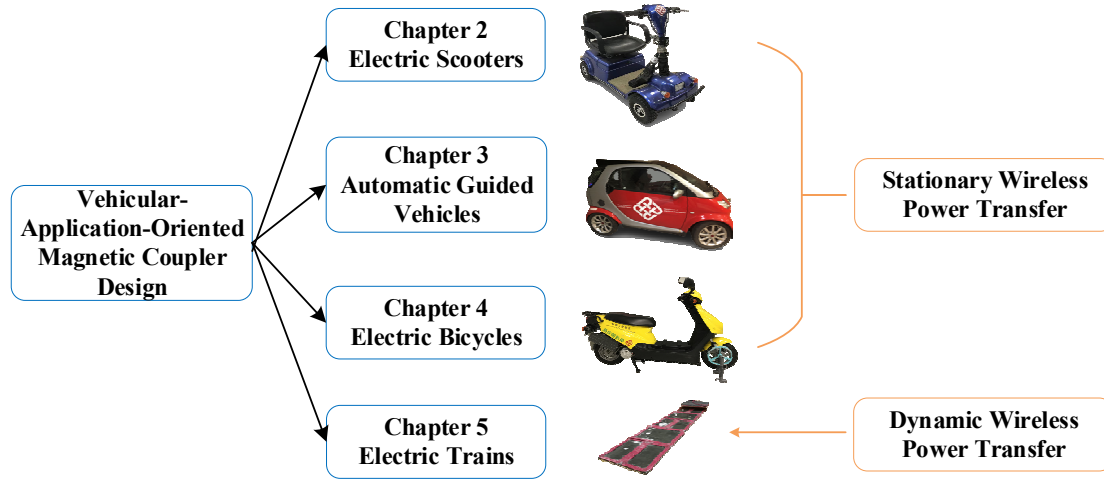
Fig. 1-20. Outline of the topics included in this thesis.

Chapter 3 introduces a novel double-receiver magnetic coupler for AGVs or other independent-work devices. When cross-couplings between the receivers and the source coil are eliminated, both receivers can produce load-independent outputs. Once the cross-coupling between the two receivers has been eliminated, neither receiver can influence the other. As a result of the proposed system, engineers are free to design magnetic couplers according to the practical design requirements of different engineering applications. Due to its flexibility and suitability for these applications, the decoupling approach proposed here relies on shapes rather than the intricate design of turns. Furthermore, there is no complex control or extra reactance, which enables a compact and straightforward system. Additionally, the inverter is capable of achieving ZPA, which can reduce the volt-ampere rating and increase efficiency. For the purpose of verifying the characteristics of the proposed system, an experimental prototype with dual receivers was constructed. Experiments indicate a remarkable agreement between theoretical and experimental results. Despite varying load conditions, the voltage of each receiver remains constant, resulting in high reliability. Finally, the prototype can achieve a 90.2% maximum dc-dc efficiency at 12 cm air gaps when delivering 518 W to loads. The proposed system can be generalized to other voltages and power levels to meet different charging needs, especially for devices with two independent power supplies and a fixed operating frequency, like AGVs, or two movable and independent-working devices.

In Chapter 4, a new approach for resonator design based on switched S-SP/S compensation and Helmholtz transmitter coils is discussed for wireless power transfer (WPT) systems for electric bicycles (EBs). Using the newly developed resonators, battery loads can be charged at constant currents (CC) and constant voltages (CVs) without the drawbacks of conventional methods such as variable mutual inductance, feedback between the transmitter and receiver, and complex control strategies. Simulations and experiments have both validated the merits of the proposed resonator design. Then maximum efficiency can reach 97.17% in the CC charging mode, whereas 91.17% in the CV charging stage. Since the efficiency variation in CC mode and CV mode is just 0.66% and 0.65%, respectively, it can be regarded as stable when Rx moves from 0 to 100 mm.

Chapter 5 discusses an improved magnetic coupler for segmented DWPT with high power and voltage. A system of this type can provide a maximum output power of 2.5 kW at a 500 V output voltage. In this integrated and improved design, the transmitter coil has been refined, resulting in a more stable operation. Magnetic couplers are well designed to provide safe operation in applications requiring high power. The parallel inverter is used to increase the power level and reduce the voltage or current stress on semiconductors. In addition, the Q-DD-Q switching sequence is proposed. A clarification of the connection method is provided for Q-shaped coils and DD coils. In each group, three transmitters Q-DD-Q have been energized, ensuring a stable operation. It also achieves a balance between reducing the variation in output voltage and the number of energized transmitters. Tests have been conducted in the laboratory at the 85 kHz operating frequency. The experimental results indicate that the output voltage of the DWPT is stable and constant when it is moving. The dc-dc efficiency can reach approximately 85% from 100 Ω to 200 Ω loads. Future work will be devoted to resolving the current distortion, achieving zero phase angle for the entire system, and improving the lateral misalignment tolerance.

Chapter 6 summarizes the main novelty and contributions of the thesis. A few remaining issues and future work, such as three-phase and Hyperloop wireless charging

systems, are also discussed, and some suggestions are made to follow market and research trends.

Overall, this thesis is dedicated to developing a special magnetic coupler for different vehicular applications, which are promising to electric automobiles, scooters, automatic guided vehicles, electric bicycles, electric trains, etc. Specifically, magnetic coupler designs for stationary wireless power transfer are discussed in Chapter 2 – Chapter 4. One Magnetic coupler design for dynamic wireless power transfer is discussed in Chapter 5. All designs are validated by simulation and experimental tests. Presented magnetic couplers realize both coupling and decoupling mechanisms for different purposes, including misalignment tolerance enhancement, load-independent outputs, and cross-coupling elimination.

Chapter 2

Three-coil WPT Coupler for Electric Scooters

Magnetic coupler design is the soul part of WPT systems. Among various couplers, the three-coil magnetic coupler is promising due to its extended transmission distance and high efficiency. In this chapter, a three-coil magnetic coupler is studied to wireless charge electric scooters. The presented coupler enhances the major magnetic coupling and reduces the unwanted coupling.

2.1 Introduction of Electric Scooters

As one of the most popular vehicular applications in numerous developing countries, electric scooters currently dominate the market [71]. Mobility scooters are gaining increasing attention from governments and customers as environmentally friendly and carbon-free transportation devices, especially for elderly people and people in need [72] [73]. Nevertheless, one major bottleneck must be related to the limited lifetime of energy storage devices, such as lithium-ion batteries. As an energy storage device, Li-ion batteries typically have a capacity of 4,000 charge/discharge cycles [74]. For such a problem to be resolved, it is necessary to develop an effective charging infrastructure. Wireless charging must be an effective method [75], [76].

For such a device to provide efficient energy transfer, it must also have design freedom and efficiency. As depicted in Fig. 2-1, scooters tend to be easier to use in the y-direction while they are more difficult to maneuver in the x-direction [77]. Hence, magnetic couplers are designed to improve x-misalignment tolerance in this thesis.
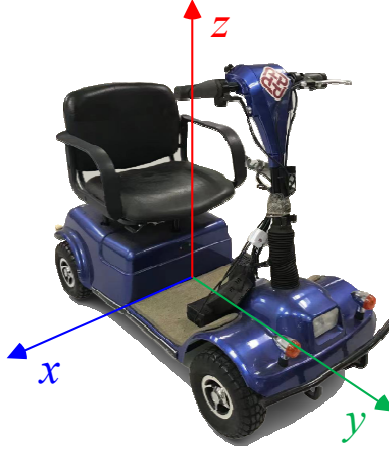
Fig. 2-1. The diagram of an electric scooter.

By implementing a special magnetic coupler based on a three-coil WPT, the degree of design freedom is increased since mutual inductance is eliminated between the receiver and source coils. For instance, the unipolar Q coil, the mixed QDD coil, and the bipolar DD coil are designed respectively to serve as a source coil, a transmitter coil (T_X), and a receiver coil (R_X). Magnetic decoupling is achieved by combining unipolar and bipolar coils. Additionally, the new coupler is capable of maintaining a high degree of efficiency under varying conditions of lateral misalignment. An experimental prototype of the proposed structure has demonstrated that the structure can realize inherent properties, improve misalignment tolerance, and transfer energy. The presented three-coil system can be generalized to be used in EV systems, especially scooters. To better understand the presented structure, it is essential to have an overview of three-coil WPT systems.

2.2 Review of Three-coil WPT

Three-coil WPT systems typically consist of a transmitter (T_X), a relay coil, and a receiver coil (R_X) [78-81]. In general, there are four typical types of three-coil WPT systems, including type-A to -D, as demonstrated in Fig. 2-2. The classification is made based on the relevant positions of the three coils and the value of mutual inductance between the transmitter coil and the receiver coil, i.e., M_2. Detailed categorizing

information is described in TABLE 2-1.

TABLE 2-1. ONE CLASSIFICATION OF THREE-COIL WPT SYSTEMS

Three-coil WPT with nonnegligible M_2	Three-coil WPT with negligible M_2		
Type A	Type B	Type C	Type D
[82, 83]	[84, 85]	[86, 87]	[78, 79, 81, 88-90]
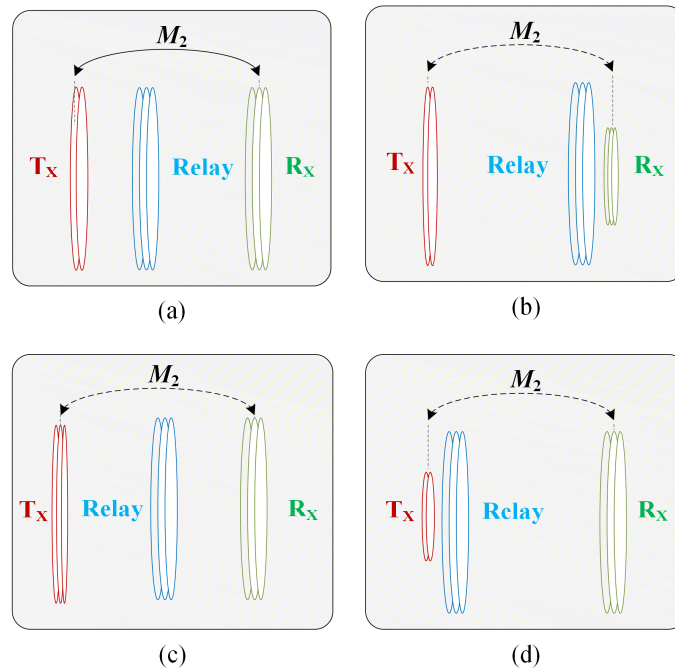
Fig. 2-2. Four typical types of three-coil WPT: (a) Type A. (b) Type B. (c) Type C. (d) Type D.

Specifically, type A is the scenario with the nonnegligible M_2. Contrary to this, M_2 can be designed to be so small that it is negligible in type B to D. Type B refers to the placement of the relay coil next to the receiver. In type B, the load impedance can be reflected to achieve an optimal value, thus achieving optimal load impedance and high power delivery [84]. In terms of type C, the relay coil is placed to be equidistant between the transmitter and the receiver in order to ensure expected mutual inductances [86] or the desired voltage gain [87].
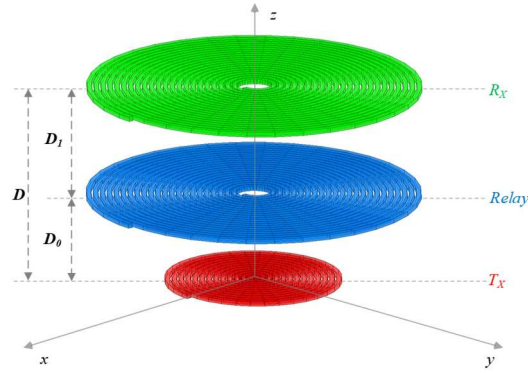
Fig. 2-3. The scheme of the coupling structure.

Due to its intrinsic superiority, i.e., the extended transmission range with high efficiency, type D is widely adopted at present. It is a normal practice of type D to shrink the size of the transmitter coil to achieve an extremely small M_2 with an extended transmission distance. That means the influence from M_2 can be ignorable. In addition, the relay coil of type D saves space because it does not take up as much space between the transmitter and receiver as traditional two-coil structures do. Thus, the coupling structure in this chapter consists of three coils in total, namely, transmitter (T_X), relay, and receiver (R_X) are demonstrated in Fig. 2-3. The airgap between T_X and relay is D_0 while the airgap between relay and R_X is D_1. Particularly, D represents the transmission distance from T_X to R_X, which is also the sum of D_0 and D_1.

2.3 Introduction of three-coil WPT coupler for scooters

2.3.1 Magnetic Coupler Structure

In practical applications, constant source supplies, such as CV supplies, are preferred for stable operation with a wide range of loads [50], [88]. In order to achieve a load-independent CV output, a number of methods can be employed. Accessional compensation networks such as LCC and LCL can be employed as a means of compensation [50]. They have the advantages of being simple in construction and easy to install. However, these compensation networks are bulky and result in a loss of power. Alternatively, dc-dc converters can be used, but complex strategies are required to

regulate the output voltage. [88], [63]. It has been reported recently that the three-coil WPT provides load-independent CV outputs, thus eliminating the requirement for additional compensation topologies, complex control methods, and their corresponding drawbacks. [89].

A number of methods are employed to produce load-independent CVs. The use of accessional compensation networks, such as LCC or LCL topologies, is one way to achieve this goal [50]. Simple structures and ease of installation are their main advantages. However, these compensation networks result in a bulky system and an increase in power consumption. Another option is to use DC-DC converters, but complex strategies are necessary to regulate the output voltage [88], [63]. Recent studies have examined three-coil WPT to provide load-independent CV outputs. This eliminates the need for additional compensation topologies, complex control methods, and the associated disadvantages [89].

In recent years, three-coil systems have attracted increasing attention because of their high efficiency and long transmission distance [78], [79]. In addition, well-designed three-coil systems tend to exhibit excellent properties, such as constant voltage (CV) output regardless of load variations [88].
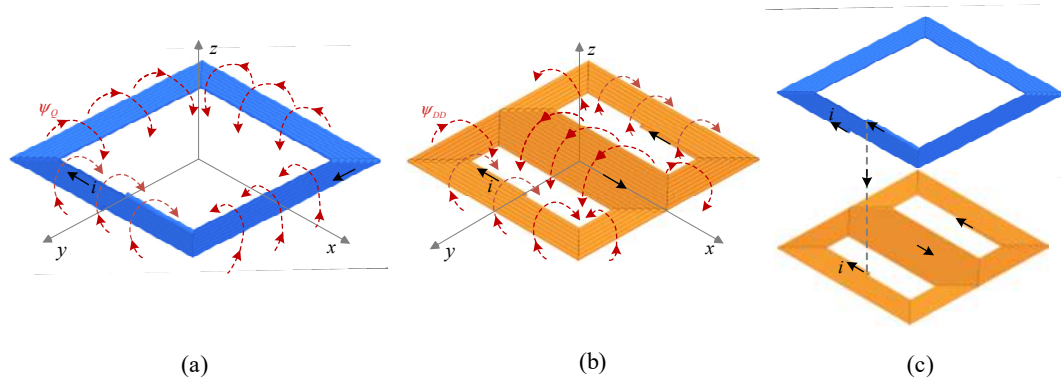
Fig. 2-4. The diagram of structures: (a) Q coil, (b) DD coil, and (c) QDD coil.

Typical practice for three-coil WPT systems is to place the source coil on the same plane as the transmitter coil or close to it, such as [79]-[88] and [89]-[92]. Generally, this practice has two main advantages: 1) Compactness: even though this system

contains three coils, the intermediate coil does not occupy much space compared to two-coil systems. 2) High Efficiency: Zhong *et al.* [79] and Zhang *et al.* [78] point out that it can be improved with the system efficiency because the input impedance can be adjusted to a larger value.

In fact, the QDD coil is an overlap combination between traditional Q and DD coil through series connection, as shown in Fig. 2-4. When the excitation currents are in phase, the structure of the Q and DD coil with corresponding magnetic flux is shown in Fig. 2-4 (a)-(b). For the Q transmitter coil, the generated magnetic flux is single-sided, and the polarity depends on the phase of its excitation current. For the DD transmitter coil, the generated magnetic is double-sided due to the symmetrical coil structure [93], [94]. In other words, the Q coil is unipolar while the DD coil is bipolar.

A null coupling coefficient can be achieved between a Q coil and a DD coil under overlapped conditions [24, 93, 94]. The effect of null magnetic coupling can be reflected through induced voltages, as shown in Fig. 2-5. In the unipolar magnetic field generated by an overlapped Q coil, the induced voltage of a DD coil U_{DD} is 0 ($U_{DD}=U_{da}-U_{db}=0$), as shown in Fig.2.5 (a). Similarly, in the bipolar magnetic field generated by an overlapped DD coil, the induced voltage of a Q coil U_Q is 0 ($U_Q=U_{qa}-U_{qb}=0$), as shown in Fig.2.5 (b).
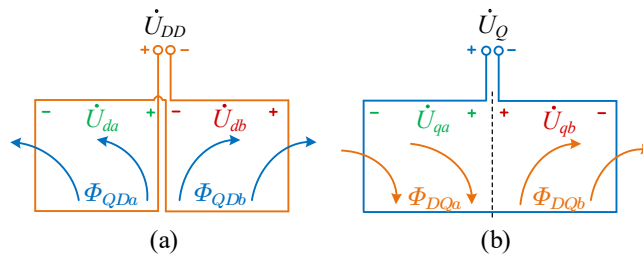
Fig. 2-5. (a) The induced voltage of the DD coil with the flux Φ_{QDa} and Φ_{QDb} generated by the Q coil and (b) The induced voltage of the Q coil with the flux Φ_{DQa} and Φ_{DQb} generated by the DD coil.

Also, research in [35] indicates that DD and QDD coils show good performances against misalignment. Nevertheless, DD and QDD coils are not well investigated for the same purpose in terms of three-coil WPT systems.

Hence, a new magnetic coupler structure for three-coil WPT for EV charging is proposed to resolve the aforementioned problems. The key contributions are summarized as follows:

1. This special magnetic coupler overcomes a number of design limitations, including coil sizes and transmission distance requirements. As a result, these parameters are no longer limited by the mutual inductance between the source coil and the receiver coil. The unwanted mutual inductance is theoretically eliminated by the Q source coil naturally decoupling from the DD receiver coil.

2. It is proposed that the Rx coil structure, as well as the upper portion of the Tx coil, will reduce electromagnetic leakage, thereby improving electromagnetic compatibility (EMC) with the help of DD coils [95].

3. Load-independent CV output can be achieved. There are no additional LCC/LCL compensation topologies or DC-DC converters in the proposed structure, which makes it compact and simple.

4. This proposed structure can enhance overall efficiency compared with the corresponding QDD-DD two-coil counterpart. In addition, this chapter makes use of bipolar coils to improve the lateral misalignment tolerance in comparison to the traditional three-coil WPT, which commonly uses circular, helical, or rectangular coil structures.

Fig. 2-6 (a) shows the exploded view of the proposed magnetic coupler consisting of three coils: source coil, transmitter coil, and receiver coil. Specifically, the source coil is a purely Q-shaped coil. The transmitter coil is a serial connection between a Q-shaped coil and a DD-shaped coil, namely a QDD-shaped coil. The receiver coil is a DD-shaped coil. Even though there is almost no magnetic coupling between the source coil and receiver coil, the power can still be transferred thanks to the transmitter coil. It receives energy originating in the source coil and resends energy, eventually to the receiver coil. The limitation of the shape of the coils is the misalignment tolerance enhancement is not omnidirectional. This results in only x-direction misalignment

tolerance being improved. Therefore, this design is very suitable for electric scooters.

The whole assembly view is shown in Fig. 2-6 (b). The source coil and the transmitter coil are placed compactly. The distance between the source coil and the receiver coil is **D** fixed as 14cm to comply with the industrial requirements for EVs. One real example is the ground clearance of the Tesla Model 3 is 13.97cm (5.5in) [96]. The separation or transmission distance **D** is supposed to be fixed. The change of the separation or transmission distance would change mutual inductances, thereby further changing the output voltage. Besides, the distance between the transmitter coil and the source coil is ignored because they are almost on the same plane. In total, the whole system contains four pieces of coils, including two identical Q-shaped coils and two identical DD-shaped coils. Detailed size information is shown in Fig. 2-7.

(a)   (b)
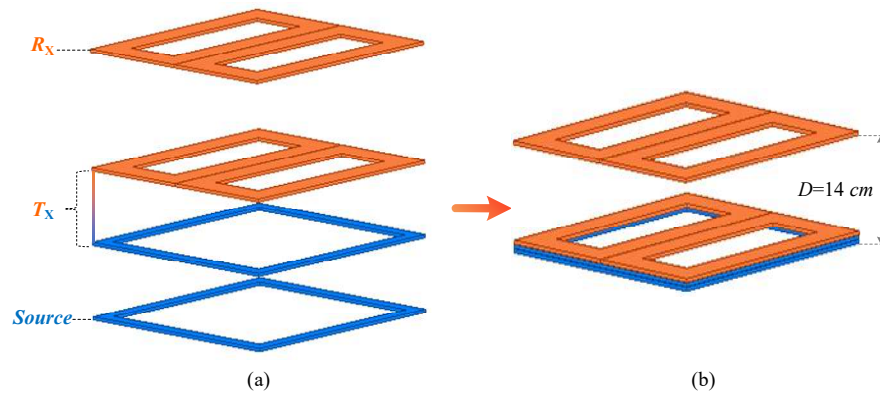
Fig. 2-6. Diagrams of the proposed magnetic coupler (a) Exploded view and (b) The whole assembly view with the airgap D.
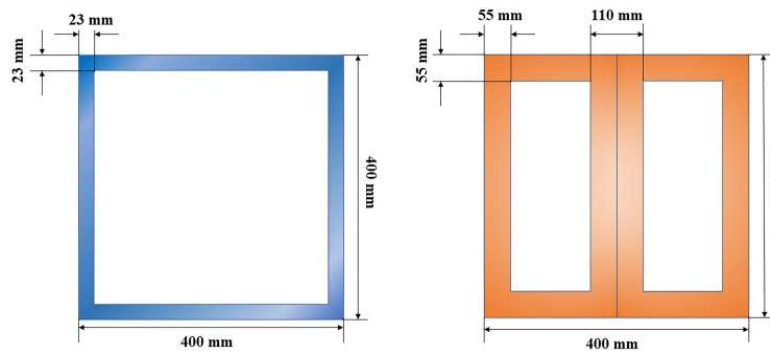
Fig. 2-7. Sizes of the proposed magnetic coupler.

2.3.2 Circuit Analysis

The circuit scheme of the proposed three-coil WPT system is shown in Fig. 2-8. The operating angular frequency of the inverter is ω, and the input dc voltage of the inverter is V_{in}. The H-bridge inverter is equipped at the source side to convert the dc power into 85kHz ac power for supplying the source coil. The inverter can be controlled by using the phase-shift method [89]. L_S, L_T, and L_R are the self-inductances of the source coil, the transmitter coil, and the receiver coil, respectively. C_S, C_T, and C_R are the resonant capacitors used to compensate L_S, L_T, and L_R correspondingly. A full bridge rectifier is constituted of four diodes D_a-D_d and one capacitor C_d for feeding the load R_L. The mutual inductance between the source coil and the transmitter coil is M_1. The mutual inductance between the transmitter coil and the receiver coil is M_3. The mutual inductance between the source coil and the receiver coil is M_2, which is eliminated thanks to the proposed magnetic coupler, i.e., $M_2 = 0$ theoretically.
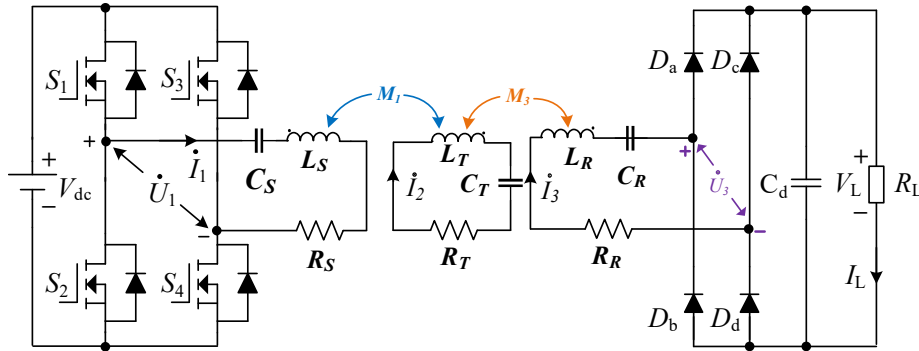
Fig. 2-8. Circuit scheme of the proposed three-coil WPT system.

The fundamental harmonics approximation (FHA) method is used to analyze the proposed WPT system. The fundamental component of the output voltage of the inverter is given as [97], [98]

$$u_1(t) = \frac{4}{\pi} V_{in} \sin\frac{\delta}{2} \sin\omega t \qquad (2.1)$$

where δ is the conduction angle of $u_1(t)$ as shown in Fig. 2-9.
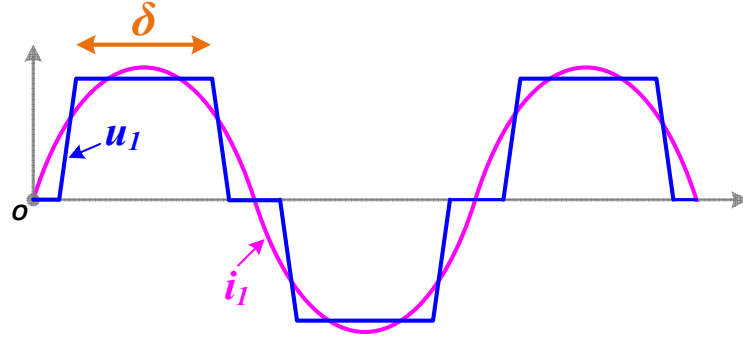
Fig. 2-9. The diagram of output voltage u_1, and output current i1 of the inverter under phase-

shifted modulation.

Then, the fundamental phasor root mean square (RMS) form of $u_1(t)$ can be expressed as

$$\dot{U}_1 = \frac{2\sqrt{2}}{\pi} V_{in} \sin\frac{\delta}{2} \angle 0° \tag{2.2}$$

The equivalent RMS value of the rectifier input voltage U_3 can be described as

$$\dot{U}_3 = \frac{2\sqrt{2}}{\pi} V_L \tag{2.3}$$

where V_L is the output voltage on the load.

R_{eq} is the input equivalent load of the rectifier that can be derived as

$$R_{eq} = \frac{8}{\pi^2} R_L \tag{2.4}$$

2.3.3 Resonant Networks

In general, self-inductance L_S, L_T, and L_R networks are compensated by capacitors to minimize volt-ampere (VA) rating and maximized power transfer capability [50]. Two resonant networks are taken into consideration, namely, S resonant network and T resonant network.

The S resonant circuit is shown in Fig. 2-10 (a). At the resonant frequency, the

total impedance of an S resonant network is 0. That means the resonant network works as a short circuit because of $Z_1 = -Z_2$.
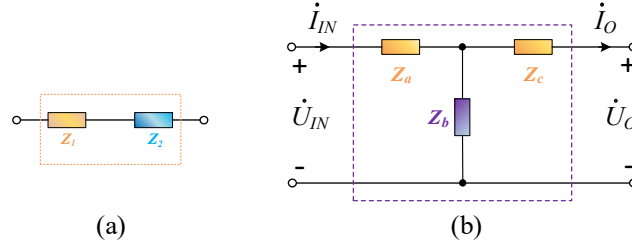
Fig. 2-10. Resonant networks: (a) S-resonant network and (b) T-resonant network.

The T resonant circuit is shown in Fig. 2-10 (b) [99], [100]. Because $Z_a=Z_c=-Z_b$ at the resonant frequency, the relationship between the input and the output can be gained as

$$\begin{bmatrix} \dot{U}_{IN} \\ \dot{U}_O \end{bmatrix} = \begin{bmatrix} 0 & -Z_b \\ Z_b & 0 \end{bmatrix} \begin{bmatrix} \dot{I}_{IN} \\ \dot{I}_O \end{bmatrix} \tag{2.5}$$

2.3.4 Equivalent Decoupling Circuit with Analysis

The equivalent decoupling circuit of the proposed three-coil WPT system is shown in Fig. 2-11, where S_1, S_2 and S_3 are S resonant networks while T_1 and T_2 are T resonant networks. R_{eq} is used in this equivalent circuit for simplifying analysis.
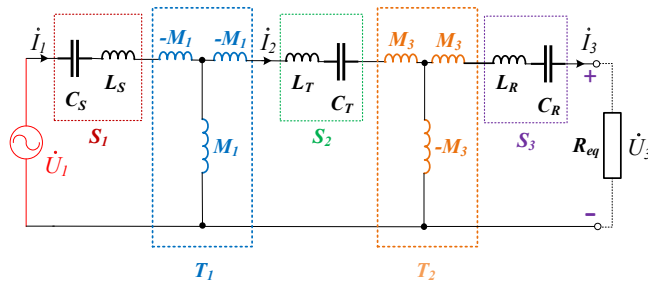
Fig. 2-11. Equivalent decoupling circuit of the proposed three-coil WPT system.

To tune the coils, self-inductances L_S, L_T and L_R are supposed to be compensated by capacitors C_S, C_T, and C_R respectively for constituting S resonant networks [88]. Thus, the operating angular frequency of the inverter is formed by S_1 to S_4. ω should satisfy the following relationships:

$$\omega = \frac{1}{\sqrt{L_S C_S}} = \frac{1}{\sqrt{L_T C_T}} = \frac{1}{\sqrt{L_R C_R}} = 2\pi f \qquad (2.6)$$

where *f*, the H-bridge inverter's switching frequency, is set to be 85 kHz according to the SAE J2954 standards for EVs [101].

Concerning S resonant networks, the following equations can be established:

$$\begin{cases} Z_{S_1} = j\omega L_S + \dfrac{1}{j\omega C_S} = 0 \\[2mm] Z_{S_2} = j\omega L_T + \dfrac{1}{j\omega C_T} = 0 \\[2mm] Z_{S_3} = j\omega L_R + \dfrac{1}{j\omega C_R} = 0 \end{cases} \qquad (2.7)$$

where Z_{S1}, Z_{S2}, Z_{S3} are the impedance of resonant networks S_1, S_2, S_3, respectively.

As for T_1 resonant networks, the relationship between U_1 and I_2 is given as

$$\dot{U}_1 = -j\omega M_1 \dot{I}_2 \qquad (2.8)$$

Similarly, the relationship between U_3 and I_2 from T_2 is derived as

$$\dot{U}_3 = -j\omega M_3 \dot{I}_2 \qquad (2.9)$$

The relationship between U_1 and U_3 from (2.8) and (2.9) should be obtained as

$$\frac{\dot{U}_3}{\dot{U}_1} = \frac{M_3}{M_1} \qquad (2.10)$$

Substituting (2.2) and (2.3) into (2.11), the relationship between V_L and V_{in} can be gained as

$$\frac{V_L}{V_{in}\sin(\frac{\delta}{2})} = \frac{M_3}{M_1} \qquad (2.11)$$

Therefore, the load-independent output voltage V_L can be expressed as

$$V_L = \frac{M_3}{M_1} \sin(\frac{\delta}{2}) \cdot V_{in} \tag{2.12}$$

It can be seen that the output voltage V_L is irrelevant to the load, which is only related to M_1, M_3, and the inverter input voltage value V_{in}. Hence, the entire system ensures a load-independent voltage output, which is essential to charge electrical devices. The sensitivity of the distance is high in the presented system. Mutual inductance M3 will be changed if the distance is changed. Therefore, the output will be changed according to (2.12).

2.4 Experimental Validation

2.4.1 Experimental Prototype

As shown in Fig. 2-12, a laboratory prototype of the three-coil WPT system with the proposed magnetic coupler structure is built. The parameters of this system are listed in TABLE 2-2.
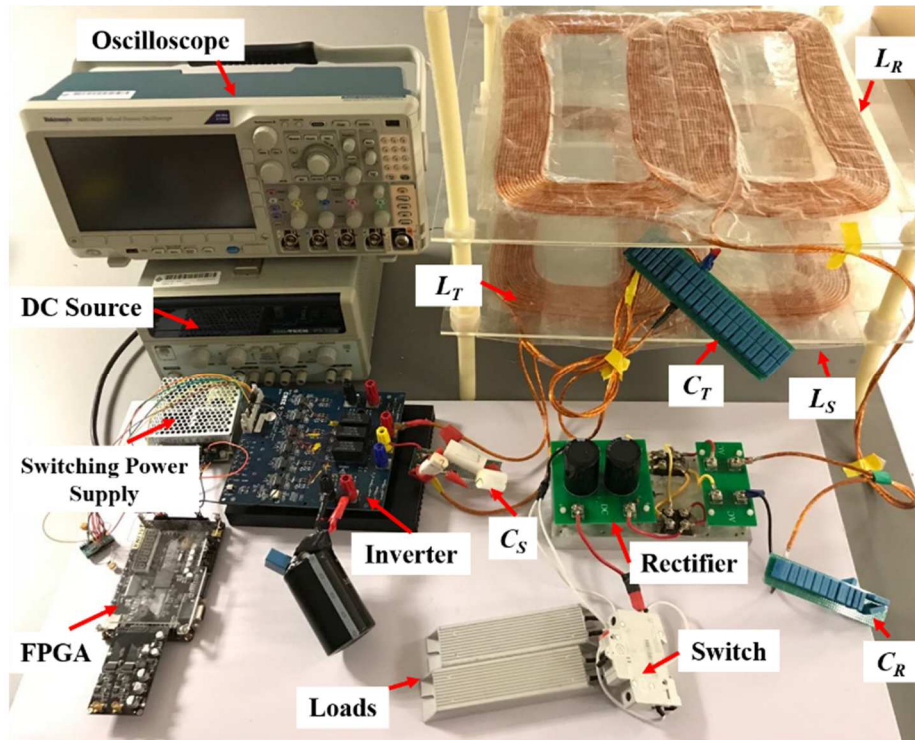
Fig. 2-12. Experimental prototype.

TABLE 2-2. SYSTEM PARAMETERS

Symbol	Value	Symbol	Value	Symbol	Value
C_S	92.0 nF	C_T	15.6 nF	C_R	18.7 nF
L_S	37.7 μH	L_T	223.6 μH	L_R	187.4 μH
R_S	0.20 Ω	R_T	0.65 Ω	R_R	0.48 Ω
M_1	32.2 μH	M_2	0.03 μH	M_3	16.7 μH
f	85 kHz	N_Q	6 turns	N_{DD}	14 turns

2.4.2 Zero Voltage Switching

The output voltage is designed as fixed at 80 V for validation of the proposed WPT experimental prototype. This design can be generalizable to other voltage levels. The output voltage can be adjusted according to different EV charging requirements.

A resistive load R_L is connected to the output of the rectifier, and its resistance changes from 20 Ω to 100 Ω. And the output power is able to vary between 64 W and 320 W. The maximum output power of 320 W is achieved when R_L is 20 Ω. The minimum output power of 64 W happens when R_L is 100 Ω. Key waveforms of the inverter, including output voltage u_1 and output current i_1 are shown in Fig. 2-13. This system can achieve zero voltage switching (ZVS) because i_1 slightly lags behind u_1.
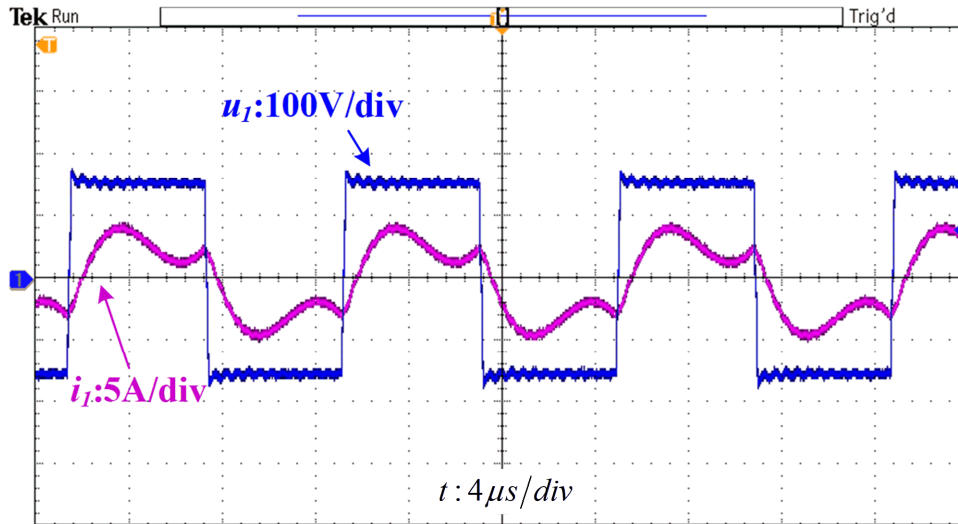
Fig. 2-13. Key waveforms of the inverter.

2.4.3 Load-independent Constant Voltage Output

As shown in Fig. 2-14, the percentage of change of the load RL is 100% (from 40 Ω to 20 Ω), and the measured output current IL changes from 1.91 A to 3.82 A. Nevertheless, the change of measured output voltage is 1.6 V (from 80 V to 78.4 V) merely. Therefore, this experimental result verifies the load-independent output characteristic of the presented system.
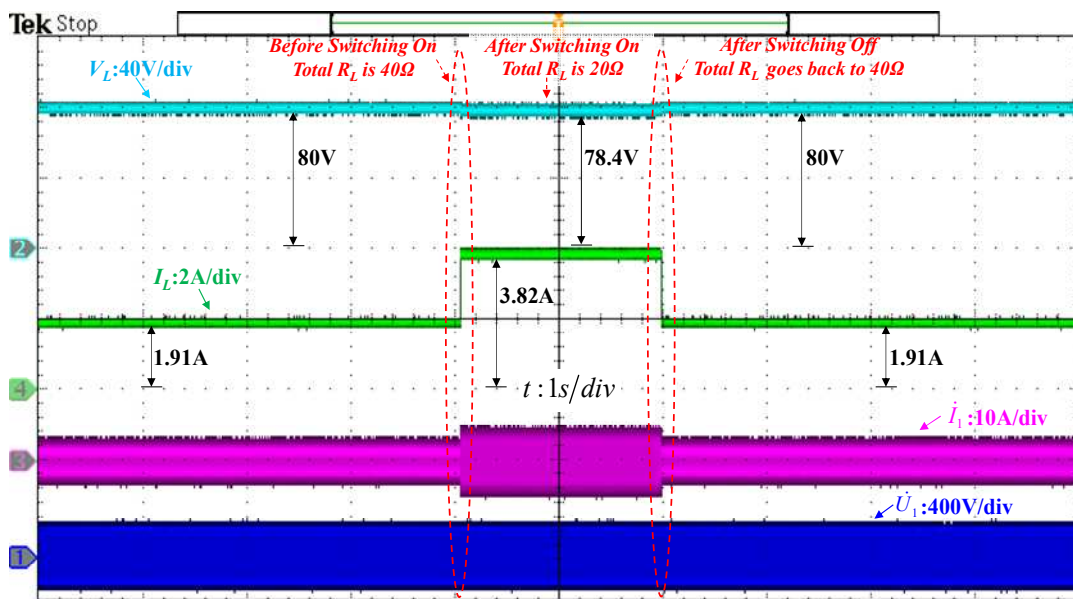
Fig. 2-14. Constant voltage output verification.

2.4.4 Efficiency Analysis

Reference [78] shows a specified condition to ensure the efficiency of the three-coil system can be higher than its two-coil counterpart. This condition is rewritten as in (2.13) this chapter, and a detailed derivation can be found in [78].

$$M_1{}^2 R_R > M_3{}^2 R_T \tag{2.13}$$

where M_1 is the mutual inductance between the source coil and the transmitter coil, M_3 is the mutual inductance between the transmitter coil and receiver coil. R_T is the Equivalent Series Resistance (ESR) of the transmitter coil and R_R is the ESR of the receiver coil. In this chapter, high-quality LITZ wire is adopted so that the ESRs of coils are very small.

In order to obtain a strong magnetic coupling between the source coil and the transmitter coil for satisfying (2.13), the size of the Q coil is selected to be the same as the DD coil to provide a large M_1 since the coupling coefficient is mainly determined by the size of the magnetic coupler [35]. Therefore, M_1, M_3 R_R and R_T are all satisfied (2.13). That means the efficiency of this proposed three-coil system is higher than its two-coil counterpart theoretically.

2.4.5 Efficiency Comparison Without Misalignment

In this chapter, the efficiency comparison is between the proposed structure and its two-coil counterpart. As illustrated in Fig 2.15, the efficiency is the overall dc-dc power transfer efficiency that is defined as (2.14). The efficiency is different between the presented structure and its two-coil counterpart due to different input powers. The input power P_{in} can be directly measured through the DC power supply EA-PSI 9500-30 and the output power P_{out} can be shown by (2-15).

$$\eta = \frac{P_{out}}{P_{in}} \tag{2.14}$$

where P_{out} is the DC output power and P_{in} is the input power from the DC source.

$$P_{out} = V_L \cdot I_L \tag{2.15}$$

where I_L is the current on the load.

Because the efficiency is associated with the load conditions or power level, it is essential to compare the presented three-coil structure and its two-coil counterpart under the same output power level. Therefore, the voltage 80V is kept unchanged by altering the conduction angle to generate constant powers on a specific load for both the proposed three-coil structure and its two-coil counterpart. 80V is one example of experimental validation. This design can be generalizable to other voltage levels. It can be adjusted according to different EV charging requirements. Fig. 2-15 illustrates the efficiency of the proposed three-coil system is persistently higher than its corresponding two-coil counterpart from 64 W to 320W, which complies with the theory in [49]. According to [78], the efficiency of a three-coil WPT system should be higher than its two-coil counterpart thanks to the additional coil.
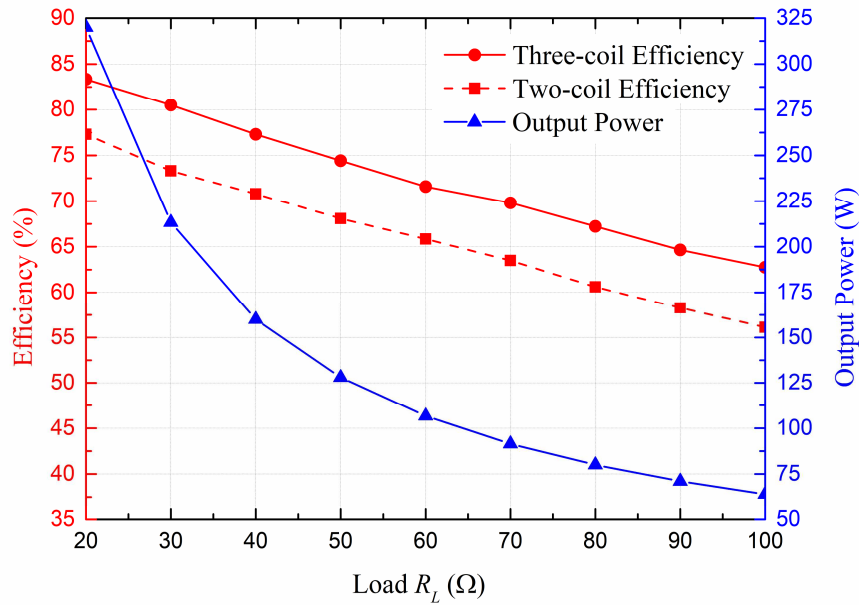
Fig. 2-15. The measured values of overall dc-dc efficiency and the output power from 20 Ω to 100 Ω load conditions.

2.4.6 Efficiency Comparison Under Misalignment Conditions

The misalignment direction is along with the x-axis shown in Fig. 2-16. The

maximum misalignment is 10 cm, which is equivalent to 25 percent of the coil length. TABLE 2-3 shows that M_1 is constant and larger than M_3 no matter whether it is under x-misalignment or not. Under the x-misalignment conditions, the position of the receiver is changed, whereas the positions of the source coil and the transmitter coil are fixed. Thus, M_1 becomes unchanged but M_3 is decreasing. Then, ESRs are not changed because they are the inherent parameters of coils. As depicted in Fig. 2-1, one application of the proposed structure is the mobility scooter. It is convenient to move the scooter in the y-direction while it is difficult to shift in the x-direction [77]. Accordingly, this chapter only focuses on solving the issue of x-misalignment. M_c is the mutual inductance of the two-coil counterpart. The change of the M_c is the same as M_3. The only difference between the presented three-coil WPT system and its two-coil counterpart is the existence of the source coil.

Hence, if the relationship of mutual inductances satisfies (2.13) under the well-aligned condition already, then the equation (2.13) will be continuously satisfied under x-misalignment conditions based on the proposed structure. That means the efficiency of the three-coil structure should be higher than its two-coil counterpart in this situation.
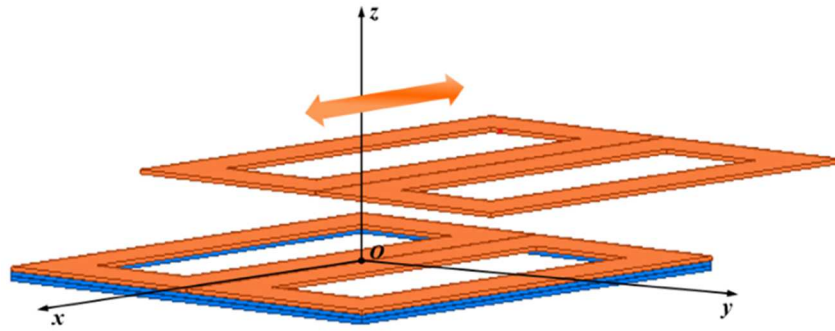
Fig. 2-16. Proposed structure with x-misalignments.

TABLE 2-3. MUTUAL INDUCTANCE VS. X-MISALIGNMENT

X-Misalignment (cm)	M_1 (μH)	M_3 (μH)	M_c
0	32.2	16.7	16.7
2.5	32.2	16.5	16.5
5.0	32.2	15.7	15.7
7.5	32.2	15.0	15.0
10.0	32.2	14.5	14.5

2.4.7 System Control under Misalignment Conditions

In order to make efficiency comparison feasible, the output power P_{out} should be kept constant. In other words, it is actually to keep the output voltage V_L constant for each specific load. However, under different misalignment conditions, M_1 stays stable while M_3 is changing, which leads to the output voltage V_L changes according to (2.12) . Therefore, it is necessary to adopt system control to keep V_L constant. As shown in Fig. 2-17, phase-shifted modulation is used to control the output voltage of the inverter u_1 for further regulating V_L. And the deadtime is set to 200 ns.
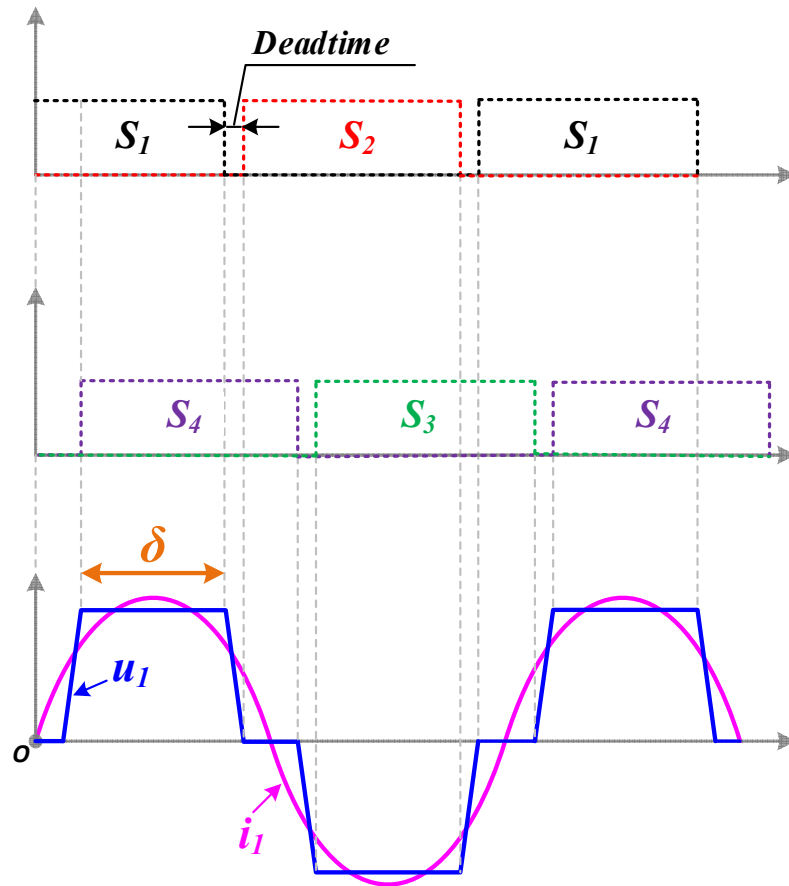
Fig. 2-17. Driving signals (S_1, S_2, S_3, and S_4), conduction angle δ, output voltage u_1, and output current i1 of the inverter under phase-shifted modulation.

From Fig. 2-18 (a)-(d), it is obvious that δ is changed under different misalignment conditions. R_L is fixed as 20 Ω. The maximum misalignment is 10cm, which is 25 percent of coil length. By adjusting δ, V_L can be maintained at 80 V, which means the

output power P_{out} can be fixed at 320 W.

The experimental result of efficiency comparison under different x-misalignments is shown in Fig. 2-19, which illustrates that the efficiency of the three-coil system is always higher than its corresponding two-coil part from 0 to 10 cm. Besides, the drop in three-coil efficiency is from 83.3% to 78.4%, while the two-coil counterpart is from 77.3% to 71.7%. It shows that the efficiency change of the three-coil structure is 4.9% while the two-coil counterpart is 5.6%, which indicates that the efficiency stiffness against x-misalignments of the three-coil structure is slightly better than its two-coil counterpart.
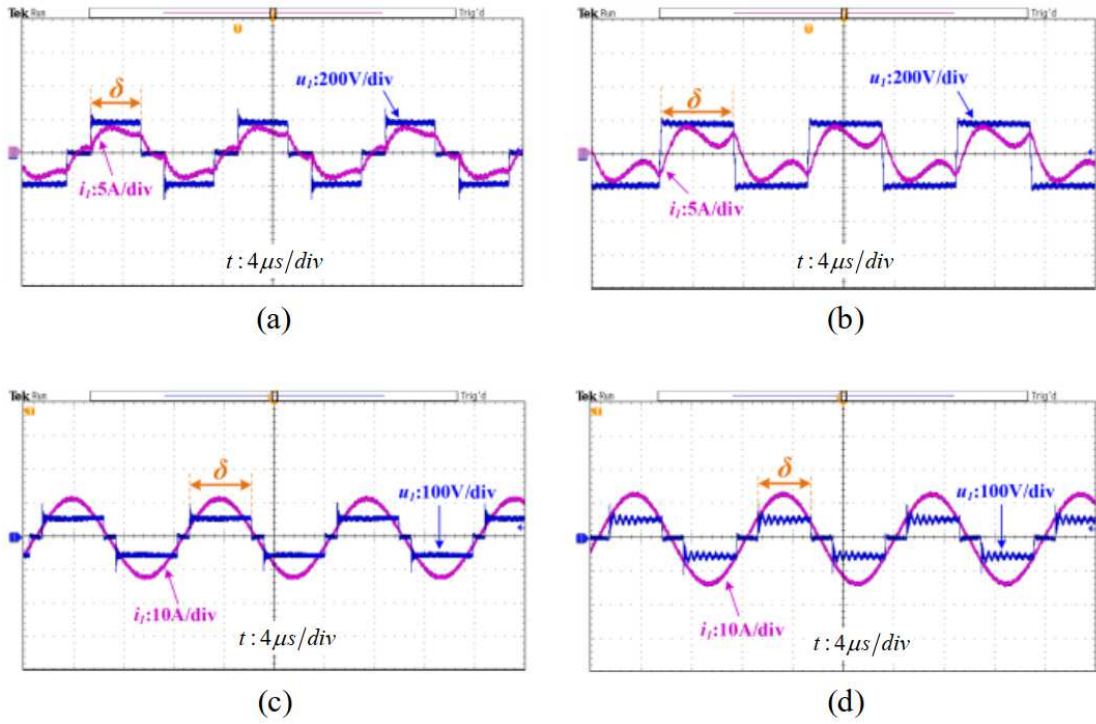
Fig. 2-18. Conduction angle δ adjustment under different conditions:

(a) Three-Coil 5cm misalignment. (b) Three-Coil 10cm misalignment.

(c) Two-Coil 5cm misalignment. (d) Two-Coil 10cm misalignment.
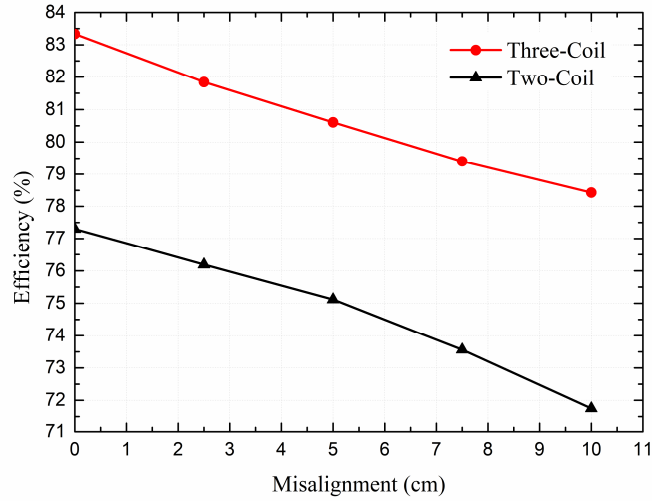
Fig. 2-19. DC-DC efficiency versus x-misalignment.

2.5 Benchmarking

Compared with [79]-[88] and [89]-[104], the proposed structure achieves a zero mutual inductance M_2. Both [79]-[88] and [89]-[104] all assume this mutual inductance as zero or negligible. As illustrated in TABLE 2-4, Q coils and DD coils are already designed large enough to validate zero mutual inductance between them. The measured value of M_2 is extremely small (0.03 µH), which can be regarded as zero due to inevitable error from experiments.

TABLE 2-4. PARAMETER COMPARISON

Parameter \ Paper	This thesis	[78]	[88]	[89]	[91]	[82]
M_2(µH)	0.03	0.094	0.28	neglect	0.24	25.11
L_S (µH)	37.7	1.53	3.68	4.59	3.85	128.58
L_T (µH)	223.6	16.2	165.39	32.77	163.21	69.15
L_R (µH)	187.4	16.2	38.29	29.86	37.12	128.76
Source Size (cm)	40×40	d=3.6	d=20	d=3.5	d=20	43×43
T_X Size (cm)	40×40	d=7.6	d=40	d=7	d=40	32×32
R_X Size (cm)	40×40	d=7.6	d=40	d=7	d=40	43×43
D (cm)	14	6.2	20	5	20	15
f (Hz)	85k	684k	200k	200k	200k	85k

TABLE 2-5 shows the comparison among different load-independent CV systems. The presented three-coil structure can naturally realize the load-independent CV output,

thereby eliminating the dc-dc converters. Compared with [105], high-order compensation networks such as LCC topologies at the receiver side can be saved. To achieve load-independent CV, another approach is to employ a dc-dc converter. Usually, complicated control methods such as primary side control [59], power flow control [60], dual side control [61], or H_∞ control [62] are adopted to regulate the output voltage for realizing good robustness against varying loads. Compared with refs [59-62], the present structure can avoid complex control methods because the load-independent output is realized by the magnetic coupler. Hence, the proposed design not only reduces the weight at the receiver side but also achieves a simple design for load-independent CV output without a complicated control method.

TABLE 2-5. LOAD-INDEPENDENT CV SYSTEM COMPARISON

Paper \\ Requirement	This thesis	[59]	[60]	[61]	[62]	[105]
DC-DC Converter	no	yes	yes	yes	yes	no
Additional LCL/LCC	no	no	no	no	no	yes
CV Control	no	yes	yes	yes	yes	no

2.6 Summary

In this chapter, a special magnetic coupler structure is proposed here to enhance the design freedom of three-coil WPT for electric scooters. Mutual inductance between the source coil and the receiver coil is eliminated, which breaks the design limitation. Conventional practices dramatically restrain the design freedom because the size of the source coil has to be small, and the distance between them has to be large. Using the proposed structure, the size and distance are not the design constraints anymore. Furthermore, the presented structure allows the expression of intrinsic characteristics such as load-independent constant voltage output and efficiency enhancement. In particular, load-independent CV output characteristics are examined and validated. Efficiencies under aligned and misaligned conditions are compared. Experimental verification of the WPT system was conducted using an H-bridge power converter. The

H-bridge power converter is a typical power electronic circuit for a WPT system. An experimental prototype was built to test the feasibility of the proposed approach, and the load-independent output characteristics are consistent with theoretical analysis. The proposed WPT system can achieve a measured overall dc-dc power transfer efficiency at 83.3% with a 14 cm air gap when delivering to a load with a power level between 320 W and 20W. The design can be generalized to other output voltages or power levels as required to meet different charging demands. The next chapter will describe the improvement technique such that a design is proposed for a decoupled-double receiver WPT system for AGVs.

Chapter 3

Double-receiver Magnetic Coupler in Wireless Power Transfer for AGVs

The use of automated guided vehicles (AGVs) has been identified as a promising method of releasing labor from repetitive work and facilitating the development of unmanned factories. With the demands of future manufacturing and intelligent transportation from industry 4.0, AGVs are gradually taking on a role as commercially valuable robotics and daily transportation. Unplanned downtimes in the industry are frequently caused by human error. Employees can make mistakes when distracted or exhausted. The AGV forklift, as an unmanned robotics system, can reduce the risk of ergonomic strains and injuries caused by improper manual handling. As an environmentally friendly vehicle, AGVs could be an excellent alternative to conventional petrol vehicles and help save fossil fuels [106]. Therefore, AGVs may be able to provide a safe work environment, an intelligent transport system, and an element of smartness in the future of warehouses. By using innovative navigation sensors, superior computing capabilities, and advanced controllers, the market for automated guided vehicles is expected to be dynamic and versatile within the next few years. This is a system that is perfectly suitable for the promising industrial revolutions such as Industry 4.0 and the Internet of Things (IoT).

Due to a large number of electronic devices enrolled, innovative and multiple charging methods have become a necessity for AGVs. Nevertheless, conductive charging seems like an unadvisable choice [107]. Conductor-based charging would compromise vehicles' working freedom because they would have to search for nearby charging stations at the cost of an additional trip [108]. In addition, the frequent plugging in and out of the equipment would result in relatively high maintenance costs [109]. In addition, the onboard charger, an essential component of such a conductive charging system, includes auxiliary equipment such as a connector, an EMI filter, a

rectifier, a dc-dc converter, and controllers [110]. A bulky onboard charger occupies considerable space and increases the weight of the vehicle [111].

As a promising charging method, inductive power transfer systems (IPT) are ideal for AGVs [112]. The transmitter is embedded on the ground, and the receiver is mounted on the chassis of the AGV. This allows for easy charging. In addition, the onboard battery pack is reduced as well as the effective working time is increased. IPT contributes to the development of AGVs by supplying an unmanned charging system, reducing the weight on the AGV, and resulting in a compact, even, in-process charging system. [113]. In this regard, AGVs are well-suited to IPT due to their low chassis height, as IPT is more effective at short or medium-range wireless charging. Over the next few decades, the field of self-driving technology is likely to result in the popularization of AGVs with high positioning accuracy, and lateral misalignment will no longer present a problem for IPTs. In this digital age, these two technologies result in a win-win situation.

As an intelligent collection of power electronics, AGVs contain many devices, as shown in Fig. 3-1. And each one has its own charging requirement, such as constant current (CC) for multi-string LEDs [89], constant voltage (CV) for gate drivers [114], CC and CV for Lithium-ion batteries [115], giving rise to the difficulty in wireless charging. As charging objectives (LEDs, gate drivers, batteries, etc.) increase, it is urgent to an emerging charger with double/multiple outputs for AGVs [116].
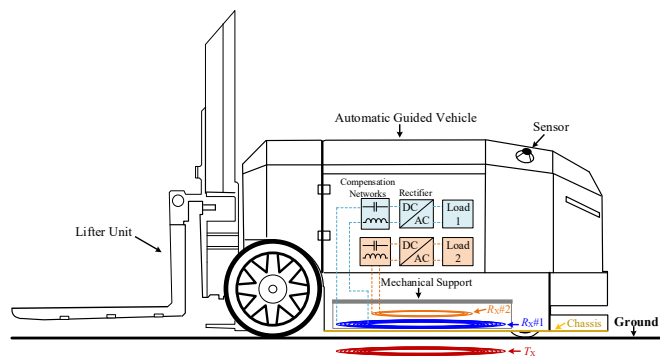
Fig. 3-1. The diagram of a typical AGV forklift with the double receiver WPT system.

3.1 Review of the decoupling methods

Wireless power transfer (WPT) has been successfully applied in numerous areas, e.g., heating systems [5], consumer electronics [117], [89], and electrical vehicles (EVs) [24]-[115], thanks to the intrinsic superiorities such as safety, convenience, and user-friendliness [118], [119]. These advantages can be further enlarged by the two-receiver system [120]. A two-receiver system consists of two receivers that can work together to offer double charging channels. But unwanted cross-couplings hinder its development by interfering with outputs [121], causing a bifurcation phenomenon [122], or shifting the maximum efficiency operation [123]. The first unwanted cross-coupling type is between receivers. Several methods have been proposed to eliminate or mitigate this unwanted coupling, which can be roughly divided into four types:

1) Physical type: The magnetic couplings among receivers can be negligible when displacing the receivers far from each other, and the size of receivers should be small enough [124], [125]. Nevertheless, this method significantly limits the design freedom; for instance, receiver sizes have to be small, and the distance between two receivers has to be large to minimize this unwanted coupling. Most importantly, this unwanted coupling is not eliminated completely in theory [124] and [125]. Even though the undesirable cross-couplings are small enough, these unwanted cross-couplings still exist. In other words, the cross-coupling is assumed as null rather than eliminating theoretically.

2) Magnetic shielding type: References [126]-[129] utilizes ferrite plates with repeater coils to transfer energy one by one. However, the following receivers highly depend on the former ones. If one receiver breaks down, all following receivers cannot work. Consequently, all receivers are supposed to work simultaneously. Each receiver cannot work independently. Moreover, bulky components such as ferrite plate, LCL, or CLC compensation topologies are widely used in this type, which increases the cost and weight of each receiver. Moreover,

misalignment tolerance is not considered in these references.

3) Circuit-based type: One is to utilize additional decoupling reactance, including fixed [116] and variable [130], [131] types. Nevertheless, the first drawback of [116] is the physical limitation because two receives are still connected by a fixed reactance physically. This greatly limits movable freedom, which also requires extra space and cost. If the reactance is an additional inductor, the cross-coupling from this additional inductor still needs consideration. The second drawback of [116] is the electrical limitation. The fixed cross-coupling elimination reactance makes two receivers cannot work independently. If one receiver is open circuit, the resonant state and output of the other one will be greatly changed. If the mutual inductance changes between two receivers, this fixed additional decoupling reactance will become invalid. As a consequence, the mutual inductance has to be unchanged between these two receivers. In order to meet more practical needs, adjustable reactance is adopted [130], [131]. However, the variable reactance strongly depends on coil positions. It is quite challenging to adjust the variable reactance to an appropriate value for each receiver. The situation tends to become more complex when estimating the relative positions of coils and the output power of other receivers. To avoid the reactance adjustment, some researchers adopted additional circuits to dynamically change the resonant frequency [132], [133], or phase angles [134]. On the one hand, changing the resonant frequency posts critical problems. If one receiver's resonant frequency is close to that of other receivers, the power can be generated unintentionally among them. In other words, the unwanted cross-couplings are still not resolved at the root. Furthermore, it is not easy to use frequency control to maintain constant outputs. A stability issue may be generated with varying loads, e.g., frequency bifurcation, and the inverter of the WPT system is unlikely to achieve zero phase angle (ZPA) [88]. Nowadays, WPT systems tend to focus on ZPA to improve efficiency compared to ZVS [88]. On the other hand, the unwanted cross-coupling can be compensated fully when the phase of the current in each receiver is orthogonal to the phase of the transmitter current [134].

Nevertheless, each receiver needs an extra control part, which dramatically increases weight and complexity. Practical communication issues between the inverter side and the load side must be considered in such a system as well.

4)   Coil-based type: In [135], a two-receiver WPT system was built with the bucking planer coil (BPC), as illustrated in Fig. 3-2. The decoupling can be realized by the flux cancelation by alternating the BPC winding direction. Compared to the coils wound in one direction, the BPC requires more cables to realize the same equivalent mutual inductance between transmitter and receivers. Most importantly, bucking coils needs specific turns and coil design, which is time-consuming for engineers and dramatically limits the design freedom. The extra cables also increase the weight and cost and require more installation space on the receiver side. Load-independent outputs and ZPA are not discussed in [135] either.
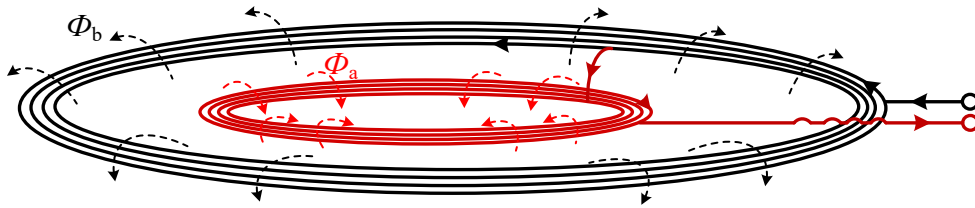
Fig. 3-2. A typical structure of a BPC coil.

In addition, load-independent CV outputs are taken into consideration and can be realized with the help of a relay coil [88]. Nevertheless, the prerequisite is that the cross-coupling between the source and the receiver should be small enough. Therefore, the second unwanted cross-coupling type is among receivers and the source coil. In this work, the Q-shaped coil is used as the source coil, while DD coils are used as receivers to realize null cross-couplings among them. And the energy can still be transferred to loads, thanks to the relay coil that contains two orthometric DD coils and one Q-shaped coil. Furthermore, investigations show that the efficiency [78] and electromagnetic compatibility (EMC) [95] can be enhanced due to a relay coil.

Overall, an interesting double-receiver WPT system is proposed to resolve the aforementioned problems. The contributions of this chapter are listed as follows:

1)   In theory, there is no unwanted coupling between receivers. Therefore, associated problems generated by this cross-coupling can be avoided, and a robust system can be realized. Especially, one receiver cannot affect the other's work, achieving low sensitivity to the influence from each other, i.e., misalignment happens, air gap changes and an open circuit occurs. Notably, these conditions are all discussed in this chapter. In practice, the proposed method emancipates engineers to design magnetic couplers based on various design purposes. Without complicated control, communication system, and additional variable reactance, a simple and compact double-receiver WPT system can be achieved.

2)   There are no unwanted couplings among the receiver coils and the source coil. Thus, this system can achieve load-independent constant voltage outputs. Compared with other CV outputs methods like employing accessional compensation networks such as LCC [50] or CLC [136] topologies, the proposed method dramatically saves on-board space and cost on the receiver side. Compared with utilizing dc-dc converters to regulate CV, the proposed system avoids complex strategies such as primary side control [59], power flow control [60], dual side control [61], or H_∞ control [62]. Thus, the proposed design reduces the weight at the receiver side and achieves a simple design for load-independent CV output without complicated control methods or bulky compensation networks.

3)   With the well-designed compensation parameters, the inverter can achieve ZPA. It can lower the volt-ampere rating and increase efficiency. In other words, the inverter only provides active power to the load, which means that it can enhance the power transfer capacity and reduce the power losses.

3.2 Magnetic Coupling Structure

This chapter utilizes two DD coils as two receivers, which are orthometric in position to eliminate the unwanted coupling between them. Bipolar structures such as DD coils are seldomly discussed with respect to double-receiver WPT systems. Remarkably, this chapter utilizes DD coils as receivers and the upper part of the relay part. Hence, the superiority of the DD coil, including low magnetic leakage [95] and high misalignment tolerance [35], can be utilized in the double-receiver WPT system.

The Q-shaped source is adopted as the source coil, which can naturally decouple from two DD receivers. Fig. 3-3 and Fig. 3-4 reveal the physics behind the decoupling mechanism. When the excitation currents are in phase, the structure of the Q-shaped and two DD coils with corresponding magnetic flux is shown in Fig. 3-3. The generated magnetic flux is single-sided for the Q-shaped transmitter coil, and the polarity depends on the phase of its excitation current. The generated magnetic flux is double-sided for the DD transmitter coil due to the symmetrical coil structure [93], [94].
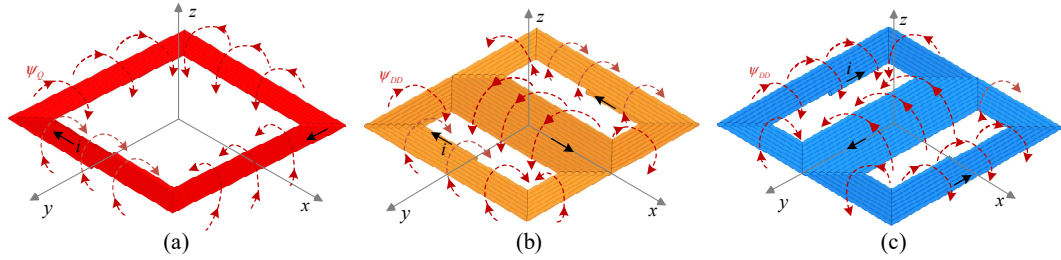
Fig. 3-3. The diagram of structures with magnetic flux. (a) Q-shaped coil, (b) DD coil, and (c) Orthometric DD coil.

The effect of null magnetic couplings can be reflected through induced voltages, as shown in Fig. 3-4. Null-induced voltages can be realized between a Q-shaped coil and a DD coil under overlapped conditions [137].

In the bipolar magnetic field generated by an overlapped DD coil, the induced voltage of a Q-shaped coil is as shown in Fig. 3-4 (a), which can be expressed as

$$\dot{U}_Q = \dot{U}_{qa} - \dot{U}_{qb} = 0 \tag{3.16}$$

In the unipolar magnetic field generated by an overlapped Q-shaped coil, the induced voltage of a DD coil, as shown in Fig. 3-4 (b), can be expressed as

$$\dot{U}_{DD1} = \dot{U}_{da} - \dot{U}_{db} = 0 \qquad (3.17)$$

The induced voltages of two overlapped orthometric DD coils are shown in Fig. 3-4 (c) and (d), which can be expressed as

$$\begin{cases} \dot{U}_{DD2} = \dot{U}_1 - \dot{U}_2 - \dot{U}_3 + \dot{U}_4 = 0 \\ \dot{U}_{DD3} = -\dot{U}_5 + \dot{U}_6 + \dot{U}_7 - \dot{U}_8 = 0 \end{cases} \qquad (3.18)$$
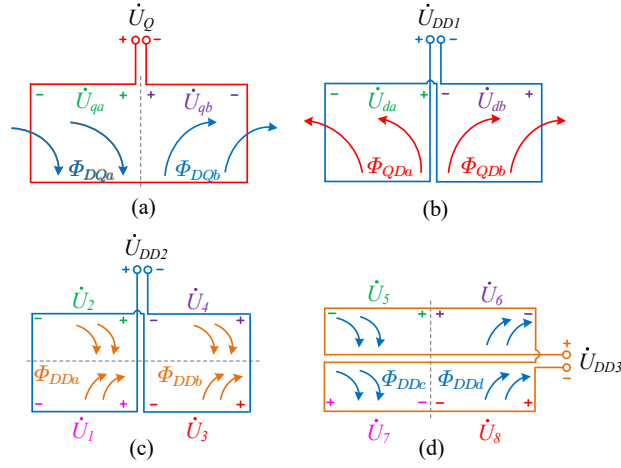
Fig. 3-4. Induced voltages: (a) the Q-shaped coil with the flux Φ_{DQa} and Φ_{DQb} generated by the DD coil, (b) the DD coil with the flux Φ_{QDa} and Φ_{QDb} generated by the Q-shaped coil, (c) the DD coil with the flux Φ_{DDa} and Φ_{DDb} generated by an orthometric DD coil.

Fig. 3-5 illustrates the diagrams of the proposed magnetic coupler with detailed size information. This coupler consists of three parts: source, relay, and receivers. Specifically, the source coil is a purely Q-shaped coil. The relay coil is made up of a Q-shaped coil and two orthometric DD coils. Receiver-A (R_X_A) and receiver-B (R_X_B) are DD coils, which are orthometric in position. Air gaps are D_A and D_B, respectively.
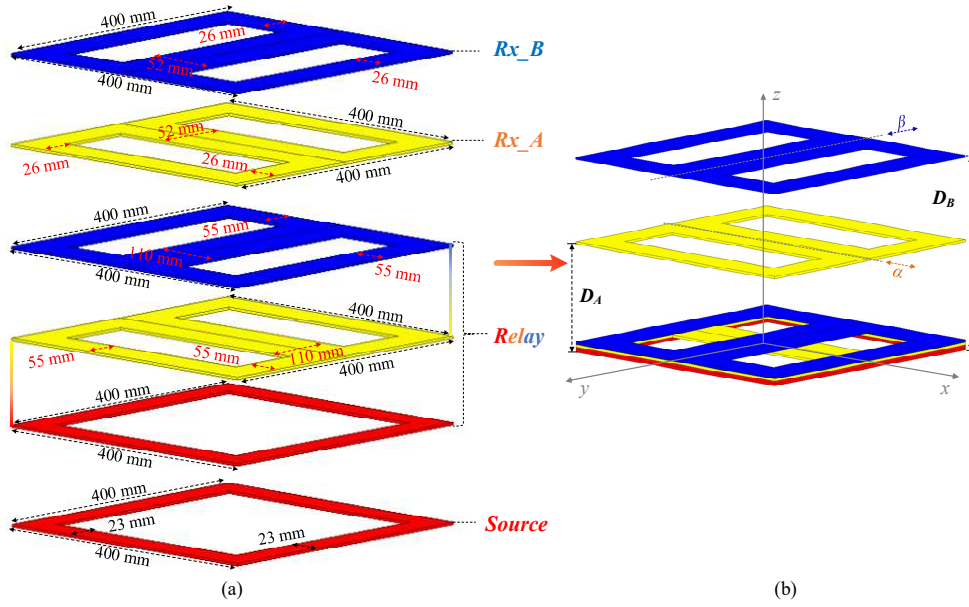
Fig. 3-5. Diagrams of proposed magnetic coupler (a) Exploded view with size information and (b) The full assembly view.

3.3 Theoretical Analysis

3.3.1 Circuit Analysis

The entire circuit diagram of the proposed system is illustrated in Fig. 3-6. The input dc voltage of the H-bridge inverter is V_{in}. Then, the inverter is equipped at the source side to generate ac power for feeding the source coil. The fundamental harmonics approximation (FHA) method is used to analyze the proposed WPT system. The fundamental component of the output voltage of the inverter is expressed as

$$u_1\left(t\right) = \frac{4}{\pi}V_{in}\sin\omega t \tag{3.19}$$

where $\omega = 2\pi f$. Especially, f is the switching frequency. The use of the resonant frequency is fixed at 85 kHz, suggested by SAE J2954 for wireless charging EVs [101]. The sensitivity of resonant frequency should be low since each coil is well-tuned with the corresponding capacitors at 85 kHz.
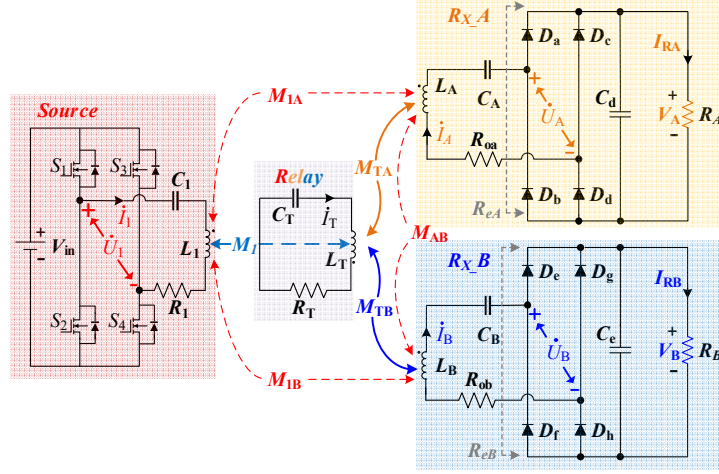
Fig. 3-6. Entire circuit diagram with the proposed double receivers, including three major mutual inductances (M_1, M_{TA}, M_{TB}) and three unwanted mutual inductances (M_{1A}, M_{1B}, M_{AB}).

Accordingly, the fundamental phasor root mean square (RMS) form of $u_1(t)$ can be expressed as

$$\dot{U}_1 = \frac{2\sqrt{2}}{\pi} V_{in} \angle 0° \tag{3.20}$$

L_1, L_T, L_A, and L_B are the self-inductances of the source coil, the relay coil, and the receiver coil A and B, respectively. C_1, C_T, C_A, and C_B are the resonant capacitors that satisfy the following equation:

$$\begin{cases} C_1 = \left(\omega^2 L_1\right)^{-1} & C_T = \left(\omega^2 L_T\right)^{-1} \\ C_A = \left(\omega^2 L_A\right)^{-1} & C_B = \left(\omega^2 L_B\right)^{-1} \end{cases} \tag{3.21}$$

Two full-bridge rectifiers are used to convert the ac power to the dc power to feed loads, i.e., R_A and R_B. The relationships between ac inputs (U_A, U_B, I_{RA}, and I_{RB}) and dc outputs (V_A, V_B, I_A, and I_B) can be described as

$$\begin{cases} \dot{U}_A = 2\sqrt{2}V_A/\pi \\ \dot{I}_{RA} = \sqrt{2}\,\pi I_A/4 \\ R_{eA} = 8R_A\pi^{-2} \end{cases} \qquad \begin{cases} \dot{U}_B = 2\sqrt{2}V_B/\pi \\ \dot{I}_{RB} = \sqrt{2}\,\pi I_B/4 \\ R_{eB} = 8R_B\pi^{-2} \end{cases} \tag{3.22}$$

where R_{eA} and R_{eB} are the equivalent resistances of these two rectifiers, respectively.

TABLE 3-1 clarifies magnetic couplings generated by the proposed double-receiver structure. All magnetic couplings are considered and analyzed, reflected by four self-inductances (L_1, L_T, L_A, and L_B) and six mutual inductances (M_{1A}, M_{1B}, M_{AB}, M_1, M_{TA}, and M_{TB}). Thanks to the decoupling mechanism, the unwanted couplings (M_{1A}, M_{1B}, and M_{AB}) can be eliminated. As a result, only three major mutual inductances need considering, i.e., M_1, M_{TA}, and M_{TB}.

TABLE 3-1. MAGNETIC COUPLING CLARIFICATION

	Source	*Relay*	R_{X-A}	R_{X-B}
Source	L_1	M_1	M_{1A}	M_{1B}
Relay	M_1	L_T	M_{TA}	M_{TB}
R_{X-A}	M_{1A}	M_{TA}	L_A	M_{AB}
R_{X-B}	M_{1B}	M_{TB}	M_{AB}	L_B

3.3.2 Load-independent CV outputs

Constant voltage (CV) output is essential for battery-based applications. For AGVs, the IPT charges the battery of the driven system and the control system, respectively. The former needs a high charging voltage, whereas the latter needs a low voltage [116]. Therefore, it is necessary to investigate CV charging systems.

Notably, a T-resonant circuit can realize the power conversion between voltage sources and current sources and transform the impedance without changing the characteristics [100]. Interestingly, if we fully compensate for the self-inductances, mutual inductances naturally form T-resonant circuits, i.e., T_1, T_A, and T_B, as illustrated in Fig. 3-7 and Fig. 3-8.

It is efficient to adopt decoupling circuits with T and S resonant networks to analyze the output characteristics. Fig. 3-7 demonstrates the equivalent decoupling circuit of the proposed double-receiver WPT system. U_1 is the phasor form of output voltage from the inverter, which can be regarded as a CV. After resonant circuits (S_1, T_1, and S_T), the whole circuit can be equivalent to a constant current (CC) source. And I_T is the phasor form of this CC output.
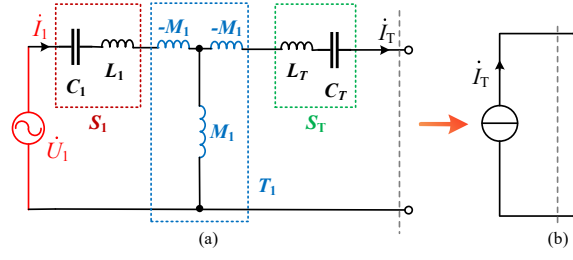
Fig. 3-7. The equivalent circuits: (a) The decoupling circuit with S_1, T_1, and S_T resonant circuits and (b) The equivalent circuits seen from the relay coil.

Then, this CC source can be further used to analyze the decoupling circuits of two receivers, as illustrated in Fig. 3-8. It contains two S resonant networks (S_{RA} and S_{RB}) and two T resonant networks (T_A and T_B). Similarly, T_A and T_B transfer this constant current I_T into double CV outputs. Thus, two load-independent CV outputs (U_A and U_B) can be gained. Especially, Z_A and Z_B are the equivalent input impedance of receiver-A and -B, respectively.
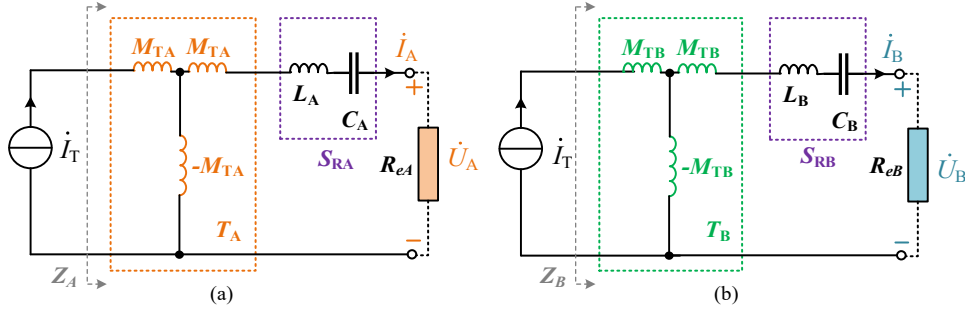
Fig. 3-8. The equivalent decoupling circuits: (a) Receiver-A and (b) Receiver-B.

Next, qualitative analysis with mathematical derivation can be seen as follows; concerning all S resonant networks mentioned above, the following equations can be established:

$$\begin{cases} Z_{S_1} = j\omega L_1 + 1/j\omega C_1 = 0, & Z_{S_T} = j\omega L_T + 1/j\omega C_T = 0 \\ Z_{S_{RA}} = j\omega L_A + 1/j\omega C_A = 0, & Z_{S_{RB}} = j\omega L_B + 1/j\omega C_B = 0 \end{cases} \tag{3.23}$$

where Z_{S1}, Z_{ST}, Z_{SRA}, and Z_{SRB} are the impedance of resonant networks S_1, S_T, S_{RA}, S_{RB}, respectively.

Similarly, concerning T_1, T_A, and T_B resonant networks, the following equations

can be established:

$$\begin{cases} \dot{U}_1 = -j\omega M_1 \dot{I}_{\mathrm{T}} \\ \dot{U}_{\mathrm{A}} = -j\omega M_{\mathrm{TA}} \dot{I}_{\mathrm{T}} \\ \dot{U}_{\mathrm{B}} = -j\omega M_{\mathrm{TB}} \dot{I}_{\mathrm{T}} \end{cases} \tag{3.24}$$

When the input dc voltage is constant, the output voltage of the inverter U_1 is constant. In this case, two constant output voltages can be realized, which can be expressed as

$$\dot{U}_{\mathrm{A}}/\dot{U}_1 = M_{\mathrm{TA}}/M_1 \quad , \quad \dot{U}_{\mathrm{B}}/\dot{U}_1 = M_{\mathrm{TB}}/M_1 \tag{3.25}$$

The output voltage of each equivalent load is irrelevant to the load, which is only related to M_1, M_{TA}, M_{TB}, and the inverter output voltage value U_1. Substituting (7) and (9) into (12), two load-independent CV outputs (V_{A} and V_{B}) can be gained on the two loads. Finally, V_{A} and V_{B} can be expressed as

$$V_{\mathrm{A}} = \left(M_{\mathrm{TA}}/M_1\right) \cdot V_{\mathrm{in}} \quad , \quad V_{\mathrm{B}} = \left(M_{\mathrm{TB}}/M_1\right) \cdot V_{\mathrm{in}} \tag{3.26}$$

3.3.3 Impedance Analysis

Fig. 3-9 shows the equivalent decoupling circuit of the overall system. The impedance relationship is depicted as (3.27). It can be seen that the input impedance seen from the inverter Z_{in} is purely resistive, which indicates that this WPT structure can achieve ZPA with fixed operating frequency by using resonant compensations. In other words, the inverter only provides active power to the load, which means that it can enhance the power transfer capacity and reduce the power losses.
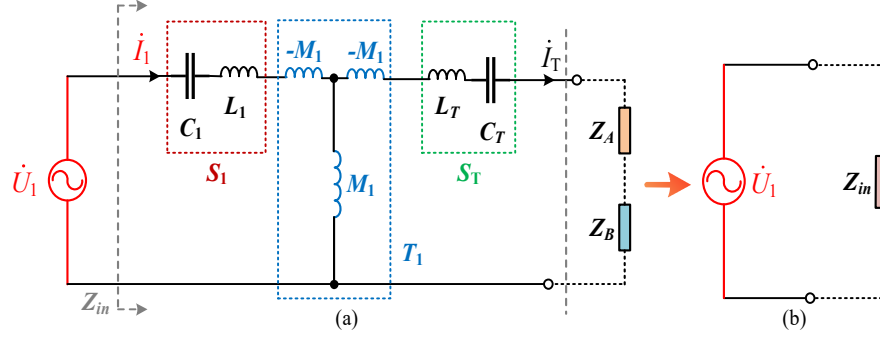
Fig. 3-9. The equivalent decoupling circuits: (a) The overall system with the equivalent input impedances Z_A and Z_B, (b) The equivalent circuit seen from the inverter, including the constant voltage source U_1 and the input impedance Z_{in}.

The corresponding impedance Z_A, Z_B and Z_{in} can be expressed as

$$\begin{cases} Z_A = -\omega^2 M_{TA}^2 \left(R_{eA} \right)^{-1} \\ Z_B = -\omega^2 M_{TB}^2 \left(R_{eB} \right)^{-1} \\ Z_{in} = \left(M_1^2 R_{eA} R_{eB} \right) / \left(M_{TA}^2 R_{eB} + M_{TB}^2 R_{eA} \right) \end{cases} \tag{3.27}$$

3.4 Experimental Verification

Details of the experimental prototype and implementation procedures are summarized in this section. TABLE 3-2 describes the detailed experimental prototype parameters. Inductance, resistance, and capacitance are all measured by RS-Pro LCR 6300 at 85 kHz (the operating frequency). The high-quality 600-strand LITZ wire is utilized to minimize the AC resistances and to reduce the skin effect losses.

TABLE 3-2. SPECIFICATIONS OF THE EXPERIMENTAL SETUP

Symbol	Value	Symbol	Value	Symbol	Value
C_1	96.98 nF	L_1	37.12 μH	R_1	0.141 Ω
C_T	8.44 nF	L_T	417.61 μH	R_T	0.936 Ω
C_A	49.62 nF	L_A	71.47 μH	R_{oa}	0.110 Ω
C_B	48.77 nF	L_B	72.15 μH	R_{ob}	0.125 Ω
$N_{Q\text{-Source}}$	6 turns	$N_{Q\text{-Relay}}$	6 turns	$N_{DD\text{-Relay}}$	14 turns
$N_{DD\text{-Rx\_A}}$	7 turns	$N_{DD\text{-Rx\_B}}$	7 turns	f	85 kHz

3.4.1 Experimental Setup

As demonstrated in Fig. 3-10, a laboratory prototype of the double-receiver WPT system has been built to verify the theoretical analysis. Current probes (Tektronix TCP0030A) and voltage differential probes (TA057) are adopted to gain the experimental data. MOSFETs (CCS020M12CM2) and diodes (DSEI 2x61-06C) are used in the proposed WPT system to meet the requirement of the industrial power supplies. Specifically, CCS020M12CM2 is the 20-A All-Silicon Carbide module that is very suitable for the high-frequency inverter. DSEI 2x61-06C is used to build the rectifier, as shown in TABLE 3-3.

TABLE 3-3. SPECIFICATIONS OF THE DIODES

DSEI 2x61-06C	$V_f=V_{fR}$	1.8 V
	$r_D=r_{DR}$	4.7 mΩ
	Q_{RR}	1 μC
	I_R	30 A
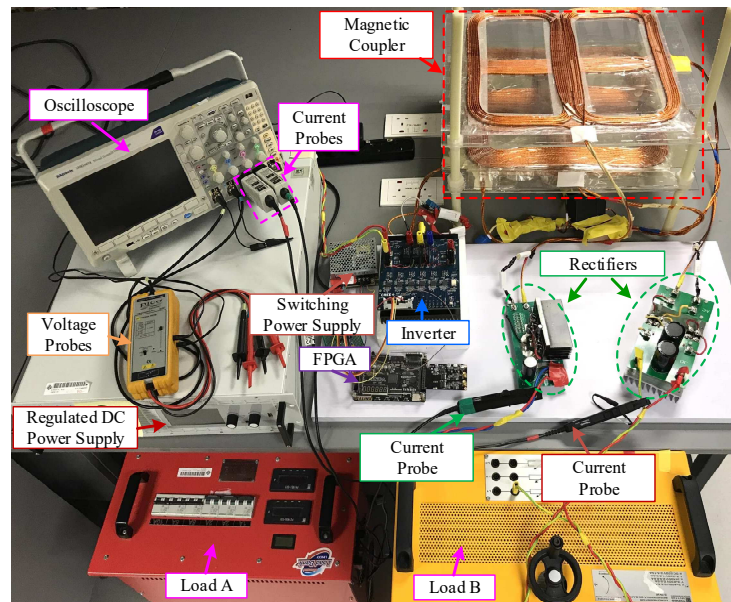
Fig. 3-10. Experimental prototype.

3.4.2 Self-inductance and Mutual Inductance Test

Due to the symmetric structure, this chapter only measures *y*-direction (*β*) misalignments of receiver-B for simplification, as shown in Fig. 3-5. The variations of self-inductances and mutual inductances are shown in Fig. 3-11. RS-Pro LCR-6300 is utilized to measure the inductance in this thesis. The variations of measured self-inductance are within 0.35% of the well-aligned value, which can be negligible. Accordingly, all the self-inductance can be regarded as unchanged in this chapter.

It is necessary to test the mutual inductances since they determine the output characteristics according to (12). *β* is the misalignment in the y-direction according to Fig. 3-5. Then, Fig. 3-12 demonstrates that M_1 and M_{TA} are stable while *β* is increasing. The variations of measured M_1 and M_{TA} are within 0.78% of the well-aligned value, which can be regarded as unchanged. It should be noted that the unwanted cross-couplings can be negligible, which can be reflected by measuring the maximum values of unwanted coupling coefficients among coils, i.e., k_{1A} (0.003), k_{1B} (0.003), and k_{AB} (0.003). Even the maximum values are already small enough to neglect, thereby verifying cross-coupling elimination effects. After successfully eliminating k_{AB} thanks to two DD coils in orthogonal position, the output voltage of receiver-A is independent of receiver-B. Receiver-A can maintain its output characteristic when receiver-B works in different situations.
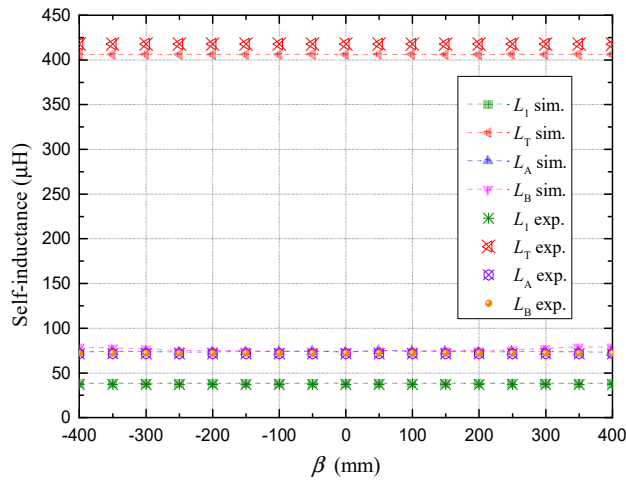
Fig. 3-11. Variation of self-inductance due to the misalignment of R_X_B.
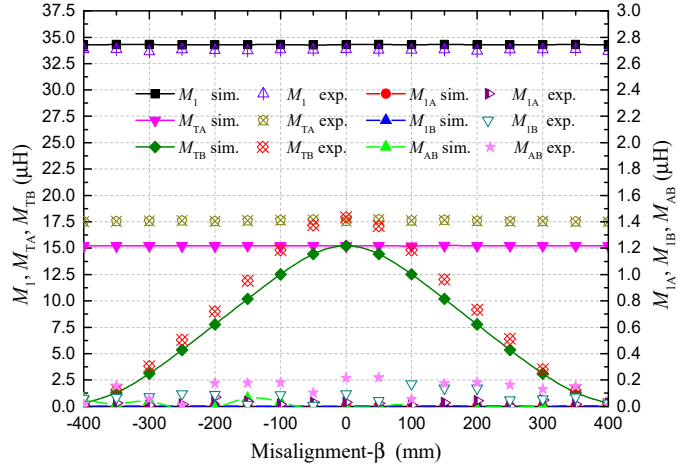
Fig. 3-12. The variation of measured mutual inductances due to the misalignment-β of receiver-B.

3.4.3 Zero Phase Angle Validation

In the proposed WPT experimental prototype, the output voltage is designed as 72 V. Fig. 3-13 illustrates the experimental oscillograms of inverter output voltage u_1, inverter output current i_1, and receiver output voltages V_A and V_B. It is noted that u_1 and i_1 are in phase, which implies that the ZPA operation can be realized, and the resonant inverter only provides active power to the loads. In other words, the voltage/current stress and conduction loss can be reduced dramatically.
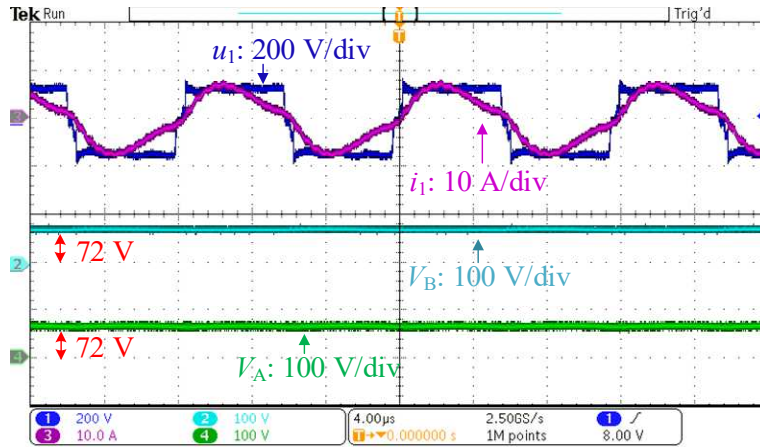
Fig. 3-13. Key oscillograms of the proposed double-receiver system, including u1, i1, VA, and VB

when DA = DB = 120 mm, and RA = RB = 20 Ω.
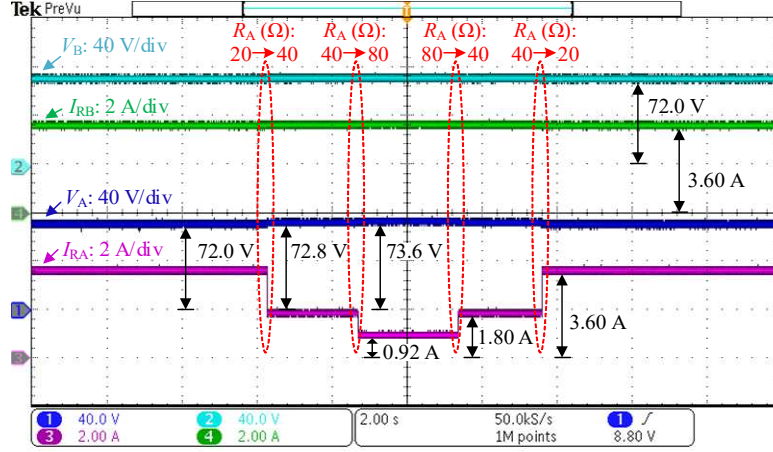
Fig. 3-14. The dynamic response values of the proposed system when R_A is changed from 20 to 40, and 80 Ω then goes back again at the alignment condition of two receivers ($\alpha = \beta = 0$), max air gaps ($D_A = D_B = 120$ mm), and $R_B = 20$ Ω.

3.4.4 Load-independent Constant Voltage Validation

Firstly, the load-independent output voltage is tested under alignment conditions. Fig. 3-14 illustrates the dynamic response of the system when RA changes from 20 Ω to 40 Ω, then to 80 Ω, and back to 20 Ω again. The percentage change of the load resistance RL is 400% and the measured output current IRA changes from 0.92 A to 3.60 A. However, the rate of change of measured VA is only 2.22% (from 72.0 V to 73.6 V), which can be regarded as unchanged. The current IRB and VB are kept as 3.6 A and 72 V, respectively. Hence, this experimental result indicates that the proposed system can achieve the load-independent CV output for two receivers under the aligned condition.

Secondly, Next, the load-independent output voltage is tested under misalignment conditions ($\beta = \pm 100$ mm, ± 200 mm, ± 300 mm, and ± 400 mm), as shown in Fig. 3-15. Due to the symmetrical structure, this thesis only tests the β-misalignment conditions. Fig. 3-15 (a)-(h) illustrate the dynamic response under different β conditions when R_A changes from 20 Ω to 40 Ω then to 80 Ω, then goes back again. The rate of change of the load R_A is 75%. However, the rate of change of measured V_A is 2.22% (from 72.0 V to 73.6 V), which can be regarded as unchanged. I_{RB} and V_B are kept as 3.6 A and 72

V, respectively. Hence, this experimental result indicates that the proposed system can realize the load-independent CV output for two receivers under different β-misalignment conditions.
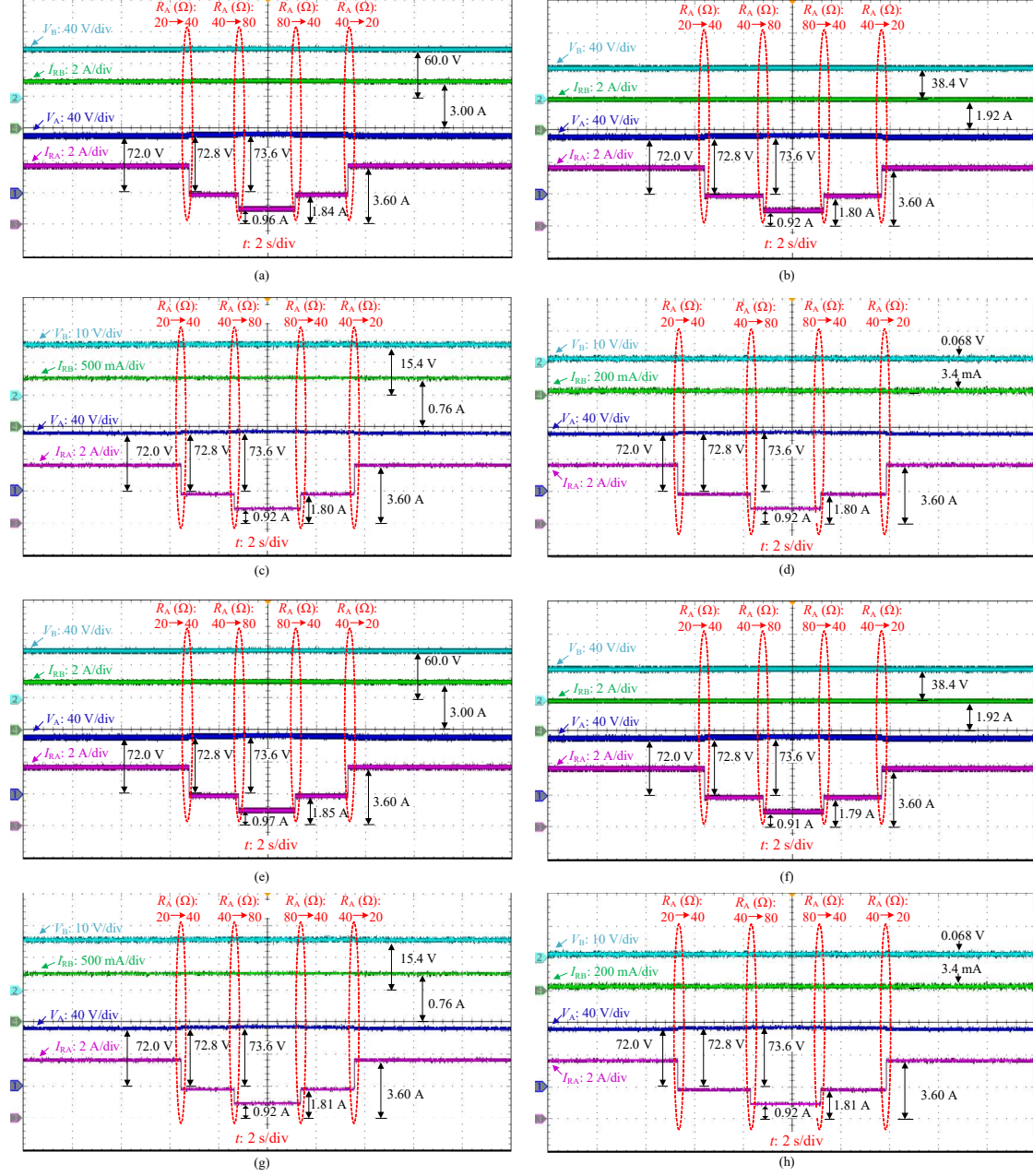
Fig. 3-15. The dynamic response values of the proposed system when R_A is changed from 20 to 40 and 80 Ω then goes back again at aligned receiver-A condition ($\alpha = 0$), maximum air gaps ($D_A = D_B = 120$ mm), and $R_B = 20$ Ω but at various β misalignment conditions: (a) $\beta = 100$ mm, (b) $\beta = 200$ mm, (c) $\beta = 300$ mm, (d) $\beta = 400$ mm, (e) $\beta = -100$ mm, (f) $\beta = -200$ mm, (g) $\beta = -300$ mm, (h) $\beta = -400$ mm.

3.4.5 Dynamic Responses Under Different Air gaps

Fig. 3-16 demonstrates dynamic responses under different airgaps (DA and DB) at aligned conditions. Therefore, $\alpha = \beta = 0$. R_A is changed from 40 Ω to 80 Ω and then goes back to 40 Ω again. The air gap of receiver A, D_A, is 120 mm. The air gap of receiver-B (D_B) is chosen as 30 mm, 60 mm, and 90 mm, as shown in Fig. 3-16 (a), (b) and (c), respectively.

The percentage change of the load R_A is 100%. Nevertheless, the rate of change of measured V_A is 1.11% (from 72.8 V to 73.6 V), which is negligible. Hence, this result shows the change of one receiver air gap cannot affect the other one's output characteristic. The load-independent output of the other receiver can still be maintained at 72 V.
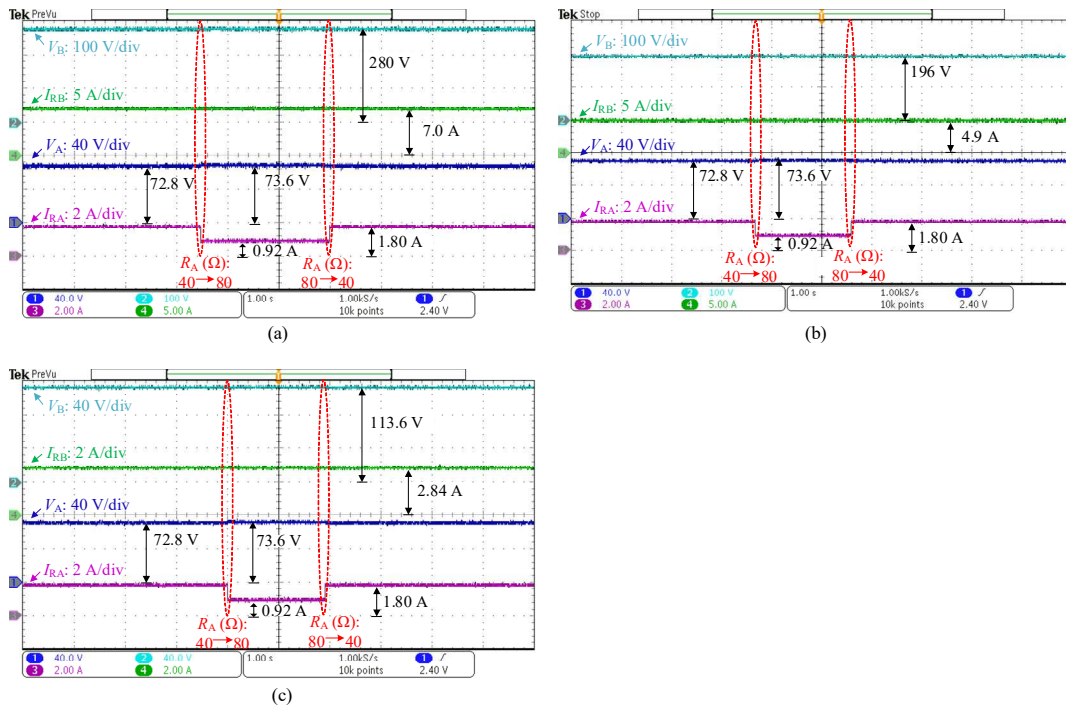
Fig. 3-16. The oscillograms with dynamic responses when RA is changed from 40 Ω and 80 Ω then goes back to 40 Ω again at $\alpha = \beta = 0$, $D_A = 120$ mm, and $R_B = 20$ Ω under different airgaps of receiver-B (D_B) conditions: (a) $D_B = 30$ mm, (b) $D_B = 60$ mm, and (c) $D_B = 90$ m.

3.4.6 Misalignment Tolerance Validation

In this chapter, only the misalignment along axis direction is considered, i.e., α and

β. Due to the symmetric structure, only β is tested. Fig. 3-17 (a) demonstrates the system's dynamic response when the receiver-B moves along with the y-axis, which can be reflected by β.

Receiver-A is in the aligned condition, which means $\alpha=0$. The position of receiver-B is changed from $\beta=0$ to $\beta=400$ mm. Loads R_A and R_B are fixed at 20Ω. Air gaps of receiver-A and -B are all set as 120 mm. The misalignment is set according to the size of the coil. The length of the coil is 400 mm. Specifically, $\beta=0$ means well-aligned and $\beta=400$ mm means fully misaligned. 120 mm airgaps comply with the industrial chassis height of an AGV.

Fig. 3-17 (b) shows that output characteristics of receiver-A (V_A and I_{RA}) are unchanged during the entire misalignment process (β from 0 to 400 mm and then to 0). This experimental result indicates that one receiver's misalignment cannot affect the output characteristics of the other receiver.
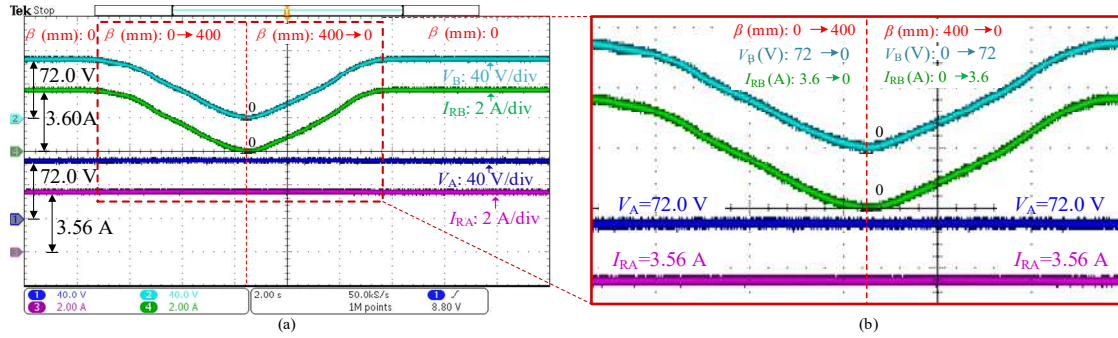
Fig. 3-17. The dynamic response of the proposed system when the $R_{X\_}B$ lateral misalignment β is changed from 0 to 400mm then goes back to 0 again at $\alpha = 0$, $D_A = D_B = 120$ mm, and $R_A = R_B = 20$ Ω.

It can be seen that the output characteristics of receiver-A are unchanged during the entire period (β from 0 to 400 mm and then to 0). This experimental result indicates that one receiver's misalignment cannot affect the output characteristics of the other receiver.

3.4.7 Efficiency vs. Output Power Under Aligned conditions

In this section, the efficiency is the overall DC-DC power transfer efficiency that is

defined as

$$\eta = P_{out}/P_{in} \tag{3.28}$$

where P_{in} is the input power and P_{out} is the output power. P_{in} can be directly measured from the DC power supply EA-PSI 9500-30, and P_{out} can be gained as

$$P_{out} = P_A + P_B \tag{3.29}$$

where P_A and P_B are the output power of receiver-A and -B, respectively. P_A and P_B can be calculated as

$$P_A = V_A^2/R_A \quad , \quad P_B = V_B^2/R_B \tag{3.30}$$

where R_B is changed from 20 Ω to 100 Ω, and load R_A is fixed at 20 Ω, 40 Ω, and 80 Ω, respectively. V_A and V_B are kept at 72 V. The 518.4 W maximum output power happens at $R_A = R_B = 20$ Ω. The presented dual-receiver system ensures the double constant voltage channel. Therefore, the maximum power should happen at the minimum resistance case ($R_A = R_B = 20$ Ω) according to (3.15). The output voltages V_A and V_B can be directly measured by oscilloscope Tektronix MDO3024. Therefore, the output power and the measured values of overall dc-dc efficiency at different loads are shown in Fig. 3-18 (a) and (b), respectively. Therefore, the measured values of overall dc-dc efficiency and the output power at different loads are demonstrated in Fig. 3-18. The highest efficiency happens at the highest power point in this system.
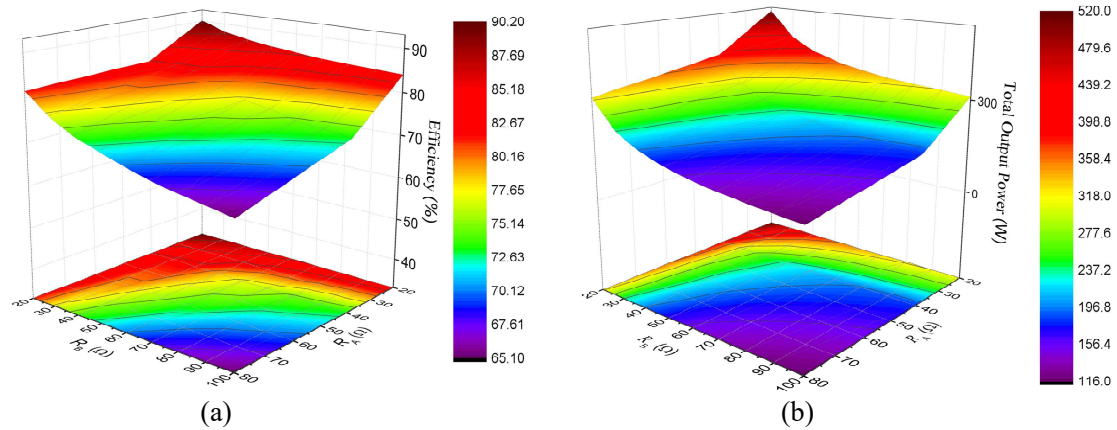
Fig. 3-18. Key measured values under different load variation conditions: (a) The total output power and (b) The overall dc-dc efficiency.

3.4.8 Efficiency vs. Output Power When One Receiver is Open Circuit

As shown in Fig. 3-19, one receiver can still work as normal when the other receiver is open. It also shows the measured values of dc-dc efficiency and the output power at different loads. Two conditions are taken into consideration. One is that receiver-A is an open circuit, and only receiver-B is working, as shown in Fig. 3-19 (a). The other one is that receiver-B is an open circuit; only receiver-A is working, as illustrated in Fig. 3-19 (b). The efficiency can arrive at ~90% when two receivers work together, as shown in Fig. 3-18. One sub-system is to charge one receiver when the other receiver is in open-circuit condition. If one receiver is in open-circuit condition and the other receiver still works normally. The maximum efficiency would drop to ~80%, as shown in Fig. 3-19. One contribution of this thesis is that two receivers can work independently. However, the efficiency drops when only one receiver is working. The reason behind it should be the no-load condition of the relay coil. Fig. 3-5 illustrates that the blue receiver Rx_B only couples with the blue DD coil in the relay part. Similarly, the yellow receiver Rx_A only couples with the yellow DD coil in the relay part. If one receiver is in the open-circuit condition, the corresponding DD coil would be in the no-load operation. That means there is no receiver coupled with the corresponding DD coil in the relay part. Therefore, the efficiency would drop in this situation.
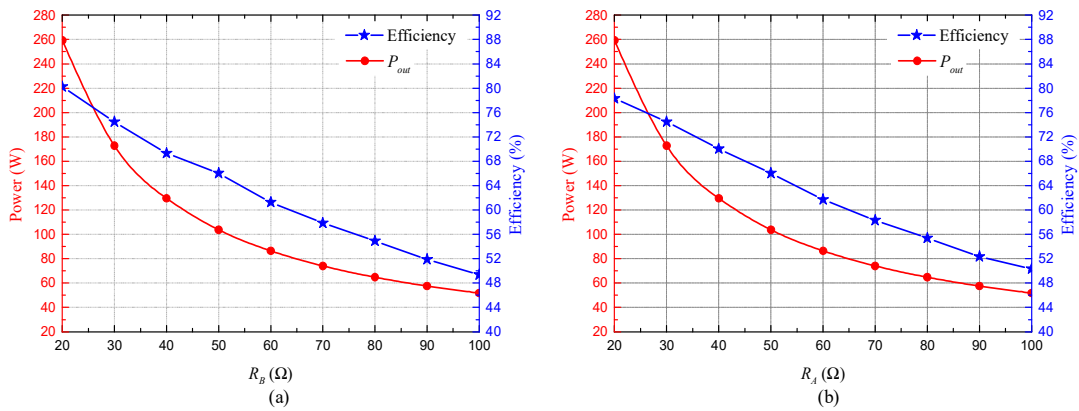
Fig. 3-19. The measured values of overall dc-dc efficiency and the output power P_{out} at different R_B conditions and $D_A = D_B = 120$ mm: (a) Receiver A is an open circuit, (b) Receiver B is an open circuit.

3.5 Benchmarking

Previous and pioneering studies set a solid foundation for double-receiver WPT systems, while still remains some research gaps that need investigating. To better explain the contribution from this chapter, several multiple-output systems are compared in TABLE 3-4. In total, the proposed system aims to make the output voltages of these two receivers independent of each other. For example, one receiver can maintain its output characteristic when the other one works in different situations, i.e., regular work, misalignment happens, airgap changes, or an open circuit occurs. Remarkably, the proposed approach avoids complex control schemes and shows low sensitivity from one receiver to the other, compared to [120], [124]- [127], [130], [138], and [139].

This chapter successfully eliminates unwanted cross-couplings in theory rather than ignoring or assuming them as zero. As a result, this system ensures that each receiver can work independently. Thus, there is no need to work simultaneously compared to [120], [126]-[116], and [139]. Then, the output type means load-independent outputs, representing the output values regardless of load variation. The proposed method ensures two load-independent outputs by eliminating unwanted cross-couplings among the source coil and receivers.

Next, several impressive predecessor studies adopt additional R_X auxiliary circuits means the system needs additional circuits to cancel out the cross-couplings by inserting reactance, e.g., changing resonant frequencies [132], [133], or changing phase angles [134]. These circuits are not the essential resonant parts. Fortunately, such circuits are not needed in the proposed method, thereby contributing to a simple and compact system. Compared to the bucking coil that requires a delicate design [135], the proposed system is easy to design for engineers because the decoupling is from the shape rather than specific turns, which significantly shortens the design period. Therefore, design freedom is greatly enhanced since turns can be changed according to the charging requirements. Moreover, the proposed structure can save space and size

from the receiver side. The R_X-side space is valuable and limited, as there is plenty of electronic equipment that needs installing, e.g., energy storage device, positioning systems, or communication device. Hence, the proposed design is extremely suitable for EVs that need double independent power supplies with a fixed operational frequency.

TABLE 3-4. MULTIPLE-OUTPUT SYSTEM COMPARISON

Paper \ Parameter	This thesis	[120]	[124]	[127]	[116]	[130]	[134]	[135]	[139]	[140]
Decoupling type	Coil shape	no	Physical	Magnetic Shield	Circuit-based	Circuit-based	Circuit-based	Coil turns	Magnetic Shield	Circuit-based
Complex control	no	no	no	no	no	no	yes	no	no	yes
Sensitivity to the other receiver's misalignment or airgap changes	low	high	high	high	low	high	low	low	high	low
Quantitative Misalignment region β (cm)	[-40,40]	---	---	---	---	---	---	[0,10]	---	---
Independent work	yes	no	yes	no	no	---	yes	yes	no	---
Output type	CV	---	---	CC	---	---	---	---	CV	---
One R_X open circuit discussion	yes	no	no	no	no	no	---	no	no	no
ZPA achievement	yes	---	---	no	---	---	no	---	yes	---
Each R_X-capacitor number	1	1	1	2	1.5	Adjustable	1	1	3	1
Each R_X-inductor number	1	1	1	2	1	1	1	1	3	1
Additional R_X auxiliary circuit	no	no	no	no	need	need	need	no	no	need
Max. Load Power (W)	518.4	117.2	9.5	1.157	325	0.2	27	---	13.53	2000
Max. Measured Efficiency (%)	90.16	~75	~90	~60	~93.2	~91	~92	99.2	89.79	90.6
Max. Size or Max. Diameter (cm)	40×40	15.5	18	15×15	10×10	16	---	30	18×17.5	64×20
Max. airgap between Tx and Rx or among adjacent couplers (cm)	12	30	---	6.5	5	---	---	13	5	7.5
Applications	Industrial power supplies	---	---	Gate drivers	AGVs	WPT-LAN	---	---	Gate drivers	Locomotives
Operating Frequency (kHz)	85 (SAE)	200	240	300	85 (SAE)	4600	160.1	85 (SAE)	200	20

"---" means not being discussed in the reference.

3.6 Summary

Overall, this chapter introduces a novel double-receiver WPT system. Measured values of unwanted cross-couplings are k_{1A} (0.003), k_{1B} (0.003), and k_{AB} (0.003), which are significantly mitigated and can be regarded as null, thanks to the proposed magnetic coupler. After eliminating cross-couplings among receivers and the source coil, both receivers can achieve load-independent outputs. After eliminating the cross-couplings

between two receivers, one receiver cannot affect the other one. Most importantly, the proposed system frees engineers to design the magnetic couplers based on practical design purposes since different engineering applications may have different coil turns. The proposed decoupling approach is flexible and suitable for these applications because the decoupling depends on shapes rather than the delicate design of turns. Moreover, there is no complicated control or additional reactance, leading to a simple and compact system. In addition, the inverter can achieve ZPA, thereby reducing the volt-ampere rating and enhancing efficiency.

An experimental prototype with double receivers was constructed to verify the characteristics of the proposed system. Experimental results show remarkable agreement with the theoretical analysis. Firstly, the voltage of each receiver can maintain constant under varying load conditions, leading to excellent robustness. The prototype can achieve a 90.16% maximum dc-dc efficiency at 12 cm air gaps when delivering 518.4 W to loads. This design can be generalizable to other output voltage or power levels to meet different charging demands, especially for equipment that needs double independent power supplies with a fixed operational frequency. The potential applications are AGVs and industrial power supplies.

The dual-receiver system can generate different outputs without a complex circuit and control method. For numerous dual-receiver WPT systems for AGVs, the receivers are mounted nearby or overlapping, which may decrease the transfer efficiency and cause the outputs to be interfered with by each other. These drawbacks are caused by the undesirable cross-couplings, which are successfully eliminated by the presented structure. Moreover, the presented magnetic coupler not only decouples one receiver from the other one but also eliminates the coupling between the transmitter and receivers. Thus, the load-independent constant voltage outputs can be realized. Two output channels from two receivers both ensure the CV output regardless of the load variation, which is suitable for industrial power supplies as a stable dual-output charger.

After discussing AGVs, the next chapter will focus on a more popular electric vehicle, i.e., electric bicycles (EBs). A special magnetic resonator using Helmholtz coils

and the S-SP/S compensation network will be introduced.

Chapter 4

Helmholtz Magnetic Coupler in WPT for EBs

Recently, more and more attention has been paid to electric bicycles (EBs) charging using wireless power transfer (WPT) techniques due to their merits of convenience and safety. Therefore, we have developed an electric bicycle charging system using Helmholtz coils and the full analysis and experiment have been conducted. The results are very promising, and it represents a useful and applicable system for electric bicycles or similar wheel-based charging systems.

4.1 Review of EB Wireless Charging

The electric bicycle (EB) is one of the most promising electric vehicles (EVs) that gain the merits of convenience, low carbon emission, and low cost [9], [5]. However, conventional EBs need power cables to charge the battery, which may suffer from electrical leakage in some harsh environments [141]. To this end, pioneers have studied wireless power transfer (WPT) techniques for EB charging systems [4]-[9]. For instance, a double-coupled inductive system is proposed for multi-pickup systems, aiming at charging a fleet of electric bicycles wirelessly [142]. Some control approaches such as advanced FPGA control are also widely used in inductive power transfer (IPT) systems for wireless charging EBs [56]. Then, to avoid complex control algorithms, reconfigurable coils or circuits are adopted to realize constant voltage (CV) or constant current (CC) for charging EBs wirelessly. For example, Li et al. proposed a variable-coil-structure-based WPT system to charge EBs [143]. By splitting and reconfiguring the transmitter coil structure, the proposed WPT system can achieve CC and CV outputs by switching between two circuit topologies. Similarly, reconfigurable circuits are also successfully adopted. For example, a reconfigurable intermediate resonant circuit-based WPT is investigated to charge batteries for EBs, which achieves CC and CV outputs by switching the intermediate circuit [64]. Reconfigurable circuits with AC switches (ACSs) are also studied, such as [144] and [145]. Specifically, reference [144]

employs an additional capacitor with an ac switch at the primary side to achieve CC and CV charging. Reference [145] utilizes a hybrid topology with two AC switches (ACSs) at the secondary side, offering configurable CC and CV outputs by turning ON/OFF two ACSs.

Their efforts set a solid foundation for more convenient, reliable, and safer EB wireless battery charging while still remaining some research gaps in achieving optimal WPT system designs. First, the mutual couplings between the transmitter and receiver coils are designed with precise alignment at specific positions [64], which means the rotational, angular, and lateral misalignments can affect the charging performance. Second, communication channels are required between the transmitters and receivers for feedback control of battery charging current and voltage in [56], [57]. The additional communication devices will deteriorate both system cost and reliability. Third, user-end converters or battery management systems (BMS) are needed in the receivers, which can significantly reduce their power density and increase the weight and size of battery containers [58]. Moreover, complicated control methods, such as primary side control [59], power flow control [60], dual side control [61], H∞ control [62], and μ-synthesis approach [63] are generally adopted to regulate the converters in realizing good robustness against load and coupling variations. Fourth, LCC or LCL compensation networks are needed at the receiver side in achieving constant voltage (CV) charging of batteries in [64], [65], [66]. Such a compensated inductor not only brings bulky size and heavier weight for the EBs but also lowers the power transfer efficiency in terms of non-negligible equivalent series resistances (ESRs). In practice, undesirable high-order harmonics may also arise from the resonance between the switched compensated inductors and parasitic capacitances.

Fig. 4-1. Photograph of the prototype.

To address those issues, both transmitting and receiving resonators are newly designed with full considerations of high reliability, efficiency, and practicability. A photograph of the prototype is shown in Fig. 4-1. The transmitting coil is a pair of Helmholtz coils that is optimally designed to have constant mutual coupling with the receiver coil. A mutual-independent series (S) capacitor is adopted for compensating the transmitting coil. The receiver coil is the conventional spiral coil that remains a slim structure inside the EB. A series capacitor is used for compensating the inductance of the receiving coil during the CV charging process, and a series-parallel (SP) network is adopted during the constant current (CC) charging process. It is worthy to note that the parameters of both S and SP compensation networks are dependent on the mutual inductance. However, since the mutual inductance has been well designed to be constant, the parameters of the SP network can be preliminarily designed with fixed values. The newly designed WPT resonators inherit the merits of conventional WPT systems in achieving load-independent CC and CV charging while making progress in resolving existing issues of WPT systems for EBs:

(i) The mutual coupling between the transmitting and receiving coils is constant, which can tolerate rotational, angular, and lateral misalignments.

(ii) No communication channels and additional converters are required since the CC and CV charging can be implemented via the S-SP/S compensation scheme.

(iii) Conventional identification and control strategies are not necessary. The switching from S-SP compensation to S-S compensation needs only a comparison between the state-of-charge (SoC) or output voltage of the battery and their respective references.

(iv) Due to the constant mutual inductance, more succinct compensation schemes can be adopted at the receiver side to achieve constant CC and CV charging. Thus, the conventional LCL and LCC compensation schemes are not required anymore.

The main contributions are summarized as follows:

1) Helmholtz Coils: This work utilizes a magnetic coupler to enhance

misalignment tolerance. Specifically, the combination of Helmholtz and spiral coils has been rarely discussed in the past. Therefore, this work investigates this structure. Moreover, it is exceptionally suitable for EBs.

2) Symmetrical structure: conventional WPT chargers rarely consider the mechanical shape of EBs. The proposed structure can be integrated into the locker for EBs in the public area. As illustrated in Fig. 4-1, the proposed structure matches the mechanical shape. There is no need for extra space to install the charger, which can save valuable space in metropolitans like New York, London, and Hong Kong. The proposed topology ensures a compact and integrated possibility for future EBs. A receiver can be integrated into the bike wheel, and transmitters can be integrated with the mechanical support. The passive devices (transmitters and receivers) are the bulkiest components of the WPF, and the power electronic converters are less bulky and can usually be fabricated using high power density techniques. Moreover, compared to DD-shaped transmitters and receivers in [10], the proposed Helmholtz and spiral coils are symmetric in shape. That means superiority in rotational misalignment can be realized, which is extremely important to a cycling movement device like EBs. When rotational misalignment happens, the proposed structure incredibly maintains the same output performance due to the symmetric structure.

3) A compact and simple system to realize CC and CV: Without complicated control or DC/DC converters to regulate outputs, a tight and compact structure can be achieved. By using a linked switch, the capacitors on the receiver side can be designed to be more compact.

4) There is no communication between transmitter and receiver, which significantly enhances the simplicity of the system. There is also no need to consider the associated electromagnetic interference (EMI) problems between the power and communication systems.

5) Special compensation networks for mutual and self-inductance together: S-S compensation can realize CV, whereas S-SP can realize CC. And efficiency

can also be maintained as stable under different positions.

4.2 The Magnetic Coupling Structure

4.2.1 Theoretical Analysis

According to the real size of an EB prototype in Fig. 4-1, all coil sizes are designed to meet the industrial demand. For example, Fig. 4-2 illustrates that the diameter of the Helmholtz transmitting coil is 240 mm. The diameter of the spiral receiving coil is 130 mm.

Furthermore, Helmholtz coils can be designed to generate a region of a nearly uniform magnetic field. As demonstrated in Fig. 4-2, when the electrical current flows in the same direction through the Helmholtz coils (i.e., T_{X1} and T_{X2}), a highly uninformed magnetic field in a 3-dimension volume of space between T_{X1} and T_{X2} can be created. p defines the position of the receiver and is the parameter to analyze the misalignment in the subsequent analysis.
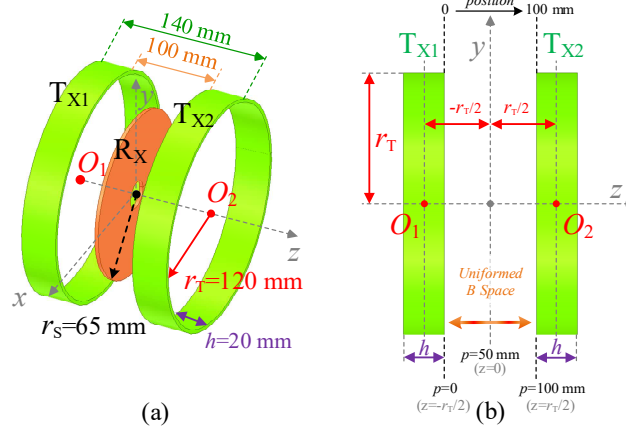
Fig. 4-2. The magnetic coupler with Helmholtz transmitting coils and a spiral receiving coil: (a) overview and (b) front view.

Specifically, the flux density B_1 and B_2 are generated by transmitter coil T_{X1} and T_{X2}, respectively, which can be expressed as [146]

$$B_1 = \frac{\mu_0 INR^2}{2\left(R^2 + (z - R/2)^2\right)^{3/2}} \quad , \quad B_2 = \frac{\mu_0 INR^2}{2\left(R^2 + (z + R/2)^2\right)^{3/2}} \tag{4.1}$$

where z is a point distance from the center of a pair of Helmholtz coils. N is the number of turns in one coil. R is the radius of coils. I is the current flowing through Helmholtz coils. Then, the total flux density generated by the Helmholtz transmitter can be expressed as

$$B_z = B_1 + B_2 \tag{4.2}$$

Next, the magnetic field near the center of the coils is often studied by considering the field along the axis and using the Taylor series to examine the uniformity of the field, which can be expressed as [147]

$$B(z) = B(0)\left\{1 - \frac{144}{125}\left(\frac{z}{R}\right)^4 + \cdots\right\} \tag{4.3}$$

where z is also the distance along the axis from the center of the two coils. And such a pair of coils is used as the transmitter in this work. Therefore, a highly uniform magnetic field Bz can be gained in the space between transmitters T_{X1} and T_{X2}, which ensures one prerequisite for stable power transferability.

The other transferability requirement is that the receiver is able to capture enough flux generated by the transmitter to ensure the designed output values. Thus, the mutual inductance, which implies the coupling degree between two sides, can be adopted to evaluate the magnetic linkage.

As shown in Fig. 4-2 (a), Helmholtz coils are adopted as the transmitter to generate an almost uniform electromagnetic field. All flux generated by the Helmholtz transmitters can be written as

$$\Phi_{all} = \Phi_M + \Phi_l \tag{4.4}$$

where Φ_l is the leakage flux that is not coupled with the receiving spiral coil. Φ_M is the linkage flux between the proposed transmitter and receiver, which can be expressed as

$$\Phi_M = B \cdot S \tag{4.5}$$

where B is the constant flux density generated by the Helmholtz transmitters, and S is the area of the spiral receiver coil. In this work, the spiral coil is adopted as the receiver due to its slim, simple, and symmetric structure. Then, the coupling coefficient between the proposed transmitter and receiver can be expressed as

$$k = \left| \Phi_M / \Phi_{all} \right| \tag{4.6}$$

where k is the coupling coefficient, which can be regarded as stable in this 3-dimension volume of space between T_{X1} and T_{X2}. Thus, a nearly constant mutual inductance can also be obtained, which can be expressed as

$$M = k\sqrt{L_P L_S} \tag{4.7}$$

where L_P is the total self-inductance of Helmholtz coils and LS is the self-inductance of the receiving coil. Then, it is necessary to verify the distribution of the magnetic field and design the parameters of the coils. Thus, this work adopts ANSYS Maxwell to conduct finite element analysis (FEA) for the proposed coupling structure.

4.2.2 Finite Element Analysis Verification

Finite element analysis is a strong tool to validate the magnetic field through field simulation. Fig. 4-3 demonstrates the simulated magnetic flux density (at 200 kHz) observed from the x-axis of Fig. 4-2, which shows that a highly uniform magnetic field can be generated by the Helmholtz transmitter. Then, the spiral receiver is designed to suit this charging region. At the highly uniformed magnetic field, the mutual inductance between the transmitter coil and receiver coil should be kept relatively constant. The inductances are listed in TABLE 4-1, which demonstrates that the simulated value highly agrees with the measured values using the LCR meter RS-Pro LCR 6300.

TABLE 4-1. PARAMETERS OF THE COILS

T_X Coil	Simulation Value	Experimental Value
No. of turns N_{TX}	11+11	11+11
Diameter (mm)	240	242
L_{TX} (μH)	137.43	135.47
R_X Coil	Simulation Value	Experimental Value
No. of turns N_{RX}	15	15
Outer Diameter (mm)	130	131
Inner Diameter (mm)	61	59
L_{RX} (μH)	25.56	26.81
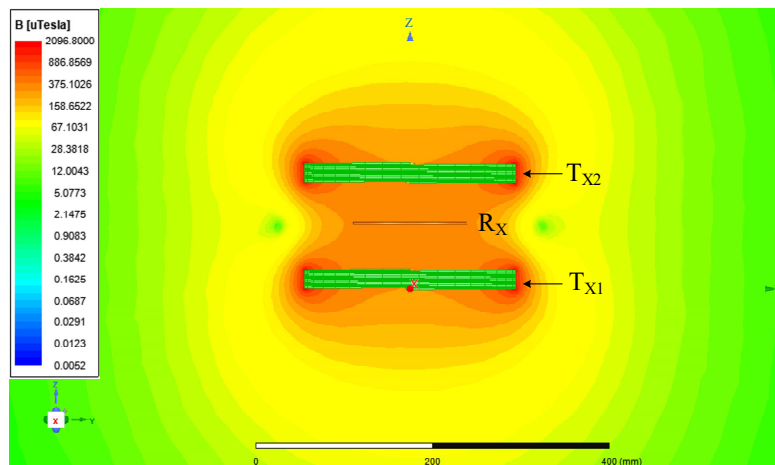
Fig. 4-3. The simulated magnetic flux density of the proposed structure by FEA.

4.2.3 Magnetic Coupler Design Procedure with FEA Simulation

A step-by-step design procedure of the proposed WPT system is also shown in Fig. 4-4. Here, δ is the difference between the maximum and minimum simulated mutual inductance. And $\varDelta$ is the tolerance of mutual inductance change. The magnetic coupler is designed according to the physical requirements, providing a large charging area with a slight mutual inductance variation.

```
                         ┌─────────┐
                         │  Start  │
                         └─────────┘
                              │
                              ▼
          ┌───────────────────────────────────────────┐
          │  Given $U_{in}$, $\omega$, and desired $U_B$, $I_B$  │
          └───────────────────────────────────────────┘
                              │
                              ▼
     ┌─────────────────────────────────────────────────────┐
     │  Determine according to the physical requirements,    │
     │  misalignment area and tolerance of mutual            │
     │  inductance variation $\Delta$                        │
     └─────────────────────────────────────────────────────┘
                              │
                              ▼
          ┌──────────────────────────┐        ┌──────────┐
          │  Design magnetic coupler  │◄───────│ Modify   │
          └──────────────────────────┘        │ turns or │
                              │                │ sizes    │
                              ▼                └──────────┘
     ┌─────────────────────────────────────────┐   ▲
     │ Calculating the mutual inductance        │   │
     │ variation $\delta$ under this charging   │   │
     │ area by ANSYS Maxwell                    │   │
     └─────────────────────────────────────────┘   │
                              │                     │
                              ▼           No        │
                    ╱─────────────╲────────────────┘
                    ╲ $\delta \leqq \Delta$ ? ╱
                    ╲─────────────╱
                              │ Yes
                              ▼
          ┌───────────────────────────┐
          │  Finalize parameter values │
          └───────────────────────────┘
                              │
                              ▼
                         ┌─────────┐
                         │   End   │
                         └─────────┘
```
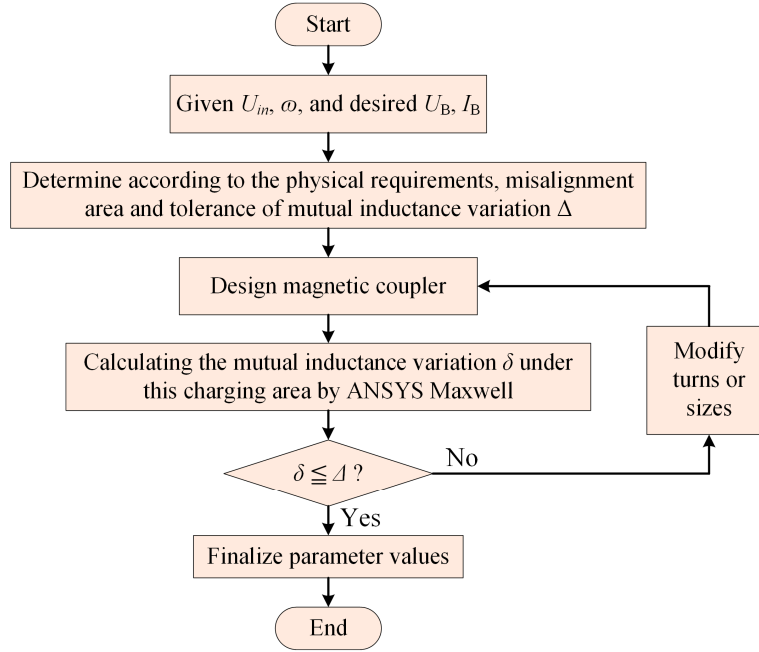
Fig. 4-4. Diagram of the design procedure of considering the large charging area with a tight mutual inductance variation.

4.2.4 Lateral Tolerance Improvement

The simulated mutual inductances versus the z-axis and x-axis are shown in Fig. 4-5. It can be seen that the mutual inductance can be maintained in the range from 8.814 μH to 9.456 μH when p∈ [20 mm,80 mm], x∈ [-40 mm,40 mm], which are set as the movement space of the receiving coil. Due to the symmetric structure, the partial area is adopted for simplified estimation for misalignment tolerance. Thus, this stable mutual inductance can be regarded as constant in such a charging space, which shows excellent lateral misalignment tolerance. Next, the rotational misalignment tolerance and angular misalignment are taken into consideration.
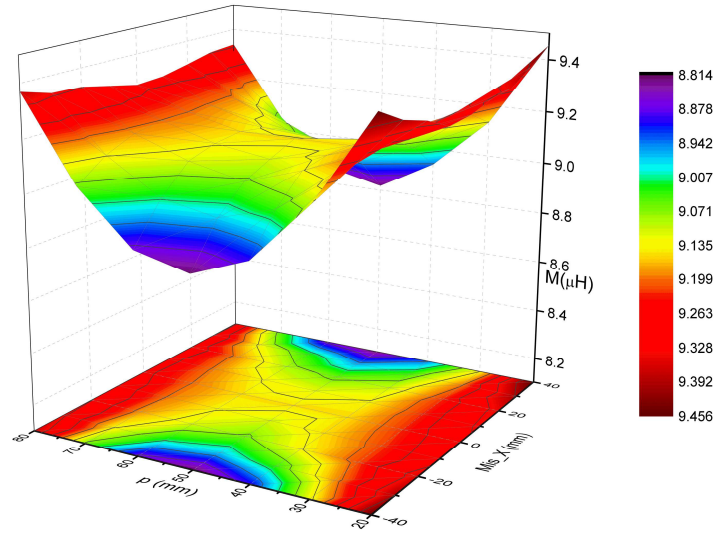
Fig. 4-5. The simulated results of the mutual inductance between the Helmholtz transmitter and the

spiral receiver.

4.2.5 Rotational Misalignment Tolerance Enhancement

Due to the symmetric structure, the proposed magnetic coupler can maintain the mutual inductance constant when misalignment occurs. Fig. 4-6 (a) illustrates the directions of angular and rotational misalignment angles, including X_Angle, Y_Angle, and Z_Angle. Then, Fig. 4-6 (b) demonstrates the simulated results under different rotational angles (i.e., Z_Angle). It can be seen that the mutual inductance deviates within 0.1% at different Z_Angle, thanks to the symmetric structure. And angular misalignment tolerance (i.e., X_Angle and Y_Angle) is discussed in section 4.2.6.

(a)   (b)
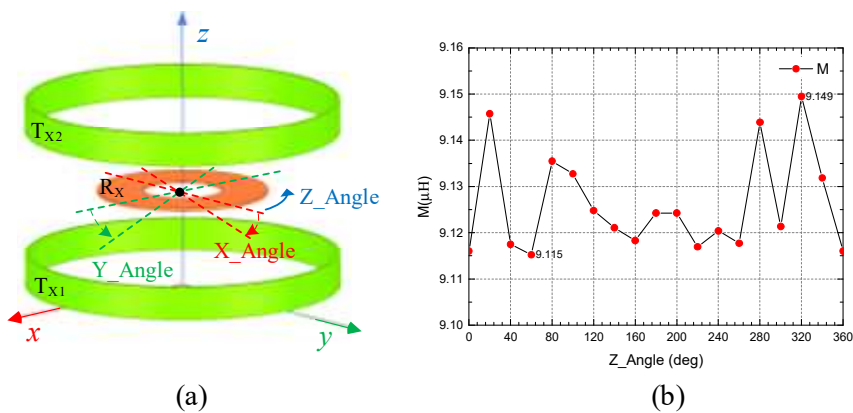
Fig. 4-6. (a) The rotational misalignment with Z_Angle and (b) The change of mutual inductance vs.

Z_Angle at *p*=50 mm.

4.2.6 Angular Misalignment Tolerance Enhancement

Fig. 4-7 demonstrates angular misalignment situations, including the angular misalignment along the x-axis and y-axis, respectively. Due to the symmetric structure, only four different positions are analyzed for the sake of simplified analysis, including 50 mm, 60 mm, 70 mm, 80 mm positions which is a reasonable range of misalignment as compared to the size of the coil and the wheel. The radius of the receiver coil is 65 mm. And the radius of the wheel is set as 120 mm.
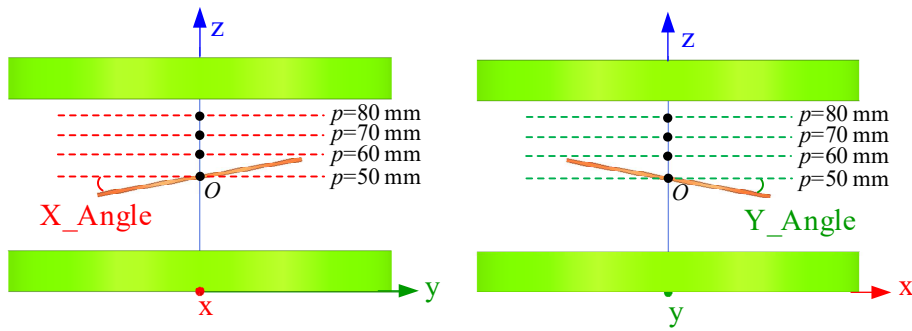
Fig. 4-7. (a) The rotational misalignment with Z_Angle and (b) The mutual inductance change vs. Z_Angle at *p*=50 mm.

Then, the degree of angular misalignments can be reflected in misalignment angles (i.e., X_Angle, and Y_Angle). The result can be seen in Fig. 4-8, which illustrates that the maximum mutual inductance is 9.282 µH, whereas the minimum mutual inductance is 8.560 µH. The maximum mutual inductance difference is 0.722 µH among different X_Angles, Y_Angles, and positions.
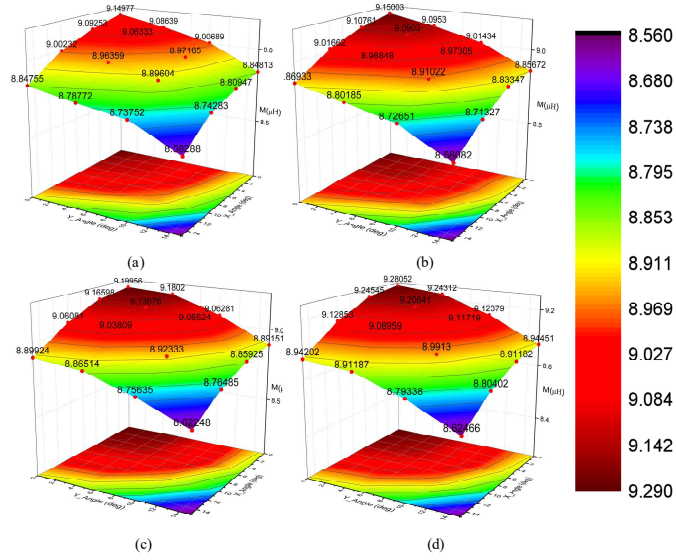
Fig. 4-8. The FEA simulated results when angular misalignment happens at different positions: (a) *p*=50mm, (b) *p*=60mm, (c) *p*=70mm, and (d) *p*=80mm.

4.3 Analysis of The Proposed Resonator system

Fig. 4-9 (a) demonstrates the topology of the proposed coil structure, where the transmitter coil can be split into two coils, i.e., L_{P1} and L_{P2}, and they are connected in series. The receiver coil is represented by L_S. Magnetic couplings among them are reflected by mutual inductances, i.e., M_0 between L_{P1} and L_{P2}, M_1 between L_{P1} and L_S, and M_2 between L_{P2} and L_S. R_P and R_S are the ESRs on the primary and secondary sides, respectively. And *S* denotes the linked switch, aiming to reconfigure the circuit topology. Specifically, the entire system works in the CC mode when S is turned on, as shown in Fig. 4-9. The entire system works in the CV mode when S is switched off, as shown in Fig.4.10. The switch can be implemented by the low-cost relay or MOSFETs.
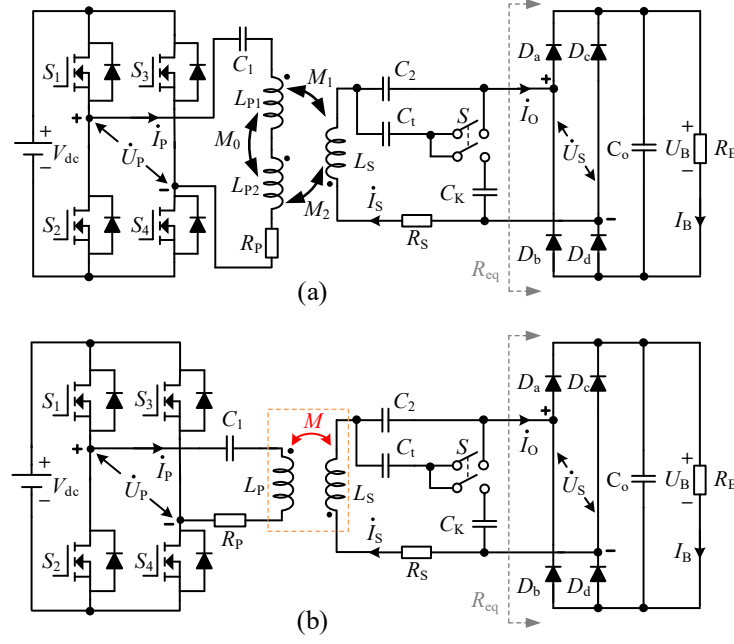
Fig. 4-9. Circuitry of the proposed WPT system: (a) The entire circuit topology of the proposed system and (b) The equivalent decoupling circuit scheme.

To simplify the analysis without losing generality, an equivalent decoupling circuit is depicted, as shown in Fig. 4-9 (b). Therefore, two transmitter coils form a coupled inductor. The total self-inductance L_P can be written as

$$L_P = L_{P1} + L_{P2} + 2M_0 \tag{4.8}$$

Then, the total magnetic coupling between this L_P and the receiver L_S can be reflected by a total mutual inductance M, which can be written as

$$M = M_1 + M_2 \tag{4.9}$$

By optimizing the FEA model in the Maxwell, L_P and M can be regarded as constant in the charging space. That ensures the desirable magnetic performance in the proposed system. Then, as for electrical performance, the entire circuit is illustrated in Fig. 4-9 (b). Firstly, the input dc voltage of the H-bridge inverter is V_{dc}. Then, the inverter is equipped at the source side to feed transmitters. With the help of fundamental harmonics approximation (FHA), the inverter output voltage can be written as

$$u_{\mathrm{P}}(t) = \frac{4}{\pi} V_{\mathrm{dc}} \sin\frac{\delta}{2}\sin\omega t \tag{4.10}$$

where δ is the conduction angle of $u_1(t)$. ω is the angular frequency, which can be expressed as

$$\omega = 2\pi f \tag{4.11}$$

where f is set as 200 kHz to comply with the Qi-standard.

For further analysis, the fundamental phasor root mean square (RMS) form of $u_{\mathrm{P}}(t)$ is used, which can be expressed as

$$\dot{U}_{\mathrm{P}} = \frac{2\sqrt{2}}{\pi} V_{\mathrm{dc}} \sin\frac{\delta}{2}\angle 0° \tag{4.12}$$

A full-bridge rectifier is constructed with diodes (D_{a}, D_{b}, D_{c}, and D_{d}) and a capacitor (C_{o}), which aims to convert AC power to DC power for battery charging. In terms of such a rectifier, the value relationships between ac inputs (U_{S} and I_{O}) and DC outputs (U_{B} and I_{B}) can be described as

$$U_{\mathrm{S}} = 2\sqrt{2}U_{\mathrm{B}}/\pi \ , \ I_{\mathrm{O}} = \sqrt{2}\,\pi I_{\mathrm{B}}/4 \ , \ R_{eq} = 8R_{\mathrm{B}}\pi^{-2} \tag{4.13}$$

where R_{B} is the equivalent resistance of the battery load.

According to the mutual coupling theory, the equivalent circuit model of the proposed WPT system can be depicted, as shown in Fig. 4-9. In this work, two resonant networks are taken into consideration, namely, S-SP resonant network and S-S network. These two different circuit topologies can be realized by reconfiguring the circuit topology.

In order to achieve CC and CV charging, the circuit schemes need reconfiguring. Different topologies can be realized when the switch S is turned ON/OFF, as illustrated in Fig. 4-10 and Fig. 4-11, respectively. Therefore, a linked switch is used to reconfigure the circuit scheme, which not only simplifies the number of switches but makes use of capacitors as well.
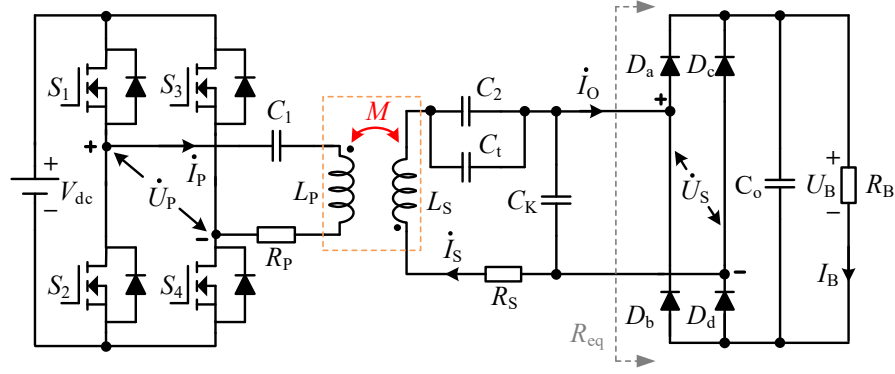
Fig. 4-10. The circuitry of the proposed WPT system with S-SP compensation network when the switch *S* is turned ON.
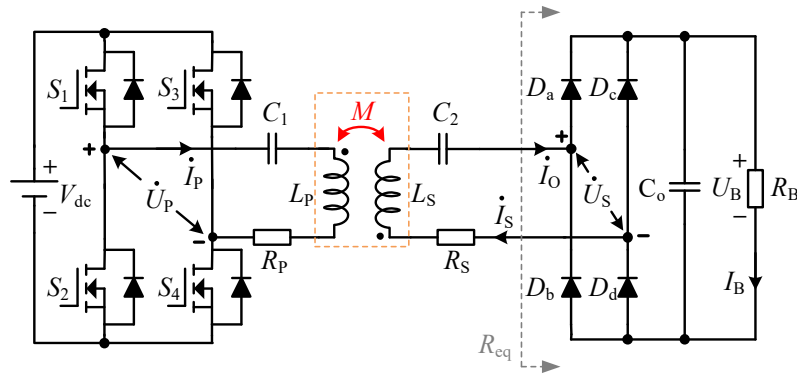
Fig. 4-11. The circuitry of the proposed WPT system with S-S compensation network when the switch *S* is turned OFF.

In this section, due to the invariant mutual inductance, the compensated networks can be designed without considering the effect of mutual coupling variations. For instance, the S-SP compensated topology can be used to achieve CC charging. An equivalent circuit model at the fundamental resonant frequency can be plotted as shown in Fig. 4-12.
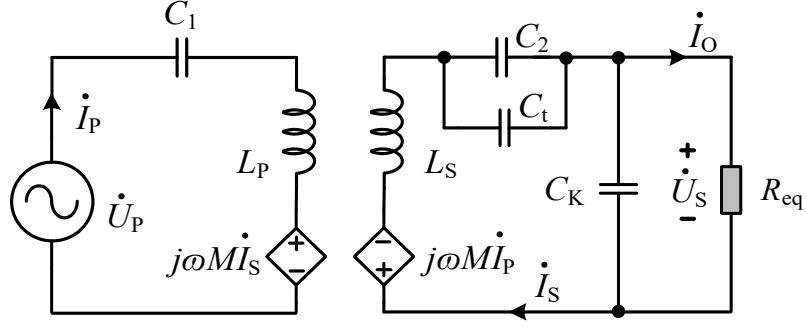
Fig. 4-12. Schematic diagram of the proposed WPT system with the S-SP compensation.

According to Kirchhoff's circuit laws, the following equation can be gained as

$$\begin{cases} \dot{U}_{\mathrm{P}} = \left(j\omega L_{\mathrm{P}} + \left(j\omega C_{1} \right)^{-1} \right) \dot{I}_{\mathrm{P}} + j\omega M \dot{I}_{\mathrm{S}} \\ 0 = j\omega M \dot{I}_{\mathrm{P}} + \left[j\omega L_{\mathrm{S}} + \left(j\omega (C_{2} + C_{\mathrm{t}}) \right)^{-1} \right] \dot{I}_{\mathrm{S}} + R_{\mathrm{eq}} \dot{I}_{\mathrm{O}} \\ \dot{U}_{\mathrm{S}} = R_{\mathrm{eq}} \dot{I}_{\mathrm{O}} \\ \dot{I}_{\mathrm{S}} = j\omega C_{\mathrm{K}} \dot{U}_{\mathrm{S}} + \dot{I}_{\mathrm{O}} \end{cases} \tag{4.14}$$

where the dot version means the phasor form of the parameter.

Then, this equation can be rewritten as

$$\dot{U}_{\mathrm{P}} = Z_{a} \dot{I}_{\mathrm{P}} + Z_{b} \dot{I}_{\mathrm{S}} + Z_{c} \dot{U}_{\mathrm{S}} + j\omega M \dot{I}_{\mathrm{O}} \tag{4.15}$$

where Z_{a}, Z_{b}, and Z_{c} can be expressed as

$$\begin{cases} Z_{a} = j\omega \left(L_{\mathrm{P}} + M \right) + \left(j\omega C_{1} \right)^{-1} \\ Z_{b} = j\omega L_{\mathrm{S}} + \left[j\omega (C_{2} + C_{\mathrm{t}}) \right]^{-1} \\ Z_{c} = 1 - \omega^{2} M C_{\mathrm{K}} \end{cases} \tag{4.16}$$

where the compensated capacitors C_{1}, C_{2}, and C_{K} are designed to satisfy:

$$\begin{cases} C_{1} = \left[\omega^{2} \left(M + L_{P} \right) \right]^{-1} \\ C_{2} + C_{t} = \left[\omega^{2} L_{S} \right]^{-1} \\ C_{\mathrm{K}} = \left[\omega^{2} M \right]^{-1} \end{cases} \tag{4.17}$$

Then, (4.15) can be rewritten as

$$\dot{U}_{\mathrm{P}} = j\omega M \dot{I}_{\mathrm{O}} \qquad (4.18)$$

Thus, the ac input current of the rectifier can be obtained as

$$\dot{I}_{\mathrm{O}} = \dot{U}_{\mathrm{P}} / j\omega M \qquad (4.19)$$

Also, the battery charging current I_{B} can be derived as

$$I_{\mathrm{B}} = \frac{8V_{\mathrm{dc}}}{\pi^2 \omega M} \qquad (4.20)$$

Apparently, the battery charging current is independent of the load. Since the mutual inductance of the proposed resonators is constant, the battery charging current only depends on the input voltage and angular frequency.

The S-S compensated topology can be adopted to realize CV charging. An equivalent circuit model at the fundamental resonant frequency can be plotted as shown in Fig. 4-13.
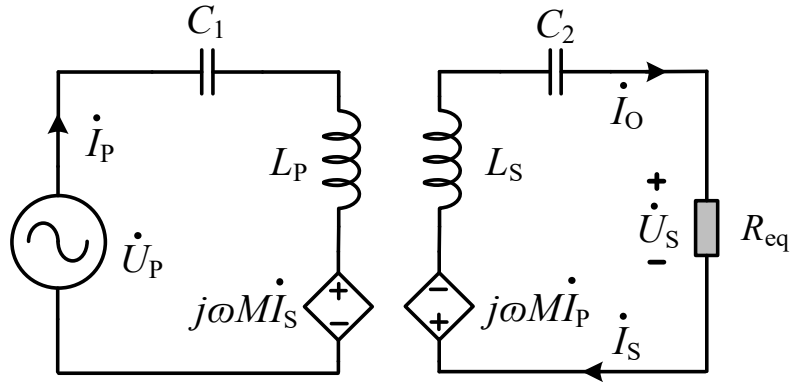
Fig. 4-13. Schematic diagram of the proposed WPT system with the S-S compensation.

According to the Kirchhoff's circuit laws,

$$\begin{cases} \dot{U}_{\mathrm{P}} = \left(j\omega L_{\mathrm{P}} + \left(j\omega C_{1} \right)^{-1} \right) \dot{I}_{\mathrm{P}} + j\omega M \dot{I}_{\mathrm{S}} \\ 0 = j\omega M \dot{I}_{\mathrm{P}} + \left(j\omega L_{\mathrm{S}} + \left(j\omega C_{2} \right)^{-1} + R_{\mathrm{eq}} \right) \dot{I}_{\mathrm{S}} \\ \dot{U}_{\mathrm{S}} = R_{\mathrm{eq}} \dot{I}_{\mathrm{O}} \\ \dot{I}_{\mathrm{S}} = \dot{I}_{\mathrm{O}} \end{cases} \qquad (4.21)$$

Then, the above equation can be rewritten as

$$\dot{U}_{\mathrm{P}} = Z_d \dot{I}_{\mathrm{P}} + Z_e \dot{I}_{\mathrm{S}} + \dot{U}_{\mathrm{S}} \tag{4.22}$$

where Z_d and Z_e can be expressed as

$$\begin{cases} Z_d = \mathrm{j}\omega(L_{\mathrm{P}} + M) + (\mathrm{j}\omega C_1)^{-1} \\ Z_e = \mathrm{j}\omega(L_{\mathrm{S}} + M) + (\mathrm{j}\omega C_2)^{-1} \end{cases} \tag{4.23}$$

where the compensated capacitors C_1 and C_2 are designed to satisfy:

$$C_1 = \left[\omega^2 (M + L_P)\right]^{-1} \quad , \quad C_2 = \left[\omega^2 (M + L_S)\right]^{-1} \tag{4.24}$$

Then, the ac input voltage of the rectifier can be expressed as

$$\dot{U}_{\mathrm{S}} = \dot{U}_{\mathrm{P}} \tag{4.25}$$

Subsequently, the battery charging voltage U_{B} can be derived as

$$U_{\mathrm{B}} = V_{\mathrm{dc}} \tag{4.26}$$

Obviously, the battery charging voltage is also load-independent when the S-S compensated scheme is adopted. The battery charging voltage only depends on the output voltage of the DC power supply.

The capacitors are designed to compensate for inductive impedance corresponding to the sum of self and mutual inductance rather than the leakage (Lp-M and Ls-M). The reason is to pursue a compact, cost-effective, and light structure. Therefore, a compact and light structure can be realized if the system compensates (L+M) rather than (L-M).

In summary, S-SP and S-S compensation schemes are adopted in this work to achieve load-independent CC and CV charging, respectively. It is important for battery charging since the equivalent resistance of a battery load gradually increases during the charging process. Compared to the conventional LCL or LCC compensation schemes, the adopted compensation schemes can eliminate the usage of the compensated inductor. That means the size and weight of the receiver side can be greatly reduced, which is extremely suitable for EBs.

4.4 Experimental verification

4.4.1 Experimental setup

Experiments are carried out on a setup as shown in Fig. 4-14. The charging current and charging voltage references are 1.2 A and 24 V, respectively. The DC power supply is 24 V. The main parameters of the WPT system are provided in TABLE 4-2, measured by the LCR meter RS-Pro LCR 6300. The controller used for the inverter is Texas Instruments' digital signal processor (DSP) TMS320F28335. The battery load is emulated by a load bank LINGO LGFZ400DC. The voltage and current waveforms are captured by the oscilloscope Tektronix MDO3024.

TABLE 4-2. MAIN PARAMETERS OF THE WPT SYSTEM IN EXPERIMENT

Symbol	Value	Symbol	Value	Symbol	Value
C_1	4.38 nF	C_2	15.34 nF	C_K	69.7 nF
L_P	135.5 µH	L_S	27.4 µH	C_t	7.76 nF
R_P	0.29 Ω	R_S	0.07 Ω	M	9.56 µH
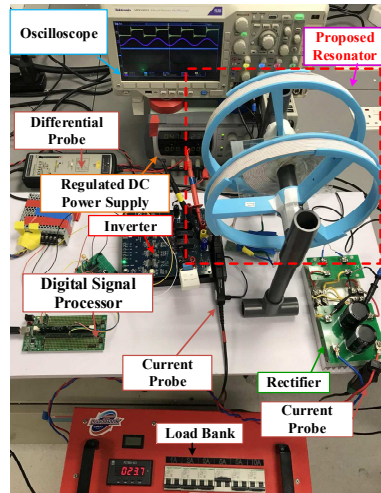
Fig. 4-14. Photograph of the experimental setup.

4.4.2 Load-independent Output validation

Initially, the switch S is turned ON, which means the compensated network of the WPT system is S-SP. The receiving coil is placed at p=50mm (in the middle of the Helmholtz coils, as shown in Fig. 4-2. The switching signals of the diagonal switches

are controlled to be complimentary in the DSP. The load resistance is changed from 18 Ω to 32.5 Ω, then to 40 Ω. The corresponding waveforms of the input voltage and current of the transmitter resonator (i.e., u_p and i_p), and the output charging voltage and current (i.e., U_B and I_B) of the load are shown in Fig. 4-15. The steady-state waveforms are enlarged. Apparently, the phase difference between u_p and i_p at steady states is almost unchanged during the entire process. The output charging currents are regulated at the reference current 1.2 A with less than 0.1% variations. The corresponding output charging voltages are 20V, 35.8V, and 44V, respectively. The results show that CC charging is achieved.
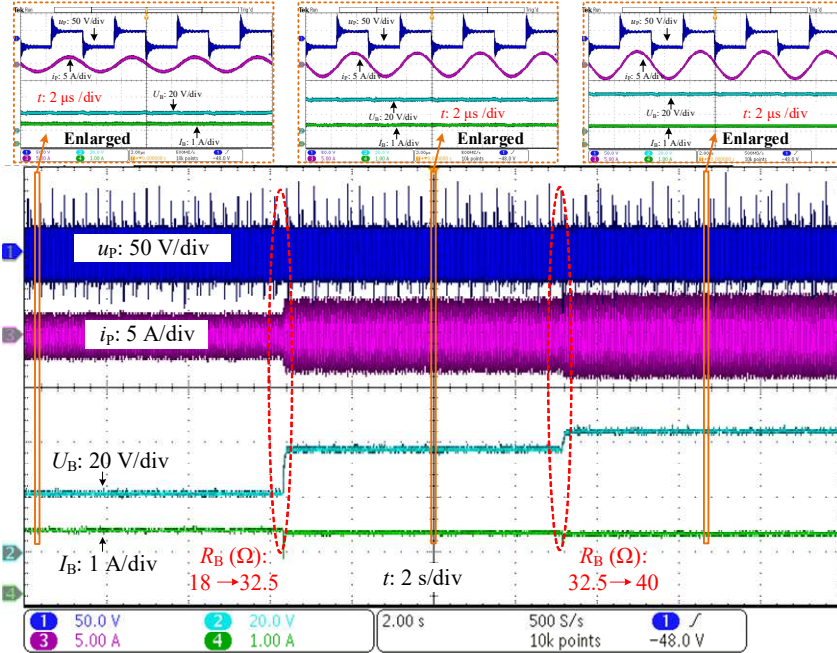
Fig. 4-15. Waveforms of u_p, i_p, U_B, and I_B of the WPT system in the CC charging mode when the load resistance changes from 18 Ω to 32.5 Ω, then to 40 Ω at p=50 mm.
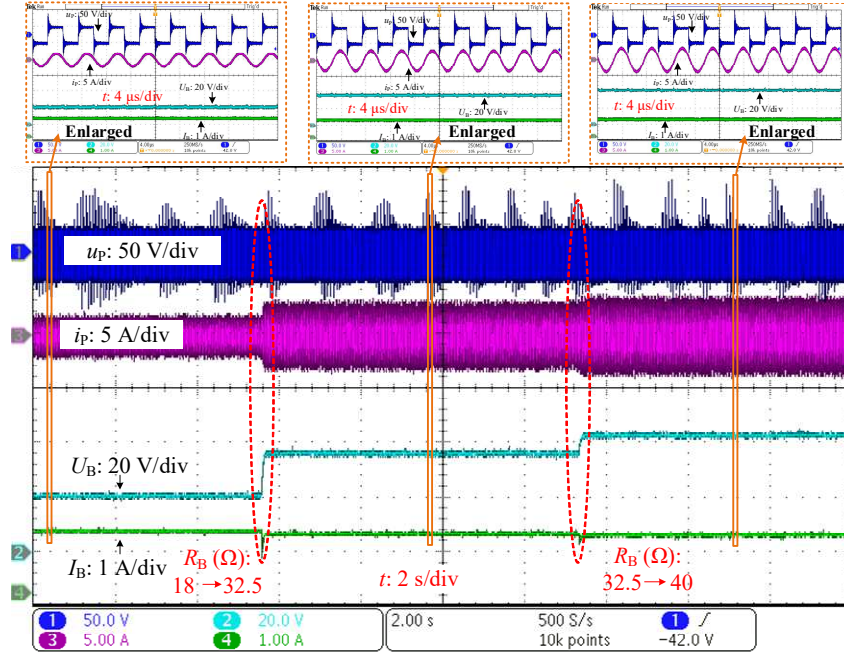
Fig. 4-16. Waveforms of u_p, i_p, U_B, and I_B of the WPT system in the CC charging mode when the load

resistance changes from 18 Ω to 32.5 Ω, then to 40 Ω at p=100 mm.

Then, the receiving coil is moved from p=50mm to p=100mm (close to one of the Helmholtz coils, as shown in Fig. 4-2), while the switch S is still turned ON to keep the S-SP compensation. The load resistance is also changed from 18 Ω to 32.5 Ω to 40 Ω. The corresponding waveforms of the input voltage and current of the transmitter resonator (i.e., u_p and i_p), and the output charging voltage and current (i.e., U_B and I_B) of the load are shown in Fig. 4-16. The steady-state output charging currents are well-regulated at the reference of 1.2 A. The corresponding output charging voltages are 20V, 35.8V, and 44V, respectively. The CC charging can also be achieved. Besides, both output current and voltage at p=100mm are identical to those at p=50mm, which means that the mutual inductance is invariant for the designed resonators.
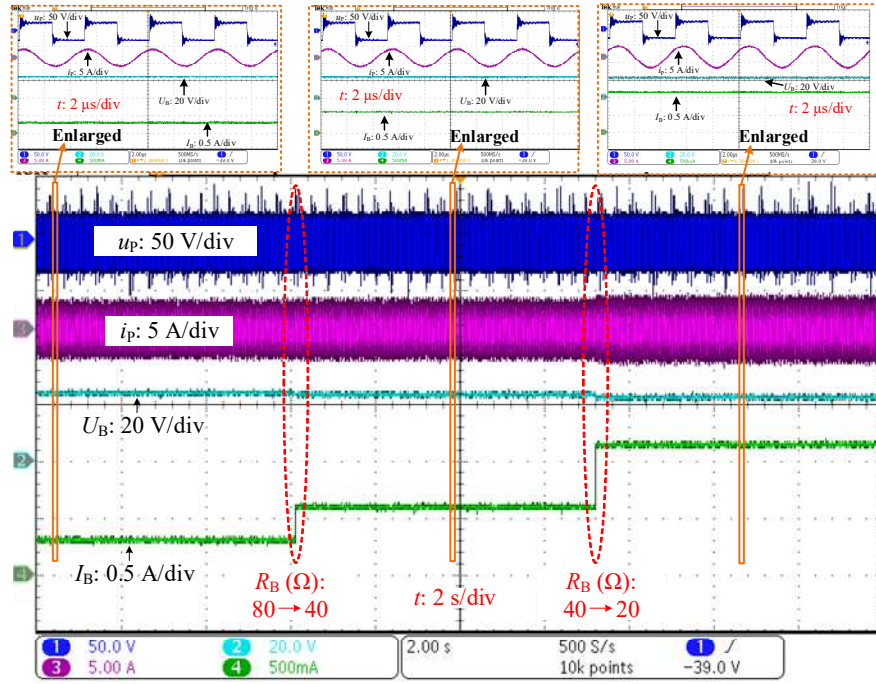
Fig. 4-17. Waveforms of u_p, i_p, U_B, and I_B of the WPT system in the CV charging mode when the load resistance changes from 80 Ω to 40 Ω to 20 Ω at p=50 mm.

Subsequently, the switch S is turned OFF, which means the compensated network of the WPT system is changed to be S-S. The receiving coil is placed at p=50mm (in the middle of the Helmholtz coils, as shown in Fig. 4-2). The load resistance is changed from 80 Ω to 40 Ω, then to 20 Ω. The corresponding waveforms of the input voltage and current of the transmitter resonator (i.e., u_p and i_p), and the output charging voltage and current (i.e., U_B and I_B) of the load are shown in Fig. 4-17. The output charging voltage is changed from 25.4 V to 25 V, then to 23.9 V at steady states, and the corresponding output charging current is changed from 0.32 A to 0.629 A, then to 1.21 A. The relative errors of the output charging voltage, as compared to the reference, are 5.83%, 4.17% and 0.42%, respectively. Because the deviations are less than 6%, the CV charging can be considered to be implemented.

Then, the receiving coil is moved from p=50mm to p=100mm (close to one of the Helmholtz coils, as shown in Fig. 4-2), while the switch S is kept turned OFF to maintain the S-S compensation. The load resistance is also changed from 80 Ω to 40 Ω, then to 20 Ω. The corresponding waveforms of the input voltage and current of the

transmitter resonator (i.e., u_p and i_p), and the output charging voltage and current (i.e., U_B and I_B) of the load are shown in Fig. 4-18. The output charging voltage is changed from 25.6V to 25.1V, then to 24.0V at steady states and the corresponding output charging current is changed from 0.322A to 0.632A to 1.22A. The relative errors of the output charging voltage, as compared to the reference, are 6.67%, 4.58% and 0%, respectively. It can be seen from the results that the CV charging can also be achieved. Furthermore, the output current and voltage at p=100mm are identical to those at p=50mm, which indicates that the mutual inductance is unchanged for the proposed resonators again.
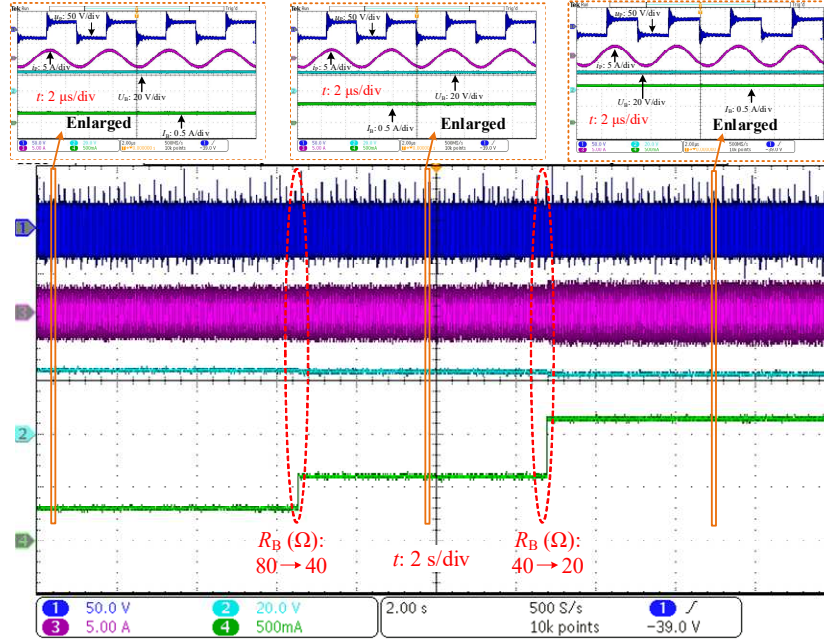
Fig. 4-18. Waveforms of u_p, i_p, U_B, and I_B of the WPT system in the CV charging mode when the load resistance changes from 80 Ω to 40 Ω to 20 Ω at p=100 mm.

4.4.3 Efficiency Analysis

To validate the transferability of the proposed resonator, the efficiency is coil-coil efficiency in this work, which can be seen in Fig. 4-19 and Fig. 4-20. The efficiency of two working stages, i.e., CV and CC, are all considered, which can be represented by η_{CV} and η_{CC}, respectively. Both can be calculated as

$$\eta = P_{\text{o}}/P_{\text{in}} \qquad\qquad (4.27)$$

where P_{in} is the input real power to the transmitter. And P_{o} is the output real power from the receiver. Both can be measured and calculated by the oscilloscope Tektronix MDO3024.

In terms of CV working stage, Fig. 4-19 illustrates the variation of the efficiency against different positions and output powers. It can be seen that the maximum efficiency can reach as high as 91.2%, which is acceptable for EB charging. With respect to CC working mode, Fig. 4-20 depicts the variation of the efficiency against positions and different load conditions. Furthermore, the maximum efficiency can arrive at 97.2% in the CC charging stage. The coil-coil efficiency arrives at its lowest transfer efficiency at 65 Ω, which may be caused by the current rise on the primary and the secondary sides at such a load condition. The efficiency drops according to the load condition. Due to the parasitic resistance of coils and the reflected impedance, the efficiency drops in this region. Future work will focus on the improvement of efficiency with a wide range of loads.

Remarkably, the efficiency variation is only 0.66% in CC mode and 0.65 % in CV mode, while moving from $p=0$ to $p=100$ mm. That means the proposed system can maintain a relatively stable charging efficiency at different charging positions, which is another superiority compared to conventional designs.

Waveforms of output current and voltage shown in these figures validate that $\frac{I_o}{I_{in}}$ meets the analysis mentioned in the above section. And, this proposed converter performs well to realize a stable output current.
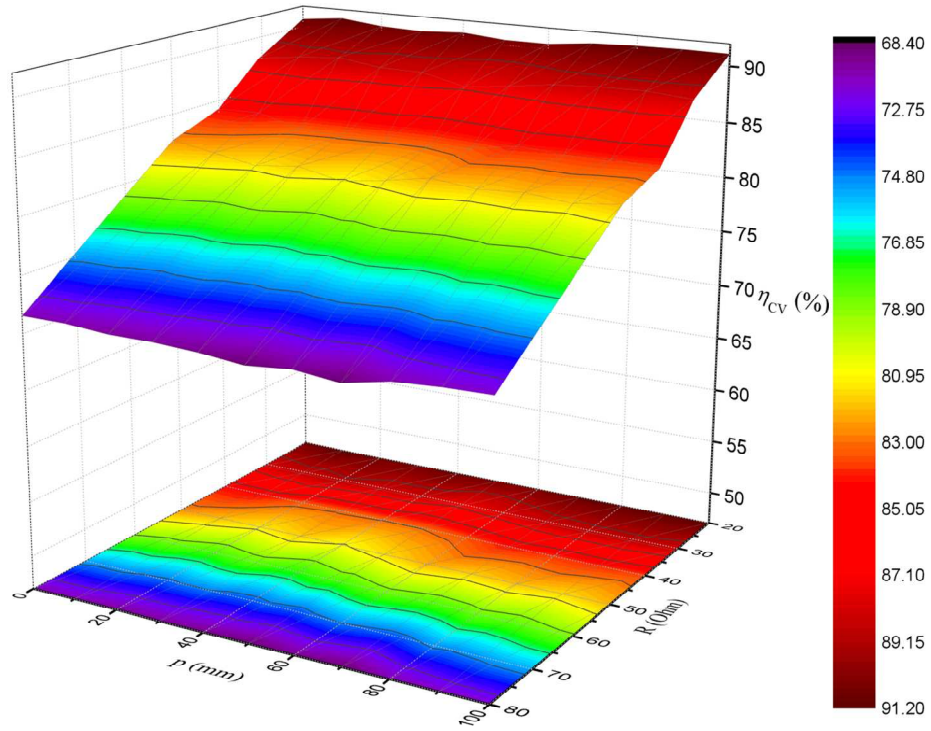
Fig. 4-19. Waveforms of measured efficiency at CV mode: Efficiency η_{CV} against different positions from p=0 to 100 mm when R_B is changed from 20 Ω to 80 Ω.
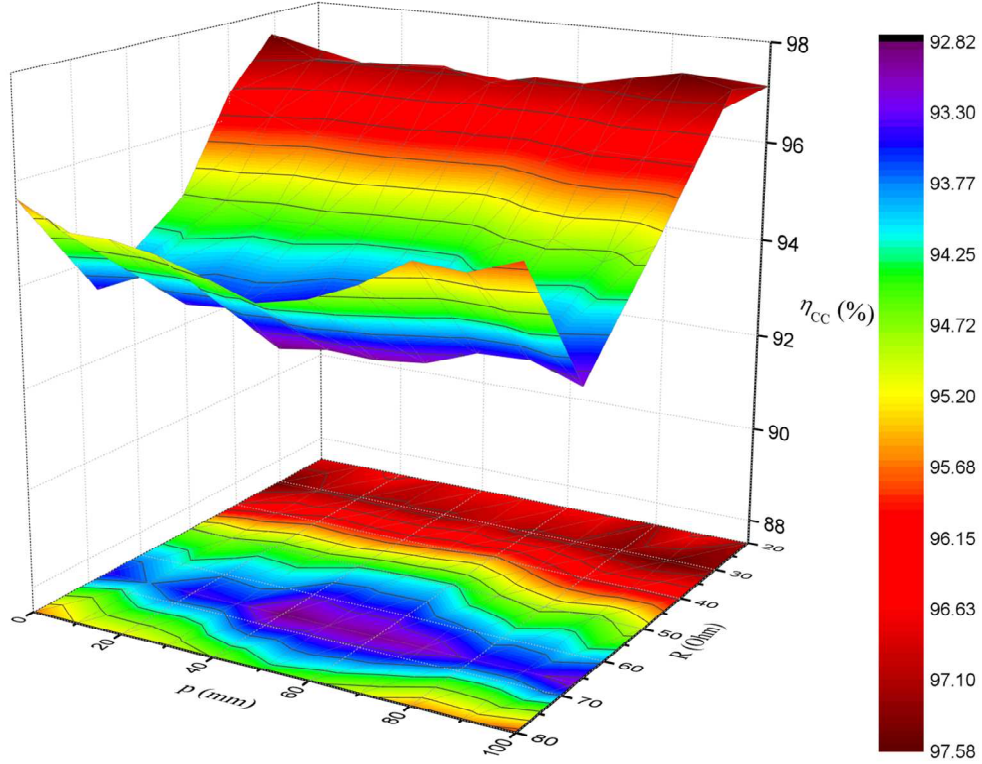
Fig. 4-20. Waveforms of measured efficiency at CC mode: Efficiency η_{CC} against with different positions from p=0 to 100 mm when R_B is changed from 20 Ω to 80 Ω.

4.5 Summary

In this chapter, a new resonator design method based on switched S-SP/S compensation scheme and Helmholtz transmitter coils is proposed for wireless power transfer (WPT) systems of Electric Bicycles (EBs). The newly designed resonators can inherently implement load-independent constant current (CC) and constant voltage (CV) charging for the battery loads while eliminating the drawbacks of conventional methods with variable mutual inductance, communication between the transmitter and receiver, additional user-end converters, complicated control strategies, and bulky LCL or LCC compensation networks. Overall, both simulation and experimental results manage to validate the merits of the proposed resonator design. Then maximum efficiency can reach 97.2% in the CC charging mode whereas 91.2% in the CV charging stage. And The efficiency can be regarded as stable when R_X is moving from $p=0$ to $p=100$ mm since the efficiency variation is only 0.66% in CC mode and 0.65% in CV mode. Only axial misalignment is experimentally tested in this chapter. The radial misalignment is not discussed in the experimental setup because the EB system is relatively easier to align in the radial direction. Chapters 2-4 discuss stationary wireless charging systems for several vehicular-based applications. To further utilize the advantages such as convenience and robustness, dynamic wireless power transfer (DWPT) is gaining more and more attention as an emerging technology for electric tram systems. Therefore, chapter 5 mainly focuses on the dynamic wireless power transfer system to charge electric trains (ETs).

Chapter 5

Improved Magnetic Coupler in Dynamic Wireless Power Transfer for Electric Trains

Electric transportation is considered an alternative to the existing internal combustion engine transportation to prevent environmental pollution. There are various types of electric transportation, such as electric cars, electric motorcycles, and electric bicycles (EBs). Above all, electric trains (ETs) are considered eco-friendly transportation in urban areas, especially for long-distance transportation. Most importantly, ETs emit less environmentally harmful compounds while using electricity as an energy source, but there are also some disadvantages. For example, the currently wired charger for ETs highly relies on the overhead line (OHL) systems. However, the OHL system is facing the shortcomings of high abrasion value, high failure rate, and large-scale maintenance. In other words, the maintenance cost of the electric supply line is relatively expensive, and the tunnel excavation for the electrical supply is required additional costs [148].

The high-power inductive power transfer technology delivers power wirelessly, which is a potential and new power supply mode for ET systems. In general, ETs can be charged wirelessly not only when they are parked (i.e., stationary WPT) but also when they are moving, i.e., dynamic wireless power transfer (DWPT) [24]. As DWPT can contribute to the extended driving range and reduced battery capacity, it has become a promising ET charger.

Unlike a conventional train, a wireless charging ET can be powered remotely from wireless charging infrastructure on the railway and store the remaining electricity in the battery, as demonstrated in Fig. 5-1. In addition, if a wireless charging ET is located on a railway with wireless charging infrastructure, electricity can be supplied either during a stop or in operation. This makes it possible to design an entire system with a smaller battery than a pure battery-powered ET. The wireless charging infrastructure is installed

in the railway to overcome the disadvantages caused by the electric supply line of the existing ETs [149].
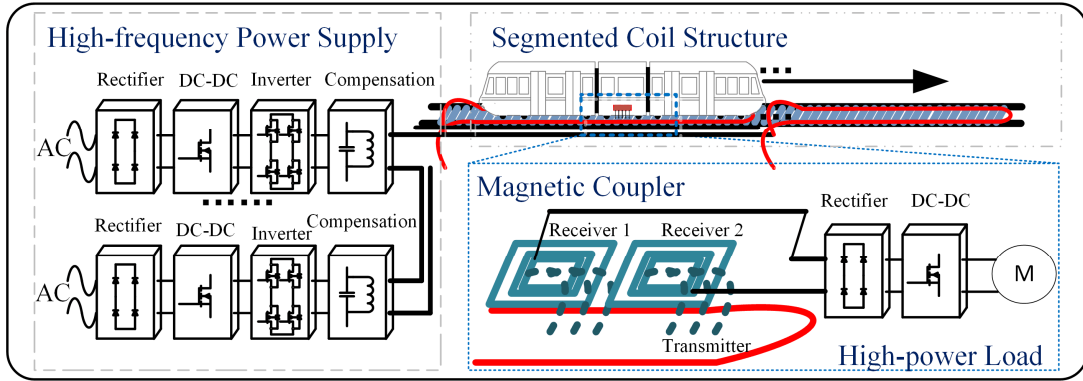
Fig. 5-1. A typical ET wireless charging system.

5.1 Review of Dynamic Wireless Power Transfer for ETs

According to the sizes of the transmitter coils and receiver coils, DWPT systems can be divided into two types: firstly, the long-track-transmitter type, where multiple receivers can be charged at the same time; secondly, the short-multiple transmitter type, where multiple transmitter coils are arranged in an array to charge the receiver. The advantage of the first type is the simple circuit structure [118]. Nevertheless, its disadvantages are also obvious, such as high electromagnetic interference (EMI) and low coupling coefficient between transmitter and receiver coils [150]. These lead to lower efficiency of the system. In contrast, for the second type, since the transmitters can be turned ON or OFF according to the receiver's position, lower EMI and higher efficiency can be achieved [151].

Generally, the following three aspects need to be considered to design a low EMI and highly efficient DWPT system with the segmented-multiple-transmitter type.

1) The self-couplings between the transmitters should be small so that the compensation circuit design can be straightforward.

2) The mutual coupling between the transmitter array and the receiver should be relatively stable for stable power output.

3) The position detection is needed to implement the segmented control to reduce EMI and power loss.

Self-coupling usually exists between adjacent transmitters. One solution is to utilize the refined magnetic coupler to reduce the unwanted self-coupling. In [93], unipolar and bipolar structures are used as adjacent transmitters, making the self-couplings between the transmitters naturally small. In [152], the self-couplings between transmitters are mitigated by using refined inductor-capacitor–capacitor (*LCC*) compensators. Furthermore, self-coupling usually appears when the two transmitters are close. Therefore, another way to reduce the self-coupling is to put the transmitters far away from each other. For instance, self-couplings can be reduced effectively when the distance between the adjacent transmitters is about 30% of the transmitter length [153]. However, the large distance between the adjacent transmitters raises another issue, i.e., the power pulsation phenomenon caused by the fluctuating mutual coupling between the transmitter array and the receiver.

For the second consideration in short-multiple-transmitter type DWPT systems, to keep the mutual coupling between the transmitter array and the receiver stable, Lu et al. [23] optimize the size of the receiver coil. By ignoring the edge effects, during the movement, the variation of the coupling coefficient is only ± 2.1%, and the power pulsation can be maintained within ± 2.9%. Nevertheless, self-couplings between the transmitters still exist, which poses challenges in designing the compensation circuit. Li et al. Ref [93] propose a new magnetic coupler to reduce the mutual coupling variation. Unipolar and bipolar coils are placed alternately to form the transmitter array, whereas unipolar and bipolar coils are overlapped and connected in series on the receiver side. With this coupling structure, the mutual inductance fluctuation is within ± 2% during the movement, and the power pulsation can also be achieved with only ± 2% fluctuation. However, the position detection method is not illustrated in detail, which is crucial to implementing the automatic segmented control.

Regarding position detection, conventionally optic or ultrasonic sensors can be employed to detect the receiver's position. These sensors need to be installed in specific

locations, which may be affected by the surrounding environment. Recently, some research works have demonstrated that the receiver's position can be estimated by the mutual inductance, leading to effective position detection. However, these works mainly focus on stationary WPT systems without further considering DWPT applications. Hence, a new coupling structure is introduced to fill the aforementioned technical gaps. Bipolar coils are used to mitigate the self-couplings between the adjacent unipolar transmitter coils. Since bipolar coils and unipolar coils are naturally decoupled, the stable mutual coupling between the transmitter array and the receiver, and hence stable power output, can be achieved. Furthermore, a position detection method by monitoring the primary current is developed to implement the automatic segmented control.

5.2 Magnetic Coupler for ETs

Electric trains (ETs) are promising due to their eco-friendly features like saving fossil fuels and reducing emissions. Wireless power transfer (WPT) is an attractive method thanks to its incredible merits. Dynamic wireless power transfer (DWPT) can charge ETs either in parking or running. The multiple-individual-transmitter structure is presented in this chapter to charge ET dynamically. It is also called segmented DWPT because multiple-segmented transmitters are placed one by one to build a charging route. One fundamental function is that transmitters can be switched on or off according to the position of the receiver [154]. Therefore, higher efficiency and lower exposed EMF can be achieved compared with the long-track loop structure [155], [156].

Impressively, Li *et al*. proposed a segmented DWPT system. It reduces the unwanted couplings between adjacent transmitters and ensures a stable mutual inductance between transmitters and the receiver [93]. The coupling structure is made up of LITZ-wire coils and ferrite plates. A related winding technique to reduce the conductor loss is reported to further reduce the loss. The technique is to provide a winding method for any shape of the ferrite core. The method for turn pitch and stranded winding structure can be designed using this method and further reduce the loss.

Nevertheless, previous segmented DWPT studies mainly focus on using one inverter to drive several transmitters. In terms of high-power applications, using one inverter to drive is very difficult because of the high current or voltage stress on semiconductor components. Moreover, the switching sequence still needs investigating. A well-designed switching sequence ensures a balance between minimizing energized transmitters while mitigating the total coupling variation. Hence, this thesis presents one improved and integrated design to resolve the abovementioned problems. The key contributions are summarized as follows:

1) A modified switching sequence: The switching means turning on/off coils. The proposed switching sequence seeks to make a balance between minimizing energized transmitters and reducing the magnetic coupling variation. Only three consecutive transmitters are energized according to the receiver position, which can ensure stable power transmission for EVs. In this part, Q-DD-Q is used as an elementary energized group. Specifically, Q-DD-Q means a group of three consecutive coils, i.e., a Q-shaped coil, a DD-shaped coil, and a Q-shaped coil again.

2) The integrated design for high-power transfer: The magnetic coupler is refined for high-power transfer and stable operation through the ANSYS Maxwell. The transmitter and receiver coils are all designed as 500 mm × 500 mm, avoiding the power-null phenomenon. Compared with using only one inverter, parallel inverters can reduce the current stress of semiconductor devices like MOSFET. Thus, the presented method is suitable for high-power applications.

The experimental results show that this research can realize the load-independent CV charging, which is vital to charge a typical battery because its equivalent resistance is changed during the entire charging process. Moreover, the overall dynamic wireless charging efficiency (dc-dc efficiency) can reach about 85% from 100 Ω to 200 Ω loads. The maximum output power is 2.5 kW at a 100 Ω load value.

5.2.1 Magnetic Coupler Design

In this part, the transmitter and receiver coils are all designed as 500 mm × 500 mm. The magnetic coupling is usually dependent on the coil size. The size of the receiver is also limited by the available installation space at the bottom of the vehicle.

Specifically, Q-shaped and DD-shaped coils are utilized as consecutive transmitter coils to reduce unwanted cross-couplings. The reason is illustrated in Fig. 5-2. It shows that the amount of the magnetic flux generated by the DD coil flowing into the Q-shaped coil equals that flowing out of it and vice versa. Thus, the mutual inductance between the DD and the Q-shaped coil can be negligible due to the natural decoupling phenomenon between these two coils [93].
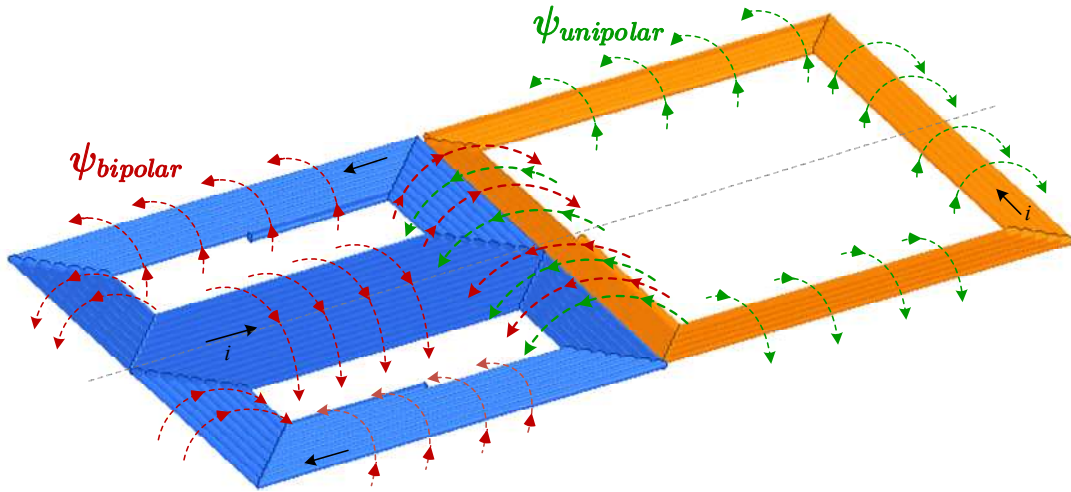
Fig. 5-2. Flux diagram of the Q-shaped coil and the DD coil.

Fig. 5-3 demonstrates the overview diagram of the entire system. Two coil types, i.e., unipolar (Q-shaped) and bipolar (DD), are arranged to form a charging route. The mutual inductance between two non-adjacent, i.e., the identical shape transmitter coils, can also be ignorable. The reason is that this magnetic coupling is already small enough due to the non-adjacent distance. Therefore, compensation networks can be designed straightforwardly.

$$\dot{U}_{ind} = j\omega M_{ti}\dot{I}_P \;\; (i=1 \; or \; 2)$$
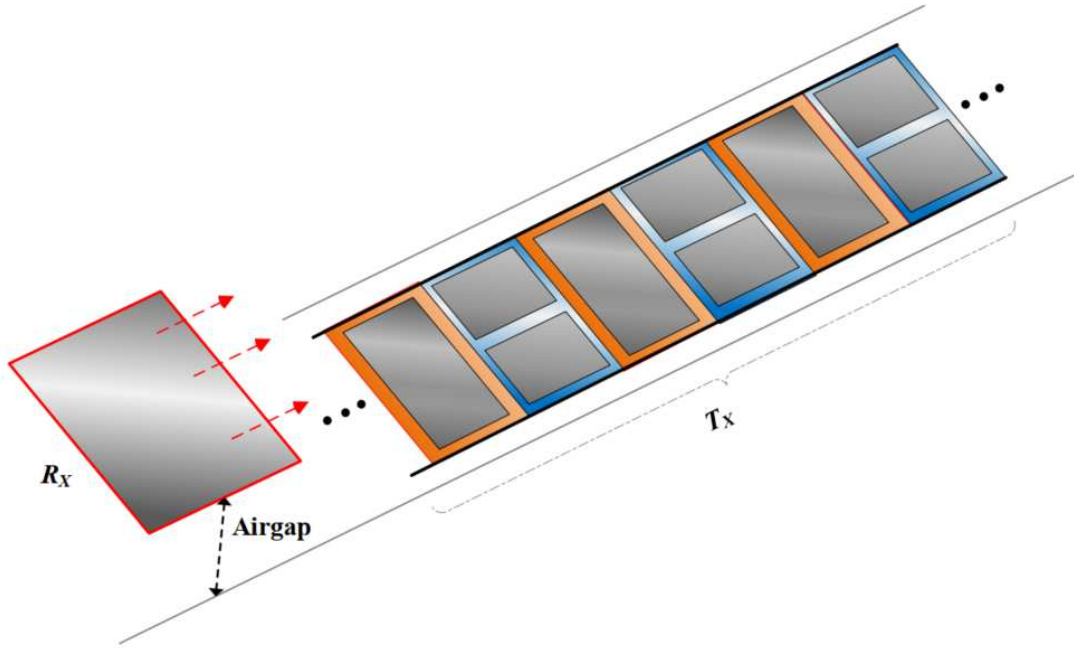
Fig. 5-3. The overview diagram of the whole system.

The detailed size of the transmitter array is demonstrated in Fig. 5-4. Because of the test size limitation, only five transmitters and one receiver are considered in this work.
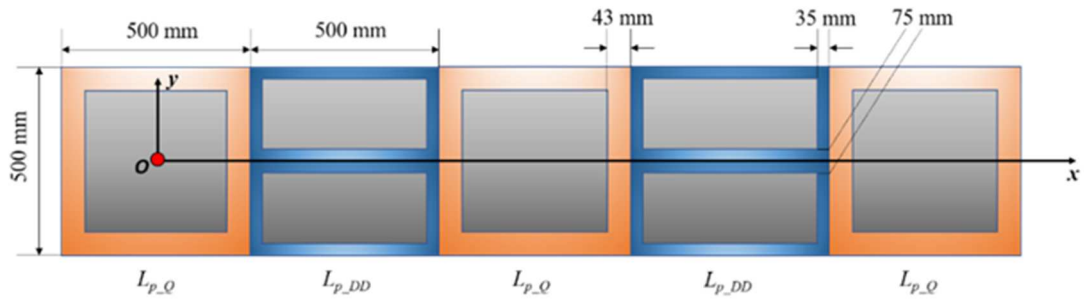
Fig. 5-4. The detailed diagram of the transmitter array.

The receiver coil is designed with the same size as the transmitting coil, as illustrated in Fig. 5-5. Both transmitters and the receiver consist of LITZ-wire coils and ferrite plates. Furthermore, ferrite plates are the same size as the coil pads to improve the magnetic field and reduce flux leakage. Each ferrite core thickness is 10 mm, and the raw material is PC40 from TDK. Specifically, the ferrite material, which has a

relatively low eddy current loss and a high relative permeability (e.g., TDK PC 40), can be used to guide the magnetic flux. This thesis adopts the 1000-strand LITZ-wire with a 6.5 mm wire diameter to manufacture inductors and the magnetic coupler. The advantage of multi-stranded LITZ-wire is to reduce losses from the skin effect and proximity effect.
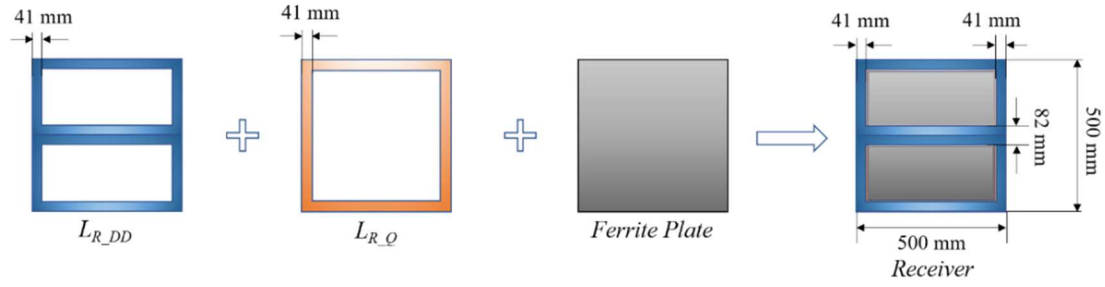
Fig. 5-5. The exploded diagram of the receiver with detailed size information.

Besides, the coil connection method still needs clarifying since it plays an essential role in stabilizing mutual inductance. Specifically, there are two terminals, i.e., A and B, for each coil, as illustrated in Fig. 5-6. The exact coil connection method from this work is demonstrated in TABLE 5-1.
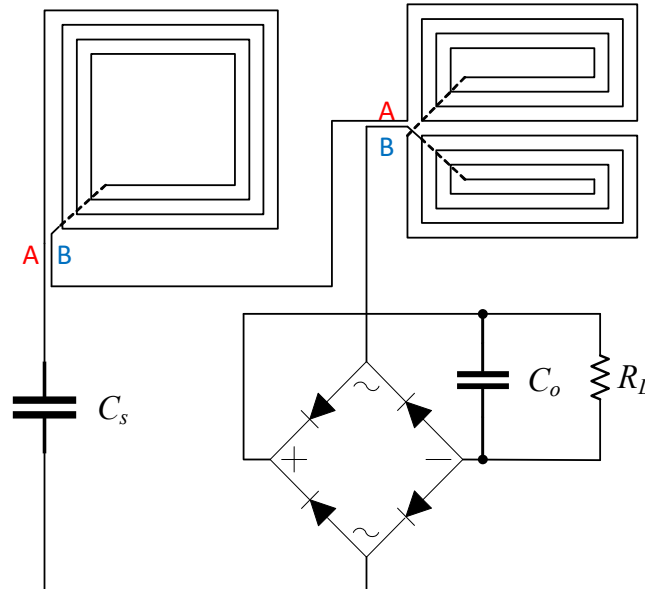
Fig. 5-6. The diagram of the R_X circuit with connection terminals.

TABLE 5-1. THE DETAILED CONNECTION METHOD

Terminal	Transmitter Side	Receiver Side
Q-shaped Coil Terminal A (Q_A)	Input	Connect to rectifier
Q-shaped Coil Terminal B (Q_B)	Output	Connect to DD_A in series
DD-shaped Coil Terminal A (DD_A)	Output	Connect to Q_B in series
DD-shaped Coil Terminal B (DD_B)	Input	Connect to rectifier

5.2.2 Circuit Analysis

As depicted in Fig. 5-7, the entire circuit system can be divided into two parts, i.e., the primary and secondary sides. The primary side consists of a high-power DC source, high-frequency inverters, and the T_X. The receiver part is composed of the R_X, a rectifier, and the load part. In this part, five transmitters and one receiver are used for demonstration. Each transmitter coil works with the LCC unit that is made up of additional inductors L_{ai}, additional capacitors C_{ai} and primary capacitors C_{pi} ($i = 1,2,...,5$). CV can be gained directly at the load side. The operating frequency is 85 kHz for industrial consideration, subjecting to SAE J2954. The angular frequency should satisfy:

$$\omega = 2\pi f = \frac{1}{\sqrt{L_S C_S}} = \frac{1}{\sqrt{L_{ai} C_{ai}}} = \frac{1}{\sqrt{(L_{Pi} - L_{ai}) C_{Pi}}} \quad (i = 1,2,...,5) \tag{5.28}$$

Three inverters are used to power the transmitters. For validation, due to the parallel connection, the phasor relationship of output voltage from the inverter can be expressed as

$$\dot{U}_{12} = \dot{U}_3 = \dot{U}_{45} = \frac{2\sqrt{2}V_{DC}}{\pi} \angle 0° \tag{5.29}$$

According to Kirchhoff's current law (KCL), the current relationships can be gained as

$$\begin{cases} \dot{I}_A = \dot{I}_1 + \dot{I}_2 \\ \dot{I}_B = \dot{I}_4 + \dot{I}_5 \end{cases} \tag{5.30}$$

Through manufacturing L_{ai} delicately, the following equation can be obtained as

$$L_a = L_{a1} = L_{a2} = L_{a3} = L_{a4} = L_{a5} \tag{5.31}$$
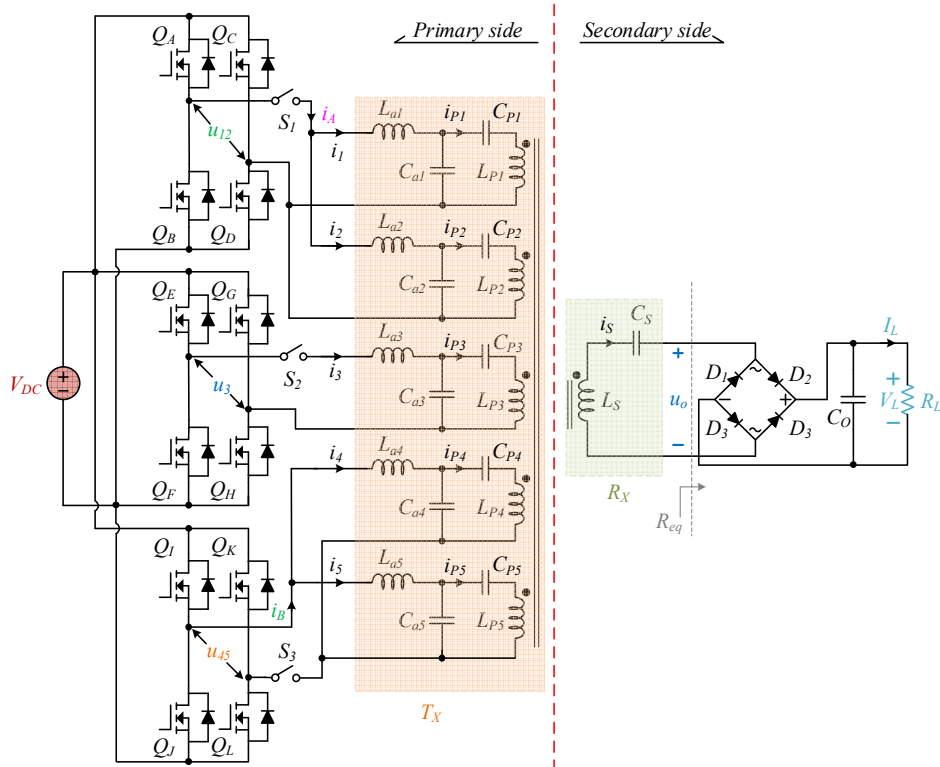
Fig. 5-7. The entire circuit diagram.

Similarly, it is easy to attain the relationships for the transmitting side by using Kirchhoff's Law

$$\begin{cases} \dot{I}_{P1} = \dfrac{\dot{U}_{12}}{j\omega L_{a1}} = \dfrac{2\sqrt{2}V_{DC}}{\pi\omega L_{a1}} \angle -90^\circ \\[3mm] \dot{I}_{P2} = \dfrac{\dot{U}_{12}}{j\omega L_{a2}} = \dfrac{2\sqrt{2}V_{DC}}{\pi\omega L_{a2}} \angle -90^\circ \\[3mm] \dot{I}_{P3} = \dfrac{\dot{U}_{3}}{j\omega L_{a3}} = \dfrac{2\sqrt{2}V_{DC}}{\pi\omega L_{a3}} \angle -90^\circ \\[3mm] \dot{I}_{P4} = \dfrac{\dot{U}_{45}}{j\omega L_{a4}} = \dfrac{2\sqrt{2}V_{DC}}{\pi\omega L_{a4}} \angle -90^\circ \\[3mm] \dot{I}_{P5} = \dfrac{\dot{U}_{45}}{j\omega L_{a5}} = \dfrac{2\sqrt{2}V_{DC}}{\pi\omega L_{a5}} \angle -90^\circ \end{cases} \tag{5.32}$$

Substituting (5.29) and (5.31) into (5.32), the relationship can be rewritten as

$$I_P = I_{Pi} = \frac{2\sqrt{2}V_{DC}}{\pi\omega L_a} \angle -90° \ (i = 1, 2, 3, 4, 5) \tag{5.33}$$

where indicates that all the currents flowing through each transmitter coil can be designed as the same value.
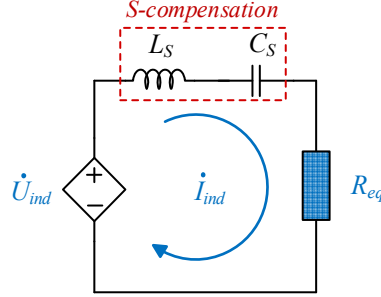
Fig. 5-8. The equivalent circuit at the secondary side with the S-compensation network.

Furthermore, Fig. 5-8 depicts the equivalent circuit on the secondary side. And the total induced voltage can be gained as

$$\dot{U}_{ind} = j\omega M_{ti}\dot{I}_P \ (i = 1 \ or \ 2) \tag{5.34}$$

where M_{ti} is the total mutual inductance between i group of transmitters and the R_X. M_{ti} is different according to different switching sequences, which highly depends on the number of energized coils. They can be expressed as

$$\begin{cases} M_{t1} = M_1 + M_2 + M_3 \\ M_{t2} = M_3 + M_4 + M_5 \\ M_{t3} = M_1 + M_2 + M_3 + M_4 + M_5 \end{cases} \tag{5.35}$$

where M_j (j=1,2,3,4,5) means the mutual inductance between the jth transmitter and the receiver.

For stable switching operation, the average value of M_{t1} should be equal to M_{t2} with slight variation while R_X is moving. M_{t3} is the total mutual inductance between R_X and all T_X coils, i.e., L_{P1} to L_{P5}. In Fig. 5-8, $U_{ind} = U_o$ because of the S-compensation network at the R_X side. As for the relationship between the input and output of the rectifier, it can be written as

$$\begin{cases} U_o = \dfrac{2\sqrt{2}}{\pi} V_L \\[2mm] I_S = \dfrac{\pi}{2\sqrt{2}} I_L \\[2mm] R_{eq} = \dfrac{8}{\pi^2} R_L \end{cases} \tag{5.36}$$

Substituting (5.33) and (5.34) into (5.36), the load-independent constant output voltage can be derived as

$$V_L = \frac{M_t V_{DC}}{L_a} \tag{5.37}$$

5.2.3 Switching Sequence

Generally, only three transmitters need energizing in each segmented group. As illustrated in Fig. 5-9, the purple dotted line means the switching point line. In other words, the switching points include the -25 cm, 75 cm and 175 cm points shown in Fig. 5-10. At each switching point, an ultrasonic sensor is installed to conduct the switch operation as illustrated in Fig. 5-9. Due to the test size limitation, only the 75 cm switching point (*P2*) is demonstrated in this work.

Silicon carbide MOSFET CCS050M12CM2 is adopted in the inverters, which ensures high-power and high-efficiency operation. For the safety concern, i.e., the current stress of the semiconductor device like MOSFET, one inverter can drive at most two transmitter coils due to the maximum current stress (61 A) of MOSFET CCS050M12CM2in the experimental prototype. In this chapter, three coils are chosen as a group either Q-DD-Q or DD-Q-DD. The reason is that these three coils can make stable magnetic couplings from the transmitter to the receiver during the moving process. The sequence of Q-DD-Q is chosen as one segmented energizing group. The Q-DD-Q means an energized group of three consecutive coils, i.e., a Q-shaped coil, a DD-shaped coil, and a Q-shaped coil again.

Furthermore, switching occurs when the right edge of the receiver directly faces the dotted line, as shown in Fig. 5-9. The switching is accomplished by the ultrasonic

sensor to test the position. There are three sensors installed at the positions of three purple dotted lines, i.e., ultrasonic sensors (US#1, US#2, and US#3). In other words, switching happens where the receiver directly faces the Q coil transmitter. The periods of starting and ending are not considered in this thesis, and the main concern is the period of stable operation.

Specifically, two-segmented energizing groups (e.g., *G1* and *G2*) are built and demonstrated in this experimental test. *G0* and other energized groups are neglected due to the size limitation of the test site. To be specific, from *P1* to *P2*, *G1* is conducted. From *P2* to *P3*, *G2* is conducted, etc. The position detection is realized by the ultrasonic detection module. *G*1 works when the receiver arrives at *P*1 while *G*1 stops when the receiver reaches *P*2. *G*2 operates when the receiver reaches *P*2 while stopping when the receiver arrives at *P*3.
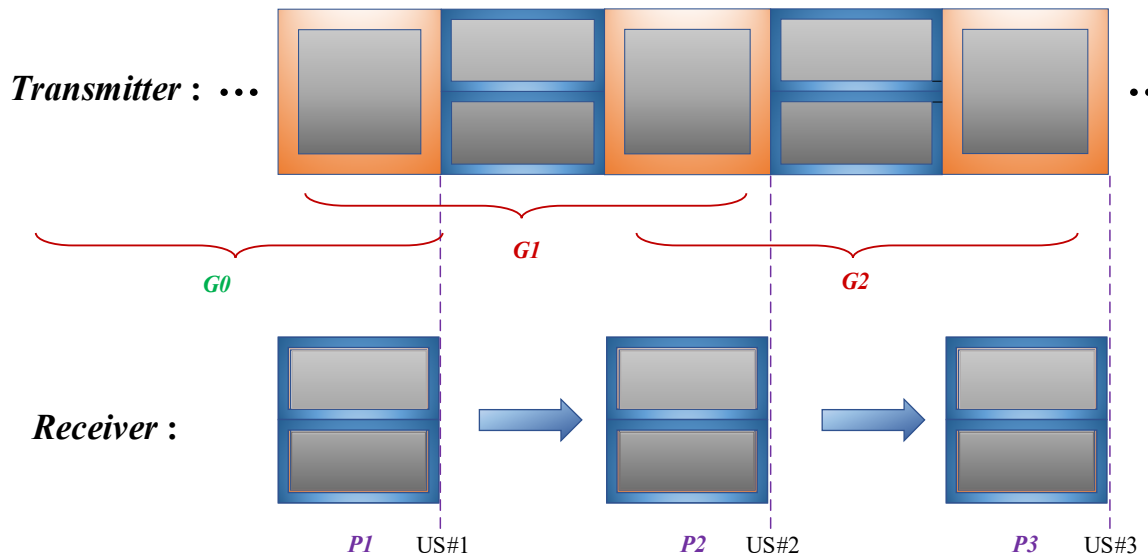
Fig. 5-9. The diagram of the proposed switching sequence.

This thesis only considers the stable running period without the start and the end. The stable charging zone is from 0 cm to 162.5 cm, as illustrated in Fig. 5-10.
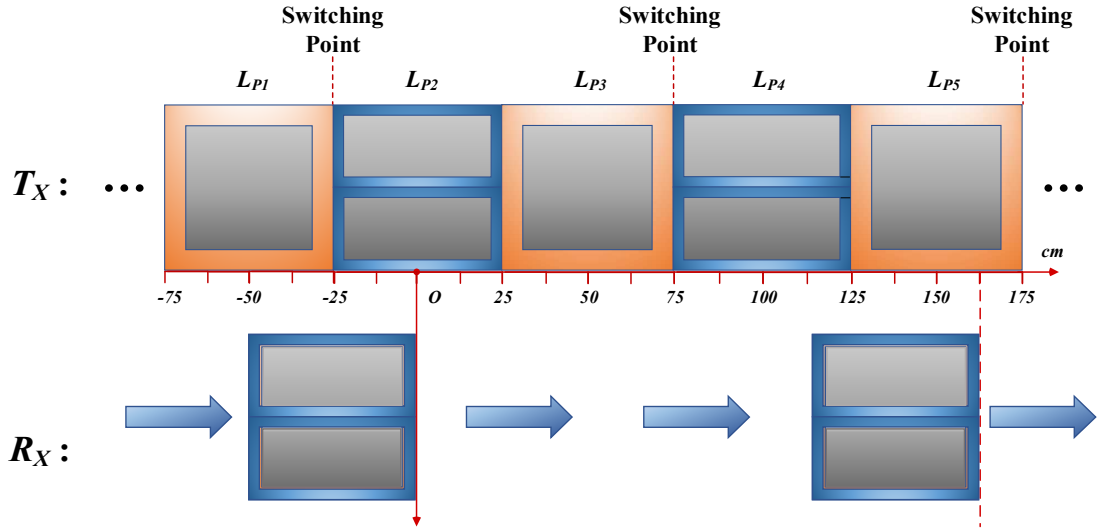
Fig. 5-10. The stable charging zone.

The mutual inductance between the T_X and R_X can be concluded in Fig. 5-11. Specifically, M_{t1} is the total mutual inductance between the R_X and *G1* including L_{P1}, L_{P2} and L_{P3}, according to (5.8) M_{t2} is the total mutual inductance between the R_X and *G2* including L_{P3}, L_{P4} and L_{P5}. And M_{t3} is the total mutual inductance between R_X and all T_X coils from L_{P1} to L_{P5}.
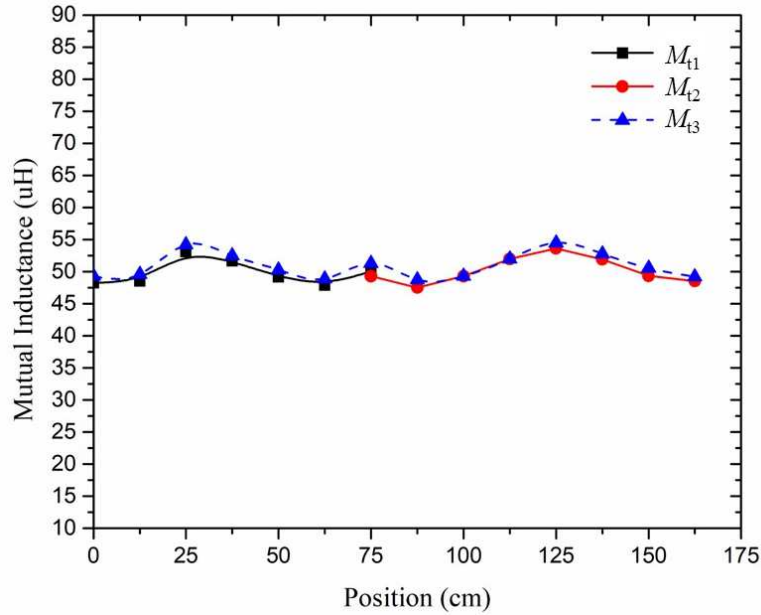
Fig. 5-11. The measured mutual inductance under different positions.

This picture also illustrates that the magnetic coupling contribution from L_{P1} and L_{P2} is small during the *P2* to *P3* process. As demonstrated in Fig. 5-11, one Q-DD-Q

sequence after another can maintain the relatively stable mutual inductance, i.e., M_{t1} and M_{t2}. Hence, the three-consecutive-coil group Q-DD-Q can be selected as one segmented energizing group.

The measured value of total mutual inductance defined by (5.8) is changed from 47.5 µH to 53.6 µH, measured by the RS-PRO LCR 6300. The minimum value happens at 87.5 cm, whereas the peak value happens at 125 cm position. The average value of the total mutual inductance, avg{M_{t3}}, is approximately 50 µH. The maximum value of the ripple of the total mutual inductance Mt3 is defined as λ_{max}, which can be expressed as

$$\lambda_{\max} = \max\left\{\left|\frac{\max\{M_{t3}\}-\text{avg}\{M_{t3}\}}{\text{avg}\{M_{t3}\}}\right|, \left|\frac{\min\{M_{t3}\}-\text{avg}\{M_{t3}\}}{\text{avg}\{M_{t3}\}}\right|\right\} \quad (5.38)$$

where max{M_{t3}} and min{M_{t3}}are the maximum and the minimum value of M_{t3}, respectively. Thus, λ_{max} is 7.2 % in this thesis. Future work will consider the speed and timing among different components.

5.3 Experimental Validation

5.3.1 Experimental Setup

As illustrated in Fig. 5-13, a laboratory prototype of the proposed segmented DWPT system is built. This prototype consists of five transmitters and one receiver. The moving speed is assumed to be slow enough so that its effect on the segmented switch can be neglected [93]. One DC power supply is adopted to power these three parallel inverters. Through the well-designed LCC units shown in Fig. 5-14, the load-independent CV can be achieved at the load side. The capacitors are EACO SCM2000, and their parameters are described in TABLE 5-2. The step-by-step selection procedures are shown in Fig. 5-12.

TABLE 5-2. DESCRIPTION OF EACO SCM2000

Parameters	Description	Parameters	Description
Standard	IEC 61071	Temperature	-40 ~ 105 °C
Structure	Metallized polypropylene film	Thermal resistance	9.7 K/W
Rated Voltage	2000 VAC	Peak Current	269 A
Peak Voltage	2828 V	Effective Current	I_{rms} = 30A @100kHz 45°C

```
                        ┌─────────┐
                        │  Start  │
                        └─────────┘
                             │
    ┌────────────────────────────────────────────────────────┐
    │ Given the inductance of transmitters and the desired    │
    │ DC input and DC output values.                          │
    └────────────────────────────────────────────────────────┘
                             │
         ┌────────────────────────────────────────┐
         │ Select the maximum measured inductance  │
         │ among them                              │
         └────────────────────────────────────────┘
                             │
      ┌──────────────────────────────────────────────┐
      │ Calculate the value of capacitance according  │
      │ to euqation (5.1)                             │
      └──────────────────────────────────────────────┘
                             │
    ┌──────────────────────────────────────────────────┐
    │ Calculate the current and voltage on the          │
    │ capacitance, I_C and U_C                          │
    └──────────────────────────────────────────────────┘
                             │
     ┌───────────────────────────────────────────────┐
     │ Select capacitors rated values according to    │◄──┐
     │ I_C and U_C                                     │   │
     └───────────────────────────────────────────────┘   │
                             │                            │
   ┌─────────────────────────────────────────────────┐    │
   │ Design the connection method of capacitors       │    │
   │ (series or parallel) to reduce the current and   │    │
   │ voltage stress on each capacitor                 │    │
   └─────────────────────────────────────────────────┘    │
                             │                            │
                        ◇◇◇◇◇◇◇◇◇◇              No        │
                       Meet the      ──────────────────────┘
                       requirements?
                        ◇◇◇◇◇◇◇◇◇◇
                             │ Yes
                        ┌─────────┐
                        │   End   │
                        └─────────┘
```

Fig. 5-12. The capacitor selection procedure.
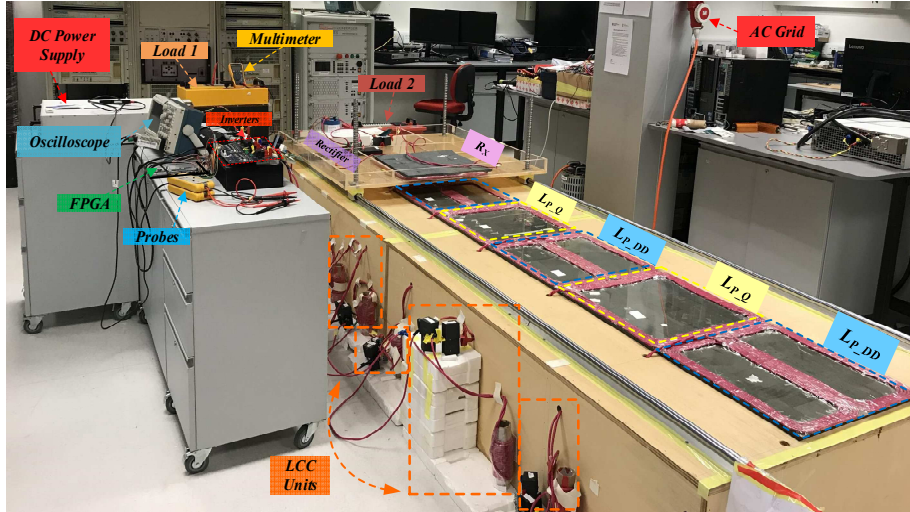
Fig. 5-13. The experimental prototype.
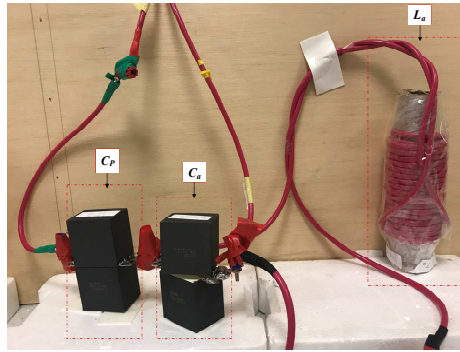
Fig. 5-14. The picture of one typical LCC unit.
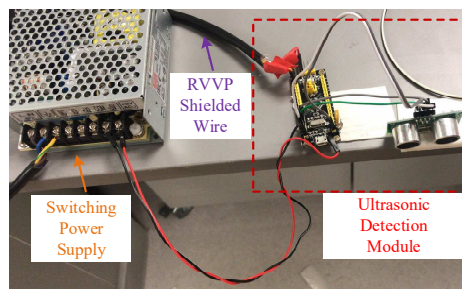
Fig. 5-15. The diagram of the ultrasonic detection part.

Specifically, two-segmented energizing groups (e.g., *G1* and *G2*) are built and demonstrated in this experimental test. *G0* and other energized groups are neglected due to the size limitation

Segmented wireless charging can be achieved according to the positions of the

receiver. The ultrasonic module HY-SRF05 can realize position detection with shielded wire, as shown in Fig. 5-15, which ensures the signal data cannot be interfered with by the high-frequency magnetic field. The detailed parameters of the entire experimental prototype are listed in TABLE 5-3.

As illustrated in Fig. 5-15, the constant voltage can be maintained at around 500 V through the whole operation period with slight variation. Fig. 5-16 describes the key waveforms before and after the switching point, respectively. Before the switching point, U_{12} is turned on whereas U_{45} is turned off. After the switching point, U_{45} is switched on whereas U_{12} is turned off. U_3 is constantly turned on during the whole period because both *G1* and *G2* need U_3 in this experimental validation.

The current distortion can be seen in Fig. 5-17 and Fig. 5-18, which is the problem that will be addressed in future work. The possible causes may be the slight change of resonant state caused by the secondary side while in motion. The ferrite core on the receiver side may affect the inductance of transmitters. The resonant state tends to be changed if the self-inductances are changed because the resonant frequency is shifted from the original operating point. Overall, load-independent 500 V output voltage is achieved with oscillation ripples less than 25 V (5% of the nominal voltage), ensuring stable output on the receiver side.

The detailed design procedure shown in Fig. 5-12 explains the design process of capacitors. The inductance value is firstly confirmed by magnetic design from ANSYS Maxwell. According to equation (5.1), the value of the capacitance can be further confirmed. The maximum current in each transmitter coil is designed originally at 18.5 A. Subsequently, the maximum voltage of the LCC topology should happen at the L_{P4} (119.41 µH), which can be expressed as

$$U_C = I_C \cdot \omega L_{P4} = 1180V \tag{5.39}$$

Therefore, the rated voltage is chosen as 2000 VAC according to the experience (2 times of U_C), as shown in Table 5.2.

TABLE 5-3. EXPERIMENTAL PARAMETERS

Symbol	Value	Symbol	Value	Symbol	Value	Symbol	Value
L_{P1}	94.83 μH	C_{P1}	51.94 nF	L_{a1}	27.33 μH	C_{a1}	128.13 nF
L_{P2}	111.83 μH	C_{P2}	41.49 nF	L_{a2}	27.46 μH	C_{a2}	123.68 nF
L_{P3}	95.68 μH	C_{P3}	50.89 nF	L_{a3}	27.21 μH	C_{a3}	125.85 nF
L_{P4}	119.41 μH	C_{P4}	42.31 nF	L_{a4}	27.39 μH	C_{a4}	129.12 nF
L_{P5}	95.47 μH	C_{P5}	52.31 nF	L_{a5}	27.41 μH	C_{a5}	127.93 nF
L_S	263.53 μH	C_S	13.41 nF	f	85 kHz	*Airgap*	80 mm
N_{PQ}	7 turns	N_{PDD}	6 turns	N_{SQ}	7 turns	N_{SDD}	7 turns
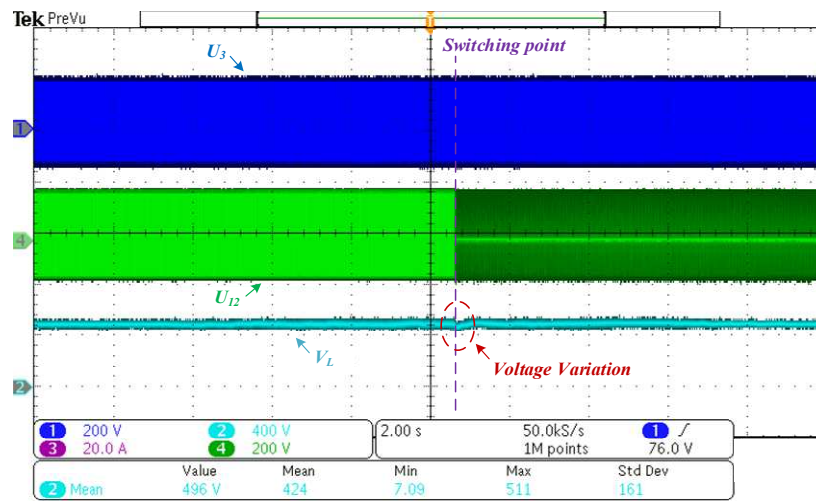
Fig. 5-16. The dynamic response at the switching point.
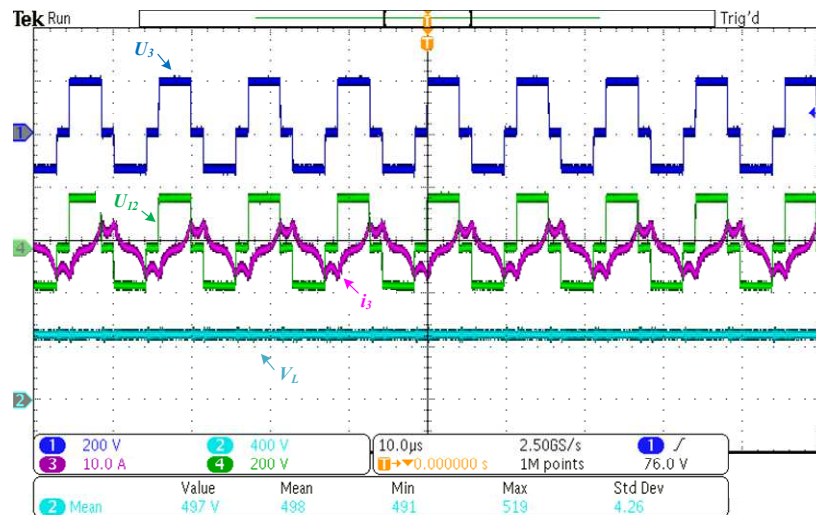
Fig. 5-17. The key waveform before the switching point.
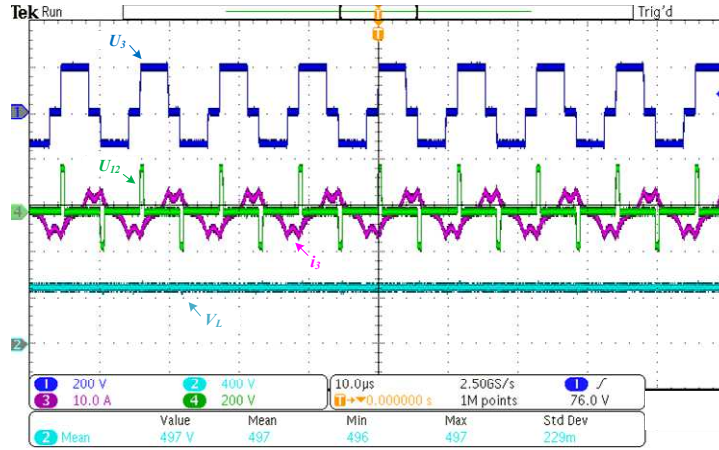
Fig. 5-18. The key waveform after the switching point.

5.3.2 Efficiency and Power Analysis

It is necessary to investigate the performances with different load values for practical use. In this section, the efficiency is the overall dc-dc power transfer efficiency defined as

$$\eta = \frac{P_{out}}{P_{in}} \tag{5.40}$$

where P_{in} is the input power and P_{out} is the output power. Particularly, the input power can be directly gained from the DC power supply EA-PSI 9500-30. The output power can be calculated by

$$P_{out} = \frac{V_L^{\ 2}}{R_L} \tag{5.41}$$

where load R_L is changed from 100 Ω to 200 Ω. The load voltage V_L is kept at 500 V. The 2.5 kW maximum output power happens at the 100 Ω load condition. The output voltage can be directly measured by oscilloscope Tektronix MDO3024. Therefore, the measured values of overall dc-dc efficiency and the output power at different loads are shown in Fig. 5-19.
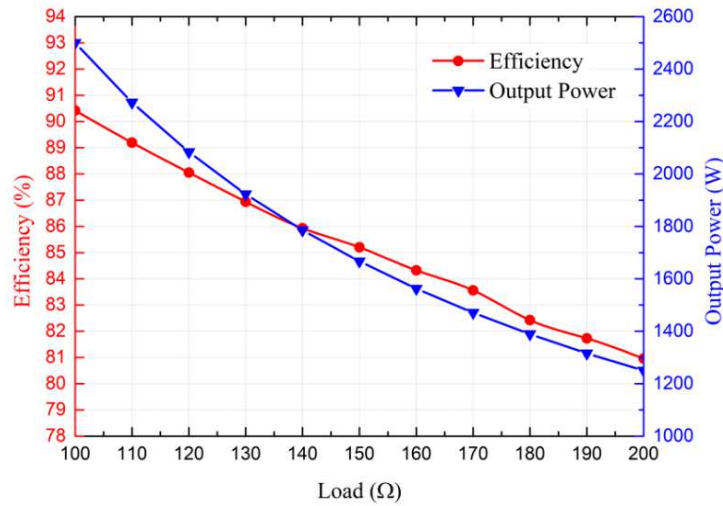
Fig. 5-19. The measured values of overall dc-dc efficiency and the output power at different loads.

5.4 Benchmarking

TABLE 5-4 demonstrates the benchmarking among several segmented DWPT research and this part. Compared with [23], [24], [48], and [93], the proposed DWPT system achieves a high-power level, i.e., 2500 W with refined energized transmitters in each segmented group. The presented system lacks impedance matching and a maximum efficiency tracking system, which may result in a lower frequency compared to other systems. Such a system can be integrated at the receiver side, which is considered the future work to improve the overall efficiency.

TABLE 5-4. THE BENCHMARKING AMONG SEVERAL SEGMENTED DWPT SYSTEMS

Paper	Parameters The mutual inductance between the adjacent TX	Power Level	Number of Energized T_X in each segmented period	Efficiency	Output Voltage Level
This thesis	negligible	2500 W	3	~85%	500 V
[23]	~28 µH	1400 W	---	~89.78%	150 V
[24]	negligible	---	4	~90%	72 V
[48]	~24 µH	120 W	---	~84%	---
[93]	negligible	384 W	Combination between 3 and 4	~90.37%	96 V

--- means not being discussed in the reference

5.5 Summary

Overall, an improved and integrated design of segmented dynamic WPT for ETs is proposed for high power and high voltage applications. The maximum output power and voltage can achieve 2.5 kW and 500 V, respectively. This integrated and improved design offers a stable operation with refined transmitter coils. The well-designed magnetic coupler ensures safe operation for high-power applications. Parallel inverters are adopted to enhance the power level and reduce the voltage or current stress on semiconductor devices. Furthermore, the Q-DD-Q switching sequence is presented. The connection method is clarified for Q-shaped coils and DD coils. Three transmitters Q-DD-Q are energized in each group, which can ensure a stable operation. The proposed switching sequence also makes a balance between the number of energized transmitters and the output voltage variation reduction. A laboratory test using 85 kHz operation frequency is conducted. The output has been tested successfully at a significant power level. The experimental results show that the output voltage of the proposed DWPT is stable and constant while in motion. The dc-dc efficiency can reach approximately 85% from 100 Ω to 200 Ω loads. The future work will focus on resolving current distortion, improving the lateral misalignment tolerance, and achieving zero phase angle for the whole system.

Chapter 6

Conclusions and Future Work

In this thesis, several special magnetic couplers are investigated for different vehicular applications, including a scooter, an automatic guided vehicle, an electric bicycle, and an electric train. Compared to previous magnetic coupler designs in WPT technology, the breakthroughs of this work include: eliminating the magnetic coupling from the source coil to the receiver coil in the three-coil WPT systems (from several μH to null), eliminating the unwanted magnetic couplings among receivers in the dual-receiver WPT systems, increasing the design freedom for engineers, a new resonator design (the influence from the mutual is reduced to null), an improvement of transfer efficiency (from less than ~80% to over ~90%). This section summarizes the major achievements and contributions of this research. Also, promising developments for future vehicular applications are discussed.

6.1 Main contributions of the thesis

One critical issue to resolve must be the unwanted cross-couplings. This thesis utilizes special magnetic couplers to provide simple and effective solutions. Unwanted cross-couplings greatly hinder the development of wireless power transfer systems. Whenever the air gap changes or misalignment occurs, undesirable cross couplings disrupt the system stability. At the same time, wanted magnetic couplings for energy transmission should be maintained or even improved. Therefore, the design of magnetic couplers with compensation networks plays an important role in WPT systems.

To improve the desired magnetic couplings as well as reduce the unwanted magnetic couplings, integrated designs between inductors and capacitors are presented. These couplers aim to enhance the power level, maximize power transferability, improve misalignment tolerance, or minimize the VA rating of the power source.

Also, detailed design procedures are demonstrated, and experimental prototypes

are constructed to verify the proposed ideas. Several special magnetic couplers are investigated for different charging requirements of different automotive vehicles. Presented couplers greatly speed up the design process and eliminate unnecessary cross-couplings, thereby better expressing intrinsic advantages such as load-independent outputs, high robustness, as well as efficiency improvement. Furthermore, the entire system is simple and easy to construct without considering communication and complicated control systems. Overall, the presented couplers are summarized as follows.

In Chapter 2, a special magnetic coupler structure is described. By using three-coil WPT systems for electric scooters and other industrial applications, a universal solution to improving design freedom is offered. This design eliminates the undesired mutual inductance between the source coil and receiver coil, which not only breaks design constraints but also facilitates the expression of intrinsic features. In particular, a load-independent CV output characteristic is analyzed and validated. Efficiency comparisons are made under aligned and misaligned conditions. The experimental validation was carried out using the H-bridge power converter since it is a common type of power electronic circuit used in WPT applications. In summary, the experimental prototype was successfully constructed to test the feasibility of the proposed approach and the experimental results are consistent with the theoretical analysis. With a 14 cm air gap, the presented DC-DC power transfer system can achieve an overall efficiency of 83.3% when supplying 320 W to a 20 W load. The system is suitable for use in electric vehicles, such as scooters. It is impressive that such a design is generalizable to other output voltages or levels of power to fit the different charging requirements of industrial products. Future work will also be focused on the circular DD-shaped coils and the decoupling phenomenon between circular DD-shaped coils and spiral coils.

Chapter 3 demonstrates a special magnetic coupler for automated guided vehicles (AGVs) and other vehicular applications that require dual-load-independent outputs. By using this design, cross couplings, the bottleneck preventing its development, are

drastically reduced. Using the proposed magnetic coupler, measured cross-coupling values are significantly mitigated and are considered to be null. After eliminating cross-couplings between the receivers and the source coil, the outputs of both receivers can be load-independent. After eliminating cross-couplings between two receivers, one cannot influence the other. Furthermore, the proposed structure in this chapter allows engineers to design the magnetic couplers based on specific engineering applications, as different engineering applications may require different coil turns. As the decoupling depends on shapes rather than the delicate design of turns, the proposed decoupling approach is flexible and suitable for industrial applications. Also, the system is simple and compact, as there are no complicated controls or additional reactance. Furthermore, ZPA can be realized, which can reduce the volt-ampere rating and increase the overall efficiency. An experiment with double receivers was conducted in order to verify the characteristics of the proposed system. Moreover, the experimental results are in excellent agreement with the theoretical analysis. Primarily, each receiver will maintain a constant voltage under various load conditions, which results in excellent robustness. At 12 cm air gaps, the prototype is able to deliver 518.4 W with a maximum dc-dc efficiency of 90.16%. The design of this circuit can be generalized to different output voltages and power levels to serve a wide range of charging needs, especially for equipment that requires dual-load-independent power sources operating at a fixed frequency. Overall, the design discussed in this chapter is well suited to industrial use and production.

Chapter 4 mentions an innovative resonator for wireless power transfer systems on Electric Bicycles (EBs) based on the switched S-SP/S compensation scheme and the use of Helmholtz transmitter coils. The newly developed resonators can inherently implement load-independent constant current (CC) and constant voltage (CV) charging for the battery loads. The magnetic resonator mentioned in this chapter ensures a straightforward design for EBs, which eliminates drawbacks caused by conventional methods with variable mutual inductance, communication between the transmitter and receiver, additional user-end converters, complicated control strategies, and bulky LCL

or LCC compensation networks. It is evident that both simulation and experimental results verify the merits of the proposed resonator design. As a result, the maximum efficiency can reach 97.17% in the CC charging mode and 91.17% in the CV charging stage. Moreover, the efficiency can be considered stable when R_z moves from $p=0$ to $p=100$ mm since the variation in efficiency is only 0.66% in CC mode and 0.65% in CV mode.

In Chapter 5, the innovative magnetic coupler design for dynamic wireless power transfer (DWPT) is presented to charge electric trains (ETs). The first one is applicable to segmented DWPT systems with high power and high voltage. Power output and voltage are respectively capable of reaching 2.5 kW and 500 V. With the refined transmitter coils, this integrated and improved design offers a stable and efficient operation for high-power vehicular applications. With the help of the parallel inverter technique, such a design dramatically mitigates the stress of voltage and current on semiconductor devices. Hence, a safe operating environment is realized for high-power vehicular products. Moreover, the Q-DD-Q switching sequence is presented and explained. Q-shaped coils and DD coils are clarified in terms of their connection method. In each group, three Q-DD-Q transmitters are energized, allowing for stable operation. Also, it provides a balance between the reduced output voltage variation and the number of energized transmitters. An experiment using an operating frequency of 85 kHz is conducted in the laboratory. In experimental tests, the output voltage of the proposed DWPT has been demonstrated to remain constant while in motion. Approximately 85% of dc-dc efficiency can be reached from 100 Ω to 200 Ω loads. Further efforts will be made in the future to resolve current distortion, increase the tolerance for lateral misalignment, and achieve zero phase angle for the entire system.

Overall, this thesis provides several magnetic coupler designs for different vehicular applications including scooters, AGVs, EBs, and ETs. Specifically, one important contribution is to eliminate the undesired cross-couplings while maintaining the wanted main couplings. The second contribution is to improve misalignment tolerance. For example, Helmholtz coils enlarge the charging area and improve different

misalignment tolerance for charging EBs. Most importantly, all the research discussed in this thesis utilizes the design of magnetic couplers to realize CC or CV rather than DC-DC converters or high-order compensation topologies. Thus, the presented systems avoid sophisticated control, providing a simple system. Moreover, these systems save components compared to high-order compensation networks, thereby ensuring a light and compact receiver. All the presented designs contribute to the light and compact receiving part installed on the EV. These designs save valuable on-board space and vehicle weight. Hence, all these designs would promote the commercialization of electric vehicles in the coming years.

6.2 Future work

Future work will continue investigating the magnetic coupler designs in WPT systems. Currently, wireless charging tends to act as a backup charger. Two bottlenecks should be taken into consideration in the magnetic coupler designs for further commercialization of wireless chargers in the future; One is cost-effectiveness, and the other is high-power capacity.

LITZ-wire is widely used in wireless power transfer systems for manufacturing couplers and inductors. LITZ-wire is much more expensive than conventional copper wire. Thus, it is essential to save the usage of the LITZ-wire in magnetic couplers. One future research is the bipolar hexagonal magnetic couplers to save the raw material usage, i.e., LITZ-wire, as shown in section 6.2.1.

Next, increasing the power level to hundreds of kilowatts or megawatts is the trend of development to reduce charging times. Due to the increasing power level, the cable weight, and the thermal concerns associated with conductive charging, which requires human labor to plug in, this may demonstrate a violation of human labor regulations. Moreover, adverse weather conditions (heavy snow and rain) can pose a potential danger to conductive charging. Hence, high-power wireless charging is a promising solution. The magnetic coupler designs in high-power WPT systems should be taken into consideration, as discussed in section 6.2.2.

6.2.1 Bipolar Hexagonal Wireless Power Transfer

The shape of the magnetic coupler plays an important role in the design. Interestingly, our nature seems to have a particular thing with a hexagonal shape, such as beehives, snow crystals, marine skeletons, or insect eyes. Drawing experience from nature, the hexagonal coil for wireless charging has been proposed to be a cost-effective solution. However, previous studies tend to focus on the unipolar hexagonal coils [157]. Bipolar hexagonal (BH) coils are rarely discussed. Therefore, one future investigation is the BH coil, and the essential contributions are listed in the following.

1) Cost-Effectiveness: LITZ-wire consisting of multiple strands is widely used to wrap coils in WPT systems [10], which aims to avoid the skin effect and the proximity effect [158]. However, the cost of LITZ-wire tends to be expensive compared to other copper cables. Therefore, it is necessary and practical to design coils cost-effectively. Based on the same mutual inductance, the proposed bipolar hexagonal coil can save LITZ-wire usage compared to traditional DD coils and bipolar circular (BC) coils. As for horizontal misalignment tolerances, these two types are quite similar. That means the proposed structure maintains the horizontal offset tolerance advantages of DD coils.

2) Load-independent constant current (CC) output: CC can be passively achieved on the load part by well-tuned capacitors without any control methods. Only passive components are used, which reduces the complexity dramatically. The 85kHz is selected as the operating frequency as recommended for industrial appliances [101].

3) Load-independent constant voltage (CV) output: In a power electronic system, control methods also play an important role [159], [160]. For example, CV can be actively realized by the active disturbance rejection control (ADRC) [161]. The simulation results show that the voltage can be maintained under a wide range of load conditions. This ensures robustness and reliability while charging industrial applications.

Three types of coils, i.e., the proposed BH coil, conventional DD coil, and bipolar

circular (BC) coils, are introduced for cost-effective comparison, as illustrated in Fig. 6-1.

Especially, the dimension design of these three types is according to practical considerations: the maximum size and the amount of raw material (LITZ-wire) usage. Firstly, the maximum size can be reflected by the maximum length and width of the coil. Hence, the length and width of DD and BC coils are equal to the length and width of BH coils, respectively. Secondly, the LITZ-wire usage can be reflected by the surface area. The mutual inductance between the transmitter (Tx) and the receiver (Rx) is designed as the same for the reasonable comparison. In other words, the surface area of each kind of coil should be different to realize the same mutual inductance. According to [162], the coreless type couplers are usually adopted because the core loss will affect the accuracy. Thus, only coreless type coils are used for comparison in this work.

All coils are wrapped by the 600-strand high-quality LITZ-wire with a 3.5mm wire diameter. The simulation results of the change of mutual inductances with different airgaps are shown in Fig. 6-1 under the 200mm-width condition.
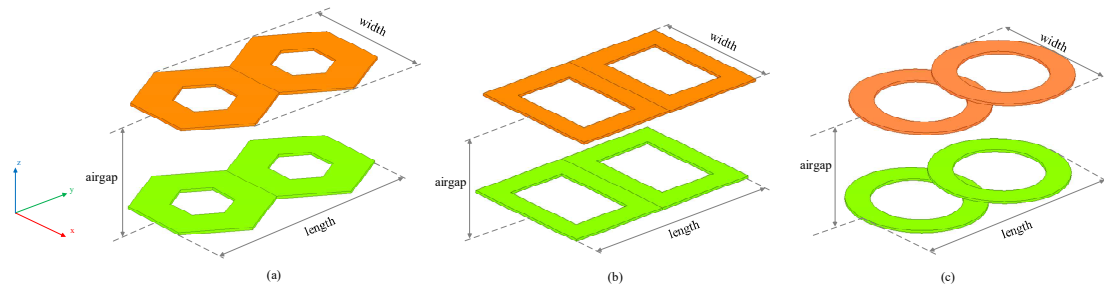
Fig. 6-1. The magnetic couplers (a) the proposed bipolar hexagonal type, (b) the conventional DD type, and (c) the bipolar circular (BC) type.

It can be seen that M is almost the same among these three types under different airgap conditions. The maximum misalignment is 40mm for x-direction (20 percent of the coil width) and 70mm for y-direction. (20 percent of the coil length).

Misalignment tolerance comparisons from different airgaps, x-, y- and diagonal directions are shown in Fig. 6-2 to Fig. 6-5, respectively. It is noted that the total surface area including Tx and Rx from the proposed BH type is 241372 mm^3 while the

corresponding surface from the conventional DD coil is 285542 mm^3, and the BC coil is the 253997 mm^3.

For achieving extremely similar performance, approximately 15.5 or 5 percent of the LITZ-wire usage from the conventional DD type of LITZ-wire or BC coils, respectively, could be saved by the proposed method. Among these three types, BH coils show superiority in mutual inductance while saving raw materials compared to DD coils and BC coils.

The cost-effective BH coil may profoundly impact the industry. Furthermore, with the help of some advanced control methods such as active disturbance rejection control, the value of such a structure can be greatly enlarged for industrial applications.
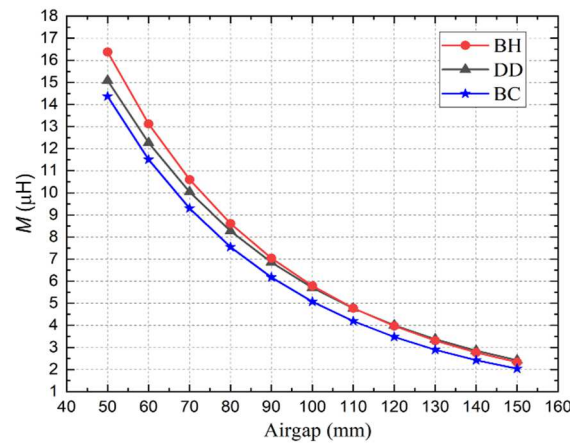
Fig. 6-2. The diagram of the mutual inductance vs. airgap.
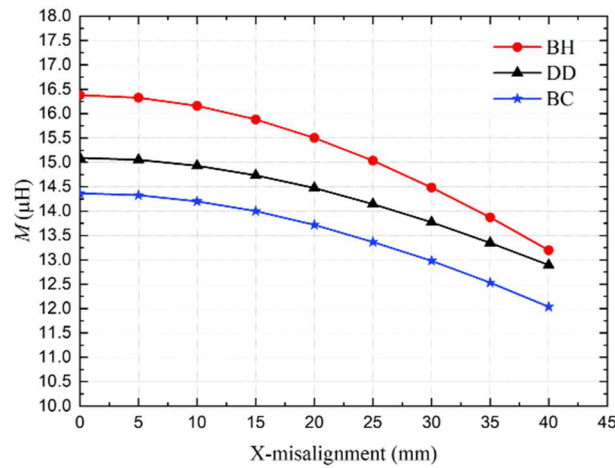
Fig. 6-3. The diagram of the mutual inductance vs. x-misalignment.
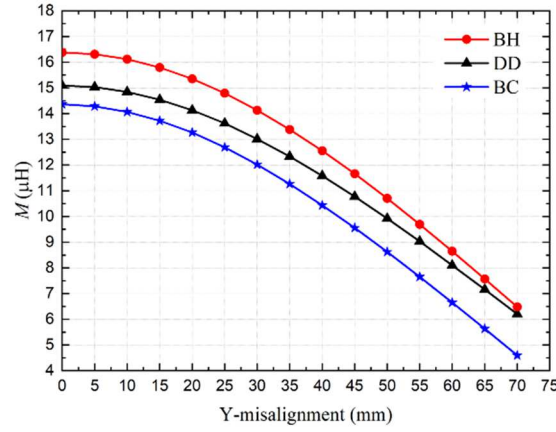
Fig. 6-4. The diagram of the mutual inductance vs. y-misalignment.
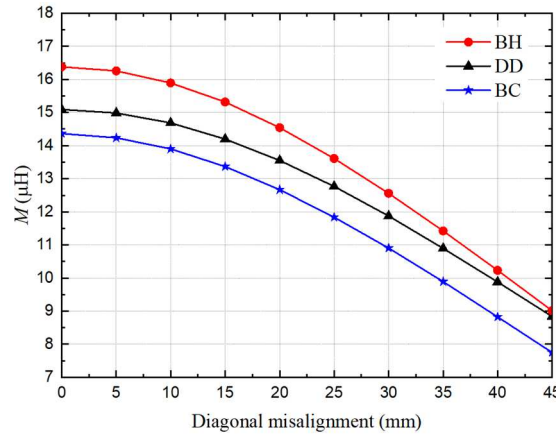
Fig. 6-5. The diagram of the mutual inductance vs. diagonal misalignment.

This work in this section proposes a special magnetic coupler design, namely, a bipolar hexagonal coupler, for saving the LITZ wire usage amount. The FEA simulation results are summarized and show that the BH coil can save raw material usage while maintaining the larger mutual inductance under the same airgap and alignment conditions. Three types of horizontal misalignments are considered in terms of misalignment conditions, including airgap, x, y, and diagonal offsets. As for the future investigation, this work will be focused on the combination of the magnetic structure with ADRC control for different conditions.

6.2.2 Future High-power EV WPT systems

Although wireless power transfer systems for vehicular applications have been investigated for many years, one remaining issue is to improve the power capacity. It

still needs to investigate wireless power transfer for high-power applications such as electric trains or monorails. In this regard, wireless power transfer systems based on multi-level technology appear to be a promising solution. Numerous approaches have been researched recently in order to implement a high-power WPT system [163]. There is a possibility of improving the power capacity of WPT systems by combining multiple transmitters or multiple receivers. As improving the transmission power, the number of transmission paths increases as well.

However, such a system tends to involve more coils or inductors compared to single-path WPT. For example, such a coupler usually contains numerous transmitter coils and receiver coils. Therefore, the unwanted cross-coupling phenomenon must be taken into consideration. For example, Fig. 6-6 shows a typical diagram of a multi-level WPT system, which illustrates that the unwanted cross-couplings, i.e., M_{12}, M_{13}, M_{23}, M_{1b}, M_{1c}, M_{2a}, M_{2c}, M_{3a}, M_{3b}, M_{ab}, M_{bc}, and M_{ac}, need reducing or eliminating in such a system to avoid the side effect from the undesirable cross-couplings (the shift of the maximum efficiency and bifurcation phenomenon). Moreover, TABLE 6-1 clarifies the name of different mutual inductances among different coils. Therefore, such a system brings new challenges to magnetic coupler designs.
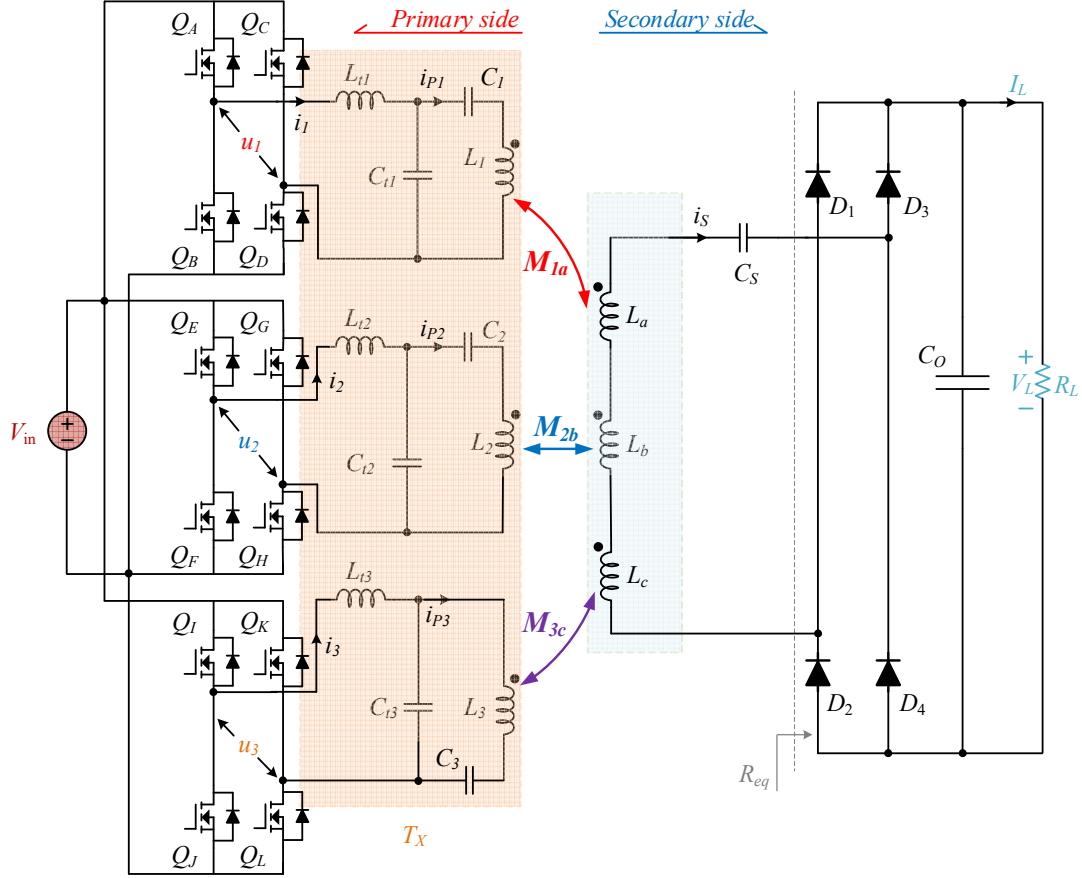
Fig. 6-6. A typical diagram of a multi-level WPT system.

TABLE 6-1. MUTUAL INDUCTANCE CLARIFICATION

	T_X #D1	T_X #D2	T_X #Q	R_X #DA	R_X #DB	R_X #Q
T_X #D1	L_1	M_{12}	M_{13}	M_{1a}	M_{1b}	M_{1c}
T_X #D2	M_{12}	L_2	M_{23}	M_{2a}	M_{2b}	M_{2c}
T_X #Q	M_{13}	M_{23}	L_3	M_{3a}	M_{3b}	M_{3c}
R_X #DA	M_{1a}	M_{2a}	M_{3a}	L_a	M_{ab}	M_{ac}
R_X #DB	M_{1b}	M_{2b}	M_{3b}	M_{ab}	L_b	M_{bc}
R_X #Q	M_{1c}	M_{2c}	M_{3c}	M_{ac}	M_{bc}	L_c

It is simple and necessary to utilize a magnetic coupler design to mitigate or even eliminate these unwanted cross-couplings. Unlike complicated control methods or additional circuits, a well-designed magnetic coupler not only simplifies the system but

also contributes to directly expressing the intrinsic characteristics of the system. For instance, load-independent outputs can be realized when there are no unwanted cross-couplings. Moreover, compensation networks can be designed straightforwardly after removing unwanted cross-couplings.
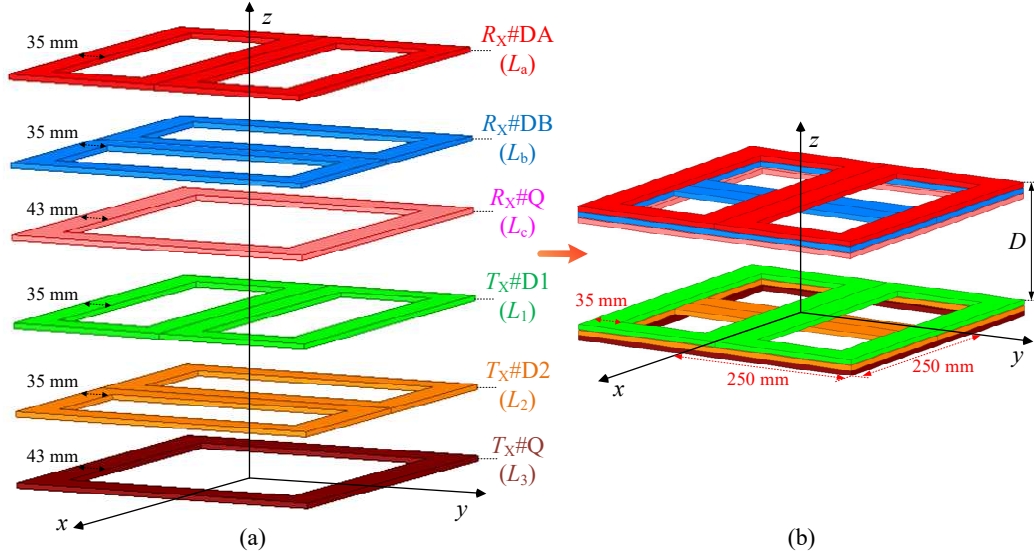
Fig. 6-7. Diagrams of the proposed magnetic coupler with size information and the transmission distance D (a) Exploded view and (b) Whole assembly view.

TABLE 6-2. SIMULATED PARAMETERS

Symbol	Value	Symbol	Value	Symbol	Value
L_1	42.51 µH	L_2	42.14 µH	L_3	39.58 µH
L_a	41.63 µH	L_b	40.91 µH	L_c	38.41 µH
M_{12}	0.203 µH	M_{13}	0.173 µH	M_{23}	0.161 µH
M_{1a}	**9.407** µH	M_{1b}	0.218 nH	M_{1c}	0.045 µH
M_{2a}	0.002 µH	M_{2b}	**9.438** µH	M_{2c}	0.089 µH
M_{3a}	0.040 µH	M_{3b}	0.039 µH	M_{3c}	**12.82** µH
M_{ab}	0.083 µH	M_{bc}	0.165 µH	M_{ac}	0.042 µH
N_{TQ}	7 *turns*	N_{TDD}	6 *turns*	N_{RQ}	7 *turns*
N_{RDD}	6 *turns*	D	80 mm	f	85 kHz

The structure and dimension of the proposed magnetic coupler for high-power applications are illustrated in Fig.6.7. The turns of the DD coil are selected as 6 turns and those of the Q coil are 7 turns. Each side contains three parts: one Q coil, one DD coil, and an orthometric DD coil. All coils have identical sizes and are integrated into the same side to build a compact coupler.

Fig. 6-8 illustrates the simulated result of electromagnetic field distribution by Ansys Maxwell. The coupling coefficient can be used to evaluate the coupling degree between two coils, which can be expressed as

$$k_{ij} = M_{ij} \Big/ \sqrt{L_i L_j} \tag{6.42}$$

where M_{ij} is the mutual inductance between coil #i and #j. L_i and L_j are the self-inductances of coil #i and #j, respectively.

TABLE 6-2 shows that the unwanted cross-mutual inductances, i.e., M_{12}, M_{13}, M_{23}, M_{1b}, M_{1c}, M_{2a}, M_{2c}, M_{3a}, M_{3b}, M_{ab}, M_{bc}, and M_{ac}, are dramatically reduced to a negligible level. Only three major mutual inductances, M_{1a}, M_{2b}, and M_{3c} need considering, which makes the compensation network design straightforward and avoids drawbacks from cross-couplings, e.g., the shift of the maximum efficiency and bifurcation phenomenon.

(a)

(b)
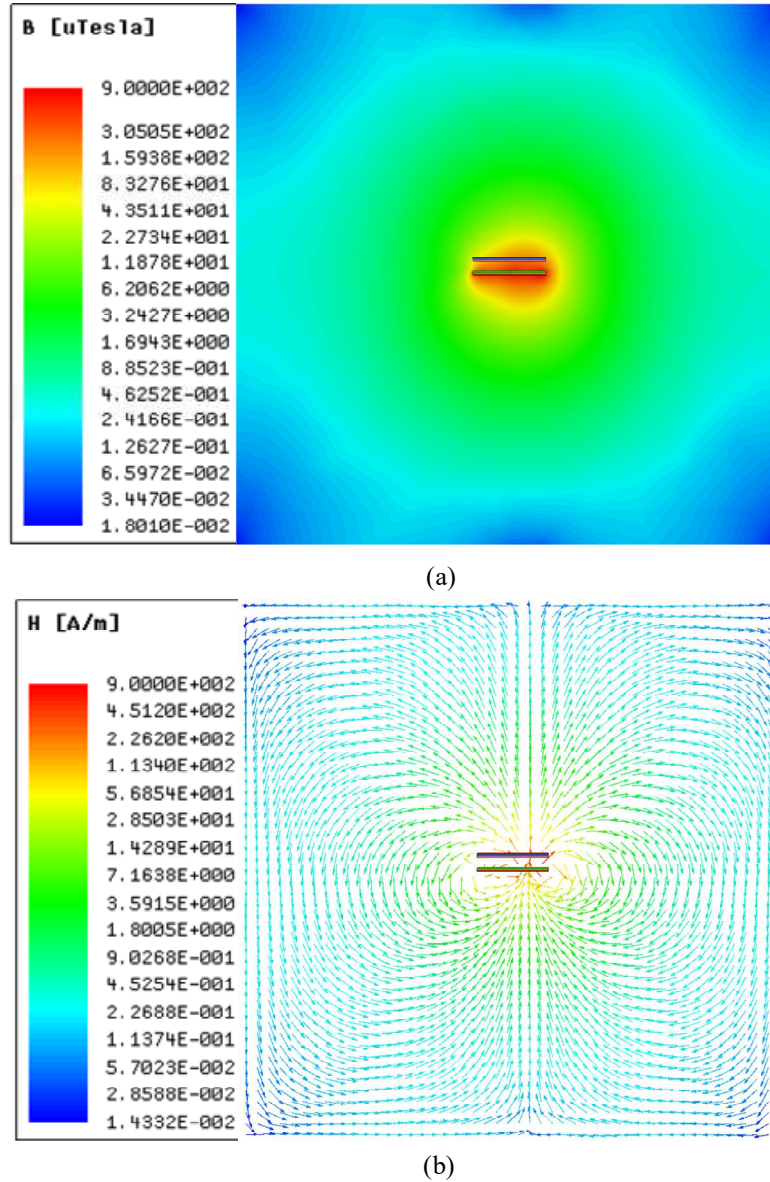
Fig. 6-8. Simulated results by Ansys Maxwell: (a) The distribution of the magnetic flux density and (b) The distribution of the magnetic field intensity.

Overall, this work proposes an input-parallel output-series WPT system with a special magnetic coupler. This magnetic structure eliminates unwanted cross-couplings among coils and provides multiple transmission paths. The compensation network can be designed as simple and straightforward thanks to the presented structure. Finally, this structure is designed to provide high-power wireless power transfer for different vehicular-based applications.

Besides, Future work will not only be focused on the CV output mode but also CC

output mode. CC output can be realized by using additional T-compensation topologies either on the transmitting side or on the receiving side such as LCC or LCL topologies. However, the additional inductors from LCC or LCL topologies will cause cross-couplings. Therefore, future work will also focus on the decoupling between the main magnetic coupling structure (Transmitting and Receiving coils) and additional inductors from LCC or LCL topologies [164].

As for driving high-power ETs, a linear motor is an excellent alternative for a non-adhesion drive system with numerous advantages such as excellent acceleration and deceleration, flexible route planning, quiet and smooth running, and less maintenance cost. Most importantly, a linear motor can contribute to the reduction of the onboard batteries, which saves the weight and cost of the train. The linear motor drive is suitable for electric trains because it can tolerate high installation costs, whereas dynamic wireless power transfer suits other electric vehicles. Future work will be focused on the combination of these two technologies [165].

References

[1]   G. A. Covic and J. T. Boys, "Inductive Power Transfer," *Proceedings of the IEEE,* vol. 101, no. 6, pp. 1276-1289, 2013.

[2]   T. H. Duong, D. W. Berning, A. R. Hefner, and K. M. Smedley, "Long-Term Stability Test System for High-Voltage, High-Frequency SiC Power Devices," in *APEC 07 - Twenty-Second Annual IEEE Applied Power Electronics Conference and Exposition*, 25 Feb.-1 March 2007 2007, pp. 1240-1246,

[3]   S. Y. R. Hui, W. Zhong, and C. K. Lee, "A Critical Review of Recent Progress in Mid-Range Wireless Power Transfer," *IEEE Transactions on Power Electronics,* vol. 29, no. 9, pp. 4500-4511, 2014.

[4]   A. Kurs, A. Karalis, R. Moffatt, J. D. Joannopoulos, P. Fisher, and M. Soljačić, "Wireless Power Transfer via Strongly Coupled Magnetic Resonances," *Science,* vol. 317, no. 5834, pp. 83-86, 2007.

[5]   L. Meng and K. W. E. Cheng, "Wireless power transfer technology for electric iron based on multi-coils induction heating design," *IET Power Electronics,* vol. 12, no. 10, pp. 2566-2577, 2019.

[6]   Y. C. Fong and K. W. E. Cheng, "A switched-capacitor step-up inverter for bidirectional wireless charging applications in electric microcar," in *2017 7th International Conference on Power Electronics Systems and Applications - Smart Mobility, Power Transfer & Security (PESA)*, 12-14 Dec. 2017 2017, pp. 1-6,

[7]   K. W. K. Chen and K. W. E. Cheng, "Review of magnetic resonance technology, recent research trends and issues in EV wireless charging," in *The 11th IET International Conference on Advances in Power System Control, Operation and Management (APSCOM 2018)*, 11-15 Nov. 2018 2018, pp. 1-7,

[8]   C.-K. Lee and W. Zhong, "Wireless power transfer systems for electric vehicles," *Energy systems for electric and hybrid vehicles,* 2016.

[9]   S. Li and C. C. Mi, "Wireless Power Transfer for Electric Vehicle Applications," *IEEE Journal of Emerging and Selected Topics in Power Electronics,* vol. 3, no. 1, pp. 4-17, 2015.

[10]   Z. Zhang, H. Pang, A. Georgiadis, and C. Cecati, "Wireless Power Transfer—An Overview," *IEEE Transactions on Industrial Electronics,* vol. 66, no. 2, pp. 1044-1058, 2019.

[11]   L. Wu, B. Zhang, and J. Zhou, "Efficiency Improvement of the Parity-Time-Symmetric Wireless Power Transfer System for Electric Vehicle Charging," *IEEE Transactions on Power Electronics,* vol. 35, no. 11, pp. 12497-12508, 2020.

[12]   M. A. S. Masoum, P. S. Moses, and K. M. Smedley, "Distribution transformer losses and performance in smart grids with residential Plug-In Electric Vehicles," in *ISGT 2011*, 17-19 Jan. 2011 2011, pp. 1-7,

[13]   P. S. Moses, M. A. S. Masoum, and K. M. Smedley, "Harmonic losses and stresses of nonlinear three-phase distribution transformers serving Plug-In Electric Vehicle charging stations," in *ISGT 2011*, 17-19 Jan. 2011 2011, pp. 1-

6,

[14]   C. K. Lee, W. X. Zhong, and S. Y. R. Hui, "Recent progress in mid-range wireless power transfer," in *2012 IEEE Energy Conversion Congress and Exposition (ECCE)*, 15-20 Sept. 2012 2012, pp. 3819-3824,

[15]   "Vehicular Electric Power Systems: Land, Sea, Air, and Space Vehicles," vol. 28, ed. Portland: Portland: Ringgold, Inc, 2004, p. 167.

[16]   M. Yilmaz and P. T. Krein, "Review of Battery Charger Topologies, Charging Power Levels, and Infrastructure for Plug-In Electric and Hybrid Vehicles," *IEEE Transactions on Power Electronics,* vol. 28, no. 5, pp. 2151-2169, 2013.

[17]   Z. Zhang, H. Pang, C. H. T. Lee, X. Xu, X. Wei, and J. Wang, "Comparative Analysis and Optimization of Dynamic Charging Coils for Roadway-Powered Electric Vehicles," *IEEE Transactions on Magnetics,* vol. 53, no. 11, pp. 1-6, 2017.

[18]   J. Shin *et al.*, "Design and Implementation of Shaped Magnetic-Resonance-Based Wireless Power Transfer System for Roadway-Powered Moving Electric Vehicles," *IEEE Transactions on Industrial Electronics,* vol. 61, no. 3, pp. 1179-1192, 2014.

[19]   S. Bandyopadhyay, P. Venugopal, J. Dong, and P. Bauer, "Comparison of Magnetic Couplers for IPT-Based EV Charging Using Multi-Objective Optimization," *IEEE Transactions on Vehicular Technology,* vol. 68, no. 6, pp. 5416-5429, 2019.

[20]   C. Huang, C. Lin, and Y. Wu, "Simultaneous Wireless Power/Data Transfer for Electric Vehicle Charging," *IEEE Transactions on Industrial Electronics,* vol. 64, no. 1, pp. 682-690, 2017.

[21]   L. Wang, U. K. Madawala, and M. C. Wong, "A Wireless Vehicle-to-Grid-to-Home Power Interface With an Adaptive DC Link," *IEEE Journal of Emerging and Selected Topics in Power Electronics,* vol. 9, no. 2, pp. 2373-2383, 2021.

[22]   F. Shan, J. Luo, W. Wu, F. Dong, and X. Shen, "Throughput Maximization for the Wireless Powered Communication in Green Cities," *IEEE Transactions on Industrial Informatics,* vol. 14, no. 6, pp. 2560-2569, 2018.

[23]   F. Lu, H. Zhang, H. Hofmann, and C. C. Mi, "A Dynamic Charging System With Reduced Output Power Pulsation for Electric Vehicles," *IEEE Transactions on Industrial Electronics,* vol. 63, no. 10, pp. 6580-6590, 2016.

[24]   X. Li, J. Hu, H. Wang, X. Dai, and Y. Sun, "A New Coupling Structure and Position Detection Method for Segmented Control Dynamic Wireless Power Transfer Systems," *IEEE Transactions on Power Electronics,* vol. 35, no. 7, pp. 6741-6745, 2020.

[25]   S. Chopra and P. Bauer, "Driving Range Extension of EV With On-Road Contactless Power Transfer—A Case Study," *IEEE Transactions on Industrial Electronics,* vol. 60, no. 1, pp. 329-338, 2013.

[26]   S. J. Gerssen-Gondelach and A. P. Faaij, "Performance of batteries for electric vehicles on short and longer term," *Journal of power sources,* vol. 212, pp. 111-129, 2012.

[27]   Y. Hori, "Novel EV society based on motor/ capacitor/ wireless — Application

of electric motor, supercapacitors, and wireless power transfer to enhance operation of future vehicles," in *2012 IEEE MTT-S International Microwave Workshop Series on Innovative Wireless Power Transmission: Technologies, Systems, and Applications*, 10-11 May 2012 2012, pp. 3-8,

[28]   C. C. Mi, G. Buja, S. Y. Choi, and C. T. Rim, "Modern Advances in Wireless Power Transfer Systems for Roadway Powered Electric Vehicles," *IEEE Transactions on Industrial Electronics,* vol. 63, no. 10, pp. 6533-6545, 2016.

[29]   W. Wenbin *et al.*, "A Review of High Power Research on Electric Vehicle Wireless Charging," in *2019 14th IEEE Conference on Industrial Electronics and Applications (ICIEA)*, 19-21 June 2019 2019, pp. 2552-2557,

[30]   J. Qu, S. Kiratipongvoot, C. k. Lee, and N. Tang, "An Integrated Printed-Circuit-Board Resonator Design for Inductive Power Transfer System," in *2018 IEEE Energy Conversion Congress and Exposition (ECCE)*, 23-27 Sept. 2018 2018, pp. 2021-2025,

[31]   D. Vincent, P. S. Huynh, N. A. Azeez, L. Patnaik, and S. S. Williamson, "Evolution of Hybrid Inductive and Capacitive AC Links for Wireless EV Charging—A Comparative Overview," *IEEE Transactions on Transportation Electrification,* vol. 5, no. 4, pp. 1060-1077, 2019.

[32]   M. Bertoluzzo, P. D. Barba, M. Forzan, M. E. Mognaschi, and E. Sieni, "Synthesis of the mutual inductor of a Wireless Power Transfer Systems: a field-circuit approach," in *2019 22nd International Conference on the Computation of Electromagnetic Fields (COMPUMAG)*, 15-19 July 2019 2019, pp. 1-4,

[33]   G. A. Rodrigues and L. Lebensztajn, "Study on Transcutaneous Energy Transmission Device Optimal Design," in *2019 22nd International Conference on the Computation of Electromagnetic Fields (COMPUMAG)*, 15-19 July 2019 2019, pp. 1-4,

[34]   I. Fujita, T. Yamanaka, Y. Kaneko, S. Abe, and T. Yasuda, "A 10kW transformer with a novel cooling structure of a contactless power transfer system for electric vehicles," in *2013 IEEE Energy Conversion Congress and Exposition*, 15-19 Sept. 2013 2013, pp. 3643-3650,

[35]   M. Budhia, J. T. Boys, G. A. Covic, and C. Huang, "Development of a Single-Sided Flux Magnetic Coupler for Electric Vehicle IPT Charging Systems," *IEEE Transactions on Industrial Electronics,* vol. 60, no. 1, pp. 318-328, 2013.

[36]   Y. Li, J. Zhao, Q. Yang, L. Liu, J. Ma, and X. Zhang, "A Novel Coil With High Misalignment Tolerance for Wireless Power Transfer," *IEEE Transactions on Magnetics,* vol. 55, no. 6, pp. 1-4, 2019.

[37]   W. X. Zhong, C. K. Lee, and S. Y. Hui, "Wireless power domino-resonator systems with noncoaxial axes and circular structures," *IEEE Transactions on Power Electronics,* vol. 27, no. 11, pp. 4750-4762, 2012.

[38]   J. Qu and C. K. Lee, "Dynamic Modeling for the Wireless Power Transfer System in Domino Structure," *IEEE Transactions on Industrial Electronics,* vol. 69, no. 4, pp. 3556-3565, 2022.

[39]   J. Qu, L. He, N. Tang, and C. K. Lee, "Wireless Power Transfer Using Domino-Resonator for 110-kV Power Grid Online Monitoring Equipment," *IEEE*

Transactions on Power Electronics, vol. 35, no. 11, pp. 11380-11390, 2020.

[40]   J. Qu, S. Kiratipongvoot, C. k. Lee, and N. Tang, "Implementation of Domino Wireless Power Transfer Technology for Power Grid Online Monitoring System," in *2018 IEEE Energy Conversion Congress and Exposition (ECCE)*, 23-27 Sept. 2018 2018, pp. 2016-2020,

[41]   J. Wang *et al.*, "Lateral and Angular Misalignments Analysis of a New PCB Circular Spiral Resonant Wireless Charger," *IEEE Transactions on Magnetics,* vol. 48, no. 11, pp. 4522-4525, 2012.

[42]   H. U. Aydogmus and H. P. Partal, "Modeling and Simulation of Multilayer Rectangular Coils for Wireless Power Transfer Applications," in *2019 International Applied Computational Electromagnetics Society Symposium (ACES)*, 14-19 April 2019 2019, pp. 1-2,

[43]   A. Zaheer, G. A. Covic, and D. Kacprzak, "A Bipolar Pad in a 10-kHz 300-W Distributed IPT System for AGV Applications," *IEEE Transactions on Industrial Electronics,* vol. 61, no. 7, pp. 3288-3301, 2014.

[44]   Q. Deng *et al.*, "Frequency-dependent resistance of litz-wire square solenoid coils and quality factor optimization for wireless power transfer," *IEEE Transactions on Industrial Electronics,* vol. 63, no. 5, pp. 2825-2837, 2016.

[45]   H. Wang, C. Zhang, Y. Yang, H. W. R. Liang, and S. Y. R. Hui, "A Comparative Study on Overall Efficiency of Two-Dimensional Wireless Power Transfer Systems Using Rotational and Directional Methods," *IEEE Transactions on Industrial Electronics,* vol. 69, no. 1, pp. 260-269, 2022.

[46]   S. Kim, G. A. Covic, and J. T. Boys, "Tripolar Pad for Inductive Power Transfer Systems for EV Charging," *IEEE Transactions on Power Electronics,* vol. 32, no. 7, pp. 5045-5057, 2017.

[47]   W. Chwei-Sen, G. A. Covic, and O. H. Stielau, "Investigating an LCL load resonant inverter for inductive power transfer applications," *IEEE Transactions on Power Electronics,* vol. 19, no. 4, pp. 995-1002, 2004.

[48]   S. Zhou and C. C. Mi, "Multi-Paralleled LCC Reactive Power Compensation Networks and Their Tuning Method for Electric Vehicle Dynamic Wireless Charging," *IEEE Transactions on Industrial Electronics,* vol. 63, no. 10, pp. 6546-6556, 2016.

[49]   X. Dai *et al.*, "Improved LCL resonant network for Inductive Power Transfer system," in *2015 IEEE PELS Workshop on Emerging Technologies: Wireless Power (2015 WoW)*, 5-6 June 2015 2015, pp. 1-5,

[50]   W. Zhang and C. C. Mi, "Compensation Topologies of High-Power Wireless Power Transfer Systems," *IEEE Transactions on Vehicular Technology,* vol. 65, no. 6, pp. 4768-4778, 2016.

[51]   H. Hao, G. A. Covic, and J. T. Boys, "An Approximate Dynamic Model of LCL-T-Based Inductive Power Transfer Power Supplies," *IEEE Transactions on Power Electronics,* vol. 29, no. 10, pp. 5554-5567, 2014.

[52]   N. A. Keeling, G. A. Covic, and J. T. Boys, "A Unity-Power-Factor IPT Pickup for High-Power Applications," *IEEE Transactions on Industrial Electronics,* vol. 57, no. 2, pp. 744-751, 2010.

[53]   Z. Pantic, S. Bai, and S. M. Lukic, "ZCS LCC-Compensated Resonant Inverter for Inductive-Power-Transfer Application," *IEEE Transactions on Industrial Electronics,* vol. 58, no. 8, pp. 3500-3510, 2011.

[54]   S. Li, W. Li, J. Deng, T. D. Nguyen, and C. C. Mi, "A Double-Sided LCC Compensation Network and Its Tuning Method for Wireless Power Transfer," *IEEE Transactions on Vehicular Technology,* vol. 64, no. 6, pp. 2261-2273, 2015.

[55]   Y. Zhang, Z. Yan, Z. Liang, S. Li, and C. C. Mi, "A High-Power Wireless Charging System Using LCL-N Topology to Achieve a Compact and Low-Cost Receiver," *IEEE Transactions on Power Electronics,* vol. 35, no. 1, pp. 131-137, 2020.

[56]   F. Pellitteri, N. Campagna, V. Castiglia, A. Damiano, and R. Miceli, "Design, implementation and experimental results of a wireless charger for E-bikes," in *2019 International Conference on Clean Electrical Power (ICCEP)*, 2-4 July 2019 2019, pp. 364-369,

[57]   V. Shevchenko, O. Husev, B. Pakhaliuk, and I. Kondratenko, "Design and Simulation Verification of Low Power Wireless Charging Battery System for Electric Bicycle," in *2018 IEEE 3rd International Conference on Intelligent Energy and Power Systems (IEPS)*, 10-14 Sept. 2018 2018, pp. 22-27,

[58]   M. Bayraktar and E. Yildiriz, "Constant current/voltage charging of a 250w e-bike with wireless power transfer," *El-cezeri,* vol. 7, no. 1, pp. 189-197, 2020.

[59]   Z. Liu, L. Wang, C. Yin, Y. Guo, and C. Tao, "A Research on Constant Voltage Output Characteristics of Wireless Power Transfer System with A DC-DC Converter," in *2019 IEEE 15th Brazilian Power Electronics Conference and 5th IEEE Southern Power Electronics Conference (COBEP/SPEC)*, 1-4 Dec. 2019 2019, pp. 1-4,

[60]   H. L. Li, A. P. Hu, and G. A. Covic, "A power flow control method on primary side for a CPT system," in *The 2010 International Power Electronics Conference - ECCE ASIA -*, 21-24 June 2010 2010, pp. 1050-1055,

[61]   H. H. Wu, A. Gilchrist, K. D. Sealy, and D. Bronson, "A High Efficiency 5 kW Inductive Charger for EVs Using Dual Side Control," *IEEE Transactions on Industrial Informatics,* vol. 8, no. 3, pp. 585-595, 2012.

[62]   C. Xia, W. Wang, G. Chen, X. Wu, S. Zhou, and Y. Sun, "Robust Control for the Relay ICPT System Under External Disturbance and Parametric Uncertainty," *IEEE Transactions on Control Systems Technology,* vol. 25, no. 6, pp. 2168-2175, 2017.

[63]   Y. Li, Y. Sun, and X. Dai, "μ-Synthesis for Frequency Uncertainty of the ICPT System," *IEEE Transactions on Industrial Electronics,* vol. 60, no. 1, pp. 291-300, 2013.

[64]   Y. Li *et al.*, "Reconfigurable Intermediate Resonant Circuit Based WPT System With Load-Independent Constant Output Current and Voltage for Charging Battery," *IEEE Transactions on Power Electronics,* vol. 34, no. 3, pp. 1988-1992, 2019.

[65]   R. Mai, Y. Chen, Y. Zhang, N. Yang, G. Cao, and Z. He, "Optimization of the Passive Components for an S-LCC Topology-Based WPT System for Charging

Massive Electric Bicycles," *IEEE Transactions on Industrial Electronics,* vol. 65, no. 7, pp. 5497-5508, 2018.

[66]   R. Mai, Y. Chen, Y. Li, Y. Zhang, G. Cao, and Z. He, "Inductive Power Transfer for Massive Electric Bicycles Charging Based on Hybrid Topology Switching With a Single Inverter," *IEEE Transactions on Power Electronics,* vol. 32, no. 8, pp. 5897-5906, 2017.

[67]   S. Li, W. Xie, and K. M. Smedley, "A Family of an Automatic Interleaved Dickson Switched-Capacitor Converter and Its ZVS Resonant Configuration," *IEEE Transactions on Industrial Electronics,* vol. 66, no. 1, pp. 255-264, 2019.

[68]   S. Li, Y. Zheng, B. Wu, and K. M. Smedley, "A Family of Resonant Two-Switch Boosting Switched-Capacitor Converter With ZVS Operation and a Wide Line Regulation Range," *IEEE Transactions on Power Electronics,* vol. 33, no. 1, pp. 448-459, 2018.

[69]   S. Li, Y. Zheng, K. M. Smedley, and B. Wu, "A family of resonant two-switch boosting switched-capacitor converter with ZVS operation and a wide voltage-gain range," in *2017 IEEE Applied Power Electronics Conference and Exposition (APEC)*, 26-30 March 2017 2017, pp. 1713-1719,

[70]   C. Wei, Y. Zhao, Y. Zheng, L. Xie, and K. M. Smedley, "Analysis and Design of a Nonisolated High Step-Down Converter With Coupled Inductor and ZVS Operation," *IEEE Transactions on Industrial Electronics,* vol. 69, no. 9, pp. 9007-9018, 2022.

[71]   J. J. Hwang, "Sustainable transport strategy for promoting zero-emission electric scooters in Taiwan," *Renewable & sustainable energy reviews,* vol. 14, no. 5, pp. 1390-1399, 2010.

[72]   I. Pettersson, L. Hagberg, C. Fredriksson, and L. N. Hermansson, "The effect of powered scooters on activity, participation and quality of life in elderly users," *Disability and Rehabilitation: Assistive Technology,* vol. 11, no. 7, pp. 558-563, 2016.

[73]   C. Fredriksson, I. Pettersson, L. Hagberg, and L. Hermansson, "The value of powered mobility scooters from the perspective of elderly spouses of the users - a qualitative study," *Disabil Rehabil Assist Technol,* vol. ahead-of-print, no. ahead-of-print, pp. 1-5.

[74]   M. U. Hashmi and A. Busic, "Limiting Energy Storage Cycles of Operation," in *2018 IEEE Green Technologies Conference (GreenTech)*, 4-6 April 2018 2018, pp. 71-74,

[75]   Y. Sakayanagi, S. Togawa, K. Konagaya, and Y. Kuwahara, "Wireless power transmission for a traveling mobility scooter," in *2016 IEEE Wireless Power Transfer Conference (WPTC)*, 5-6 May 2016 2016, pp. 1-3,

[76]   J. Hu *et al.*, "Hybrid Energy Storage System of an Electric Scooter Based on Wireless Power Transfer," *IEEE Transactions on Industrial Informatics,* vol. 14, no. 9, pp. 4169-4178, 2018.

[77]   Z. Yan *et al.*, "Fault-Tolerant Wireless Power Transfer System With a Dual-Coupled LCC-S Topology," *IEEE Transactions on Vehicular Technology,* vol. 68, no. 12, pp. 11838-11846, 2019.

[78]   J. Zhang, X. Yuan, C. Wang, and Y. He, "Comparative Analysis of Two-Coil and Three-Coil Structures for Wireless Power Transfer," *IEEE Transactions on Power Electronics,* vol. 32, no. 1, pp. 341-352, 2017.

[79]   W. X. Zhong, C. Zhang, X. Liu, and S. Y. R. Hui, "A Methodology for Making a Three-Coil Wireless Power Transfer System More Energy Efficient Than a Two-Coil Counterpart for Extended Transfer Distance," *IEEE Transactions on Power Electronics,* vol. 30, no. 2, pp. 933-942, 2015.

[80]   Q. Wang and Y. Wang, "Power efficiency optimisation of a three-coil wireless power transfer using compensatory reactance," *IET Power Electronics,* vol. 11, no. 13, pp. 2102-2108, 2018.

[81]   Z. Jian, Y. Xinmei, and W. Chuang, "A study of three-coil magnetically coupled resonators for wireless power transfer," in *2015 IEEE International Wireless Symposium (IWS 2015)*, 30 March-1 April 2015 2015, pp. 1-4,

[82]   L. Yang, X. Li, S. Liu, Z. Xu, C. Cai, and P. Guo, "Analysis and Design of Three-Coil Structure WPT System With Constant Output Current and Voltage for Battery Charging Applications," *IEEE Access,* vol. 7, pp. 87334-87344, 2019.

[83]   G. Zhu and D. Gao, "Effects of intermediate coil on power transfer capability and efficiency in three-coil wireless power transfer system," in *2017 IEEE Transportation Electrification Conference and Expo, Asia-Pacific (ITEC Asia-Pacific)*, 7-10 Aug. 2017 2017, pp. 1-6,

[84]   M. Kiani, U. Jow, and M. Ghovanloo, "Design and Optimization of a 3-Coil Inductive Link for Efficient Wireless Power Transmission," *IEEE Transactions on Biomedical Circuits and Systems,* vol. 5, no. 6, pp. 579-591, 2011.

[85]   Y. Ota, T. Takura, F. Sato, and H. Matsuki, "Wireless power transfer by low coupling electromagnetic induction — LC booster," in *2012 IEEE MTT-S International Microwave Workshop Series on Innovative Wireless Power Transmission: Technologies, Systems, and Applications*, 10-11 May 2012 2012, pp. 175-178,

[86]   Q. Vo, Q. Duong, and M. Okada, "Cooperative Transmission in Three-Coil Inductive Power Transfer System with Load-Independent Output Voltages," in *2019 International Workshop on Antenna Technology (iWAT)*, 3-6 March 2019 2019, pp. 225-227,

[87]   K. B. S. Kiran, M. Kumari, R. K. Behera, O. Ojo, and A. Iqbal, "Analysis and experimental verification of three-coil inductive resonant coupled wireless power transfer system," in *2017 National Power Electronics Conference (NPEC)*, 18-20 Dec. 2017 2017, pp. 84-89,

[88]   Y. Li, Q. Xu, T. Lin, J. Hu, Z. He, and R. Mai, "Analysis and Design of Load-Independent Output Current or Output Voltage of a Three-Coil Wireless Power Transfer System," *IEEE Transactions on Transportation Electrification,* vol. 4, no. 2, pp. 364-375, 2018.

[89]   Y. Li, J. Hu, X. Li, H. Wang, and K. W. E. Cheng, "Cost-Effective and Compact Multistring LED Driver Based on a Three-Coil Wireless Power Transfer System," *IEEE Transactions on Power Electronics,* vol. 34, no. 8, pp. 7156-7160, 2019.

[90]   Y. Zhang, T. Lu, and Z. Zhao, "Reducing the impact of source internal resistance by source coil in resonant wireless power transfer," in *2014 IEEE Energy Conversion Congress and Exposition (ECCE)*, 14-18 Sept. 2014 2014, pp. 845-850,

[91]   P. Darvish, S. Mekhilef, and H. A. Illias, "A Novel S-S-LCLCC Compensation for Three-Coil WPT to Improve Misalignment and Energy Efficiency Stiffness of Wireless Charging System," *IEEE Transactions on Power Electronics,* pp. 1-1, 2020.

[92]   V. T. Nguyen, S. H. Kang, J. H. Choi, and C. W. Jung, "Magnetic resonance wireless power transfer using three-coil system with single planar receiver for laptop applications," *IEEE Transactions on Consumer Electronics,* vol. 61, no. 2, pp. 160-166, 2015.

[93]   Y. Li *et al.*, "A New Coil Structure and Its Optimization Design With Constant Output Voltage and Constant Output Current for Electric Vehicle Dynamic Wireless Charging," *IEEE Transactions on Industrial Informatics,* vol. 15, no. 9, pp. 5244-5256, 2019.

[94]   G. Yang *et al.*, "Interoperability Improvement for Rectangular Pad and DD Pad of Wireless Electric Vehicle Charging System Based on Adaptive Position Adjustment," *IEEE Transactions on Industry Applications,* pp. 1-1, 2021.

[95]   S. Ahn *et al.*, "Reduction of electromagnetic field (EMF) of wireless power transfer system using quadruple coil for laptop applications," in *2012 IEEE MTT-S International Microwave Workshop Series on Innovative Wireless Power Transmission: Technologies, Systems, and Applications*, 10-11 May 2012 2012, pp. 65-68,

[96]   Edmunds. "2019 Tesla Model 3 Performance Specs & Features " https://www.edmunds.com/tesla/model-3/2019/st-401784046/features-specs/ (accessed Sept. 2, 2020).

[97]   H. Hao, G. A. Covic, and J. T. Boys, "A Parallel Topology for Inductive Power Transfer Power Supplies," *IEEE Transactions on Power Electronics,* vol. 29, no. 3, pp. 1140-1151, 2014.

[98]   H. Cai, L. Shi, and Y. Li, "Harmonic-Based Phase-Shifted Control of Inductively Coupled Power Transfer," *IEEE Transactions on Power Electronics,* vol. 29, no. 2, pp. 594-602, 2014.

[99]   Y. Li *et al.*, "Analysis, Design, and Experimental Verification of a Mixed High-Order Compensations-Based WPT System with Constant Current Outputs for Driving Multistring LEDs," *IEEE Transactions on Industrial Electronics,* vol. 67, no. 1, pp. 203-213, 2020.

[100] Y. Li, J. Hu, X. Li, and K. E. Cheng, "A Flexible Load-Independent Multi-Output Wireless Power Transfer System Based on Cascaded Double T-Resonant Circuits: Analysis, Design and Experimental Verification," *IEEE Transactions on Circuits and Systems I: Regular Papers,* vol. 66, no. 7, pp. 2803-2812, 2019.

[101] S. International. "Wireless Power Transfer for Light-Duty Plug-in/Electric Vehicles and Alignment Methodology." SAE International. https://saemobilus.sae.org/content/J2954_201904/ (accessed Jun. 1, 2020).

[102] K. Lee and S. H. Chae, "Effect of Quality Factor on Determining the Optimal Position of a Transmitter in Wireless Power Transfer Using a Relay," *IEEE Microwave and Wireless Components Letters,* vol. 27, no. 5, pp. 521-523, 2017.

[103] D. Ahn and S. Hong, "A Study on Magnetic Field Repeater in Wireless Power Transfer," *IEEE Transactions on Industrial Electronics,* vol. 60, no. 1, pp. 360-371, 2013.

[104] J. Lee, K. Lee, and D. Cho, "Stability Improvement of Transmission Efficiency Based on a Relay Resonator in a Wireless Power Transfer System," *IEEE Transactions on Power Electronics,* vol. 32, no. 5, pp. 3297-3300, 2017.

[105] B. Li, X. Zhang, H. Yang, Y. Yao, Y. Wang, and D. Xu, "Design of a Constant-voltage Output Wireless Power Transfer Device," in *2019 IEEE 4th International Future Energy Electronics Conference (IFEEC)*, 25-28 Nov. 2019 2019, pp. 1-5,

[106] X. Liu, W. Han, C. Liu, and P. Pong, "Marker-free coil-misalignment detection approach using TMR sensor array for dynamic wireless charging system of electric vehicles," in *2018 IEEE International Magnetics Conference (INTERMAG)*, 23-27 April 2018 2018, pp. 1-2,

[107] C. Jiang, K. Chau, C. Liu, and W. Han, "Time-division multiplexing wireless power transfer for separately excited DC motor drives," in *2017 IEEE International Magnetics Conference (INTERMAG)*, 24-28 April 2017 2017, pp. 1-2,

[108] W. Liu, K. T. Chau, C. H. T. Lee, C. Jiang, and W. Han, "A Switched-Capacitorless Energy-Encrypted Transmitter for Roadway-Charging Electric Vehicles," *IEEE Transactions on Magnetics,* vol. 54, no. 11, pp. 1-6, 2018.

[109] C. Zhu *et al.*, "Analysis and Design of Cost-Effective WPT Systems With Dual Independently Regulatable Outputs for Automatic Guided Vehicles," *IEEE Transactions on Power Electronics,* vol. 36, no. 6, pp. 6183-6187, 2021.

[110] A. A. S. Mohamed, A. A. Marim, and O. A. Mohammed, "Magnetic Design Considerations of Bidirectional Inductive Wireless Power Transfer System for EV Applications," *IEEE Transactions on Magnetics,* vol. 53, no. 6, pp. 1-5, 2017.

[111] Y. Huang, C. Liu, Y. Zhou, Y. Xiao, and S. Liu, "Power Allocation for Dynamic Dual-Pickup Wireless Charging System of Electric Vehicle," *IEEE Transactions on Magnetics,* vol. 55, no. 7, pp. 1-6, 2019.

[112] B. Che *et al.*, "Omnidirectional wireless power transfer system supporting mobile devices," in *2015 IEEE International Magnetics Conference (INTERMAG)*, 11-15 May 2015 2015, pp. 1-1,

[113] C. Jiang, K. T. Chau, C. Liu, C. H. T. Lee, W. Han, and W. Liu, "Move-and-Charge System for Automatic Guided Vehicles," *IEEE Transactions on Magnetics,* vol. 54, no. 11, pp. 1-5, 2018.

[114] M. Takasaki, Y. Miura, and T. Ise, "Wireless power transfer system for gate power supplies of modular multilevel converters," in *2016 IEEE 8th International Power Electronics and Motion Control Conference (IPEMC-ECCE Asia)*, 22-26 May 2016 2016, pp. 3183-3190,

[115] H. Wang and K. W. E. Cheng, "An Improved and Integrated Design of Segmented Dynamic Wireless Power Transfer for Electric Vehicles," *Energies,* vol. 14, no. 7, p. 1975, 2021.

[116] R. Mai, Y. Luo, B. Yang, Y. Song, S. Liu, and Z. He, "Decoupling Circuit for Automated Guided Vehicles IPT Charging Systems With Dual Receivers," *IEEE Transactions on Power Electronics,* vol. 35, no. 7, pp. 6652-6657, 2020.

[117] W. Han, K. T. Chau, C. Jiang, W. Liu, and W. H. Lam, "Design and Analysis of Wireless Direct-Drive High-Intensity Discharge Lamp," *IEEE Journal of Emerging and Selected Topics in Power Electronics,* vol. 8, no. 4, pp. 3558-3568, 2020.

[118] G. A. Covic and J. T. Boys, "Modern Trends in Inductive Power Transfer for Transportation Applications," *IEEE Journal of Emerging and Selected Topics in Power Electronics,* vol. 1, no. 1, pp. 28-41, 2013.

[119] Y. Yang, S. C. Tan, and S. Y. R. Hui, "Fast Hardware Approach to Determining Mutual Coupling of Series–Series-Compensated Wireless Power Transfer Systems With Active Rectifiers," *IEEE Transactions on Power Electronics,* vol. 35, no. 10, pp. 11026-11038, 2020.

[120] S. Pan, X. Huang, W. Wang, and L. Tan, "Study on transmission characteristics of resonant coupling wireless power transfer system with double receivers," in *2016 Asia-Pacific International Symposium on Electromagnetic Compatibility (APEMC)*, 17-21 May 2016 2016, vol. 01, pp. 1-3,

[121] D. Ahn and S. Hong, "Effect of Coupling Between Multiple Transmitters or Multiple Receivers on Wireless Power Transfer," *IEEE Transactions on Industrial Electronics,* vol. 60, no. 7, pp. 2602-2613, 2013.

[122] S. Moon, B. Kim, S. Cho, C. Ahn, and G. Moon, "Analysis and Design of a Wireless Power Transfer System With an Intermediate Coil for High Efficiency," *IEEE Transactions on Industrial Electronics,* vol. 61, no. 11, pp. 5861-5870, 2014.

[123] C. K. Lee, W. X. Zhong, and S. Y. R. Hui, "Effects of Magnetic Coupling of Nonadjacent Resonators on Wireless Power Domino-Resonator Systems," *IEEE Transactions on Power Electronics,* vol. 27, no. 4, pp. 1905-1916, 2012.

[124] J. J. Casanova, Z. N. Low, and J. Lin, "A Loosely Coupled Planar Wireless Power System for Multiple Receivers," *IEEE Transactions on Industrial Electronics,* vol. 56, no. 8, pp. 3060-3068, 2009.

[125] B. L. Cannon, J. F. Hoburg, D. D. Stancil, and S. C. Goldstein, "Magnetic Resonant Coupling As a Potential Means for Wireless Power Transfer to Multiple Small Receivers," *IEEE Transactions on Power Electronics,* vol. 24, no. 7, pp. 1819-1825, 2009.

[126] W. Chen, H. Li, and W. Lu, "Decoupling design of multi-coil wireless power transfer system with metal insulator," in *2017 IEEE PELS Workshop on Emerging Technologies: Wireless Power Transfer (WoW)*, 20-22 May 2017 2017, pp. 30-33,

[127] C. Cheng *et al.*, "A Multiload Inductive Power Transfer Repeater System With Constant Load Current Characteristics," *IEEE Journal of Emerging and*

Selected Topics in Power Electronics, vol. 8, no. 4, pp. 3533-3541, 2020.

[128]   Y. Zhang, T. Lu, Z. Zhao, K. Chen, F. He, and L. Yuan, "Wireless Power Transfer to Multiple Loads Over Various Distances Using Relay Resonators," *IEEE Microwave and Wireless Components Letters,* vol. 25, no. 5, pp. 337-339, 2015.

[129]   Z. Zhou *et al.*, "A Multi-load Wireless Power Transfer System with Constant Voltage Outputs Using S-LCC Compensation," in *2019 22nd International Conference on Electrical Machines and Systems (ICEMS)*, 11-14 Aug. 2019 2019, pp. 1-6,

[130]   C. Zhong, B. Luo, F. Ning, and W. Liu, "Reactance compensation method to eliminate cross coupling for two-receiver wireless power transfer system," *IEICE Electronics Express,* p. 12.20150016, 2015.

[131]   M. Fu, T. Zhang, X. Zhu, P. C. Luk, and C. Ma, "Compensation of Cross Coupling in Multiple-Receiver Wireless Power Transfer Systems," *IEEE Transactions on Industrial Informatics,* vol. 12, no. 2, pp. 474-482, 2016.

[132]   W. Zhong and S. Y. R. Hui, "Auxiliary Circuits for Power Flow Control in Multifrequency Wireless Power Transfer Systems With Multiple Receivers," *IEEE Transactions on Power Electronics,* vol. 30, no. 10, pp. 5902-5910, 2015.

[133]   Y. Zhang, T. Lu, Z. Zhao, F. He, K. Chen, and L. Yuan, "Selective Wireless Power Transfer to Multiple Loads Using Receivers of Different Resonant Frequencies," *IEEE Transactions on Power Electronics,* vol. 30, no. 11, pp. 6001-6005, 2015.

[134]   M. Ishihara, K. Fujiki, K. Umetani, and E. Hiraki, "Automatic Active Compensation Method of Cross-Coupling in Multiple-receiver Resonant Inductive Coupling Wireless Power Transfer Systems," in *2019 IEEE Energy Conversion Congress and Exposition (ECCE)*, 29 Sept.-3 Oct. 2019 2019, pp. 4584-4591,

[135]   U. Pratik, B. J. Varghese, A. Azad, and Z. Pantic, "Optimum Design of Decoupled Concentric Coils for Operation in Double-Receiver Wireless Power Transfer Systems," *IEEE Journal of Emerging and Selected Topics in Power Electronics,* vol. 7, no. 3, pp. 1982-1998, 2019.

[136]   Y. Wang, Y. Yao, X. Liu, and D. Xu, "S/CLC compensation topology analysis and circular coil design for wireless power transfer," *IEEE Transactions on Transportation Electrification,* vol. 3, no. 2, pp. 496-507, 2017.

[137]   H. Wang, K. W. E. Cheng, X. Li, and J. Hu, "A Special Magnetic Coupler Structure for Three-coil Wireless Power Transfer: Analysis, Design and Experimental Verification," *IEEE Transactions on Magnetics,* pp. 1-1, 2021.

[138]   G. Monti *et al.*, "Wireless power transfer between one transmitter and two receivers: Optimal analytical solution," *Wireless power transfer,* vol. 3, no. 1, pp. 63-73, 2016.

[139]   Z. Dongye *et al.*, "An S-CLC Compensated Load-Independent Inductive Power Relay System With Constant Voltage Outputs," *IEEE Transactions on Power Electronics,* vol. 36, no. 5, pp. 5157-5168, 2021.

[140]   R. Mai, L. Ma, Y. Liu, P. Yue, G. Cao, and Z. He, "A Maximum Efficiency Point Tracking Control Scheme Based on Different Cross Coupling of Dual-Receiver

Inductive Power Transfer System," *Energies (Basel),* vol. 10, no. 2, p. 217, 2017.

[141] H. Z. Z. Beh, G. A. Covic, and J. T. Boys, "Investigation of Magnetic Couplers in Bicycle Kickstands for Wireless Charging of Electric Bicycles," *IEEE Journal of Emerging and Selected Topics in Power Electronics,* vol. 3, no. 1, pp. 87-100, 2015.

[142] H. Z. Z. Beh, G. A. Covic, and J. T. Boys, "Wireless Fleet Charging System for Electric Bicycles," *IEEE Journal of Emerging and Selected Topics in Power Electronics,* vol. 3, no. 1, pp. 75-86, 2015.

[143] Y. Li, J. Hu, F. Chen, S. Liu, Z. Yan, and Z. He, "A New-Variable-Coil-Structure-Based IPT System With Load-Independent Constant Output Current or Voltage for Charging Electric Bicycles," *IEEE Transactions on Power Electronics,* vol. 33, no. 10, pp. 8226-8230, 2018.

[144] Y. Chen, R. Mai, Y. Zhang, Y. Li, and Z. He, "Inductive power transfer for electric bicycles charging based on variable compensation capacitor," in *2017 IEEE Applied Power Electronics Conference and Exposition (APEC)*, 26-30 March 2017 2017, pp. 1389-1393,

[145] Y. Chen, Z. Kou, Y. Zhang, Z. He, R. Mai, and G. Cao, "Hybrid Topology With Configurable Charge Current and Charge Voltage Output-Based WPT Charger for Massive Electric Bicycles," *IEEE Journal of Emerging and Selected Topics in Power Electronics,* vol. 6, no. 3, pp. 1581-1594, 2018.

[146] P. N. Murgatroyd, "The radial field of the Helmholtz pair," *American journal of physics,* vol. 59, no. 10, pp. 949-950, 1991.

[147] R. C. Calhoun, "An elementary derivation of the midplane magnetic field inside a pair of Helmholtz coils," *American journal of physics,* vol. 64, no. 11, pp. 1399-1404, 1996.

[148] C. Hua, C. Bin, Z. Zhihua, and Z. Yanqing, "Characteristics Analyses of Wireless Power Transfer for Ultra-high Speed Maglev Train," in *2021 13th International Symposium on Linear Drives for Industry Applications (LDIA)*, 1-3 July 2021 2021, pp. 1-5,

[149] J. H. Kim *et al.*, "Development of 1-MW Inductive Power Transfer System for a High-Speed Train," *IEEE Transactions on Industrial Electronics,* vol. 62, no. 10, pp. 6242-6250, 2015.

[150] J. Deng, L. Fei, S. Li, T. D. Nguyen, and C. Mi, "Development of a high efficiency primary side controlled 7kW wireless power charger," in *2014 IEEE International Electric Vehicle Conference (IEVC)*, 17-19 Dec. 2014 2014, pp. 1-6,

[151] S. Y. Choi, B. W. Gu, S. Y. Jeong, and C. T. Rim, "Advances in Wireless Power Transfer Systems for Roadway-Powered Electric Vehicles," *IEEE Journal of Emerging and Selected Topics in Power Electronics,* vol. 3, no. 1, pp. 18-36, 2015.

[152] F. Farajizadeh, D. M. Vilathgamuwa, D. Jovanovic, P. Jayathurathnage, G. Ledwich, and U. Madawala, "Expandable N-Legged Converter to Drive Closely Spaced Multitransmitter Wireless Power Transfer Systems for Dynamic Charging," *IEEE Transactions on Power Electronics,* vol. 35, no. 4, pp. 3794-

3806, 2020.

[153] J. M. Miller, P. T. Jones, J. M. Li, and O. C. Onar, "ORNL Experience and Challenges Facing Dynamic Wireless Power Charging of EV's," *IEEE Circuits and Systems Magazine,* vol. 15, no. 2, pp. 40-53, 2015.

[154] F. Zhao, J. Jiang, S. Cui, X. Zhou, C. Zhu, and C. C. Chan, "Research on Bipolar Nonsalient Pole Transmitter for High-Power EV Dynamic Wireless Power Transfer System," *IEEE Transactions on Power Electronics,* vol. 37, no. 2, pp. 2404-2412, 2022.

[155] S. Laporte, G. Coquery, V. Deniau, A. De Bernardinis, and N. Hautière, "Dynamic Wireless Power Transfer Charging Infrastructure for Future EVs: From Experimental Track to Real Circulated Roads Demonstrations," *World electric vehicle journal,* vol. 10, no. 4, p. 84, 2019.

[156] V. Cirimele, F. Freschi, L. Giaccone, L. Pichon, and M. Repetto, "Human Exposure Assessment in Dynamic Inductive Power Transfer for Automotive Applications," *IEEE Transactions on Magnetics,* vol. 53, no. 6, pp. 1-4, 2017.

[157] I. U. Castillo-Zamora, P. S. Huynh, D. Vincent, F. J. Perez-Pinal, M. A. Rodriguez-Licea, and S. S. Williamson, "Hexagonal Geometry Coil for a WPT High-Power Fast Charging Application," *IEEE Transactions on Transportation Electrification,* vol. 5, no. 4, pp. 946-956, 2019.

[158] W. Zhang, J. C. White, A. M. Abraham, and C. C. Mi, "Loosely Coupled Transformer Structure and Interoperability Study for EV Wireless Charging Systems," *IEEE Transactions on Power Electronics,* vol. 30, no. 11, pp. 6356-6367, 2015.

[159] Q. Chongming and K. M. Smedley, "Three-phase unity-power-factor star-connected switch (VIENNA) rectifier with unified constant-frequency integration control," *IEEE Transactions on Power Electronics,* vol. 18, no. 4, pp. 952-957, 2003.

[160] K. M. Smedley and S. Cuk, "Dynamics of one-cycle controlled Cuk converters," *IEEE Transactions on Power Electronics,* vol. 10, no. 6, pp. 634-639, 1995.

[161] S. Zhuo, A. Gaillard, L. Guo, L. Xu, D. Paire, and F. Gao, "Active Disturbance Rejection Voltage Control of a Floating Interleaved DC–DC Boost Converter With Switch Fault Consideration," *IEEE Transactions on Power Electronics,* vol. 34, no. 12, pp. 12396-12406, 2019.

[162] V. X. Thai, S. Y. Choi, B. H. Choi, J. H. Kim, and C. T. Rim, "Coreless power supply rails compatible with both stationary and dynamic charging of electric vehicles," in *2015 IEEE 2nd International Future Energy Electronics Conference (IFEEC)*, 1-4 Nov. 2015 2015, pp. 1-5,

[163] B. Zhang, R. B. Carlson, J. G. Smart, E. J. Dufek, and B. Liaw, "Challenges of future high power wireless power transfer for light-duty electric vehicles---- technology and risk management," *eTransportation,* vol. 2, p. 100012, 2019/11/01/ 2019.

[164] H.-W. Lee, S.-G. Lee, C.-B. Park, J. Lee, and H.-J. Park, "Characteristic analysis of a linear induction motor for a lightweight train according to various secondary schemes," *International Journal of Railway,* vol. 1, no. 1, pp. 6-11,

2008.

[165] Y. D. Chung, C. Y. Lee, D. W. Kim, H. Kang, Y. G. Park, and Y. S. Yoon, "Conceptual Design and Operating Characteristics of Multi-Resonance Antennas in the Wireless Power Charging System for Superconducting MAGLEV Train," *IEEE Transactions on Applied Superconductivity,* vol. 27, no. 4, pp. 1-5, 2017.